Université de Liège
Faculté des Sciences Appliquées

Delayed Detached-Eddy Simulations for Separated Flows

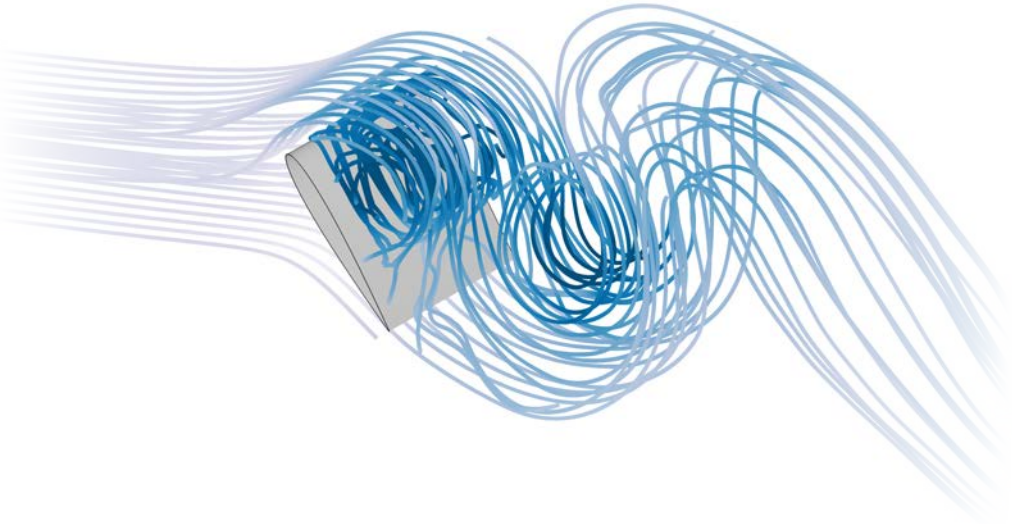

Travail de fin d'études réalisé par

Hüseyin GÜNER

en vue de l'obtention du grade de master Ingénieur Civil en Aérospatiale

Année académique 2014–2015

Promoteur: Pr Vincent TERRAPON

Jury: Pr Grigorios DIMITRIADIS
Pr Tristan GILET
Pr Olivier LÉONARD
Dr Thomas ANDRIANNE

Delayed Detached-Eddy Simulations for Separated Flows

Hüseyin Güner

Master thesis submitted to the Faculty of Applied Sciences of the University of Liège in partial fulfillment for the requirements for the degree of Aerospace Civil Engineer

Academic year 2014–2015

In this thesis, the accuracy of the Delayed Detached-Eddy Simulation (DDES) in predicting massively separated flows is examined. In particular, the flows around an airfoil and a flat plate at high angles of attack are simulated and compared with experimental data.

DDES is a hybrid simulation strategy which combines the Large-Eddy Simulation (LES) and the Reynolds-Averaged Navier-Stokes (RANS) simulation. The RANS mode of the DDES approach operates in boundary layers, where the turbulence model works properly, in order to reduce the computational cost as the use of LES to capture regions of thin boundary layer is expensive. The LES mode operates in regions where the flow is separated to capture large scales which are configuration-dependent and anisotropic.

For both tested configurations, the DDES approach based on the Spalart-Allmaras (S-A) model produces numerical predictions that are in good agreement with the experimental measurements of the aerodynamic force coefficients. By contrast, unsteady RANS simulations using the S-A turbulence model tend to overestimate the dimensionless force coefficients, especially when large regions of massive separation are present in the flow at high angle of attack.

With the DDES approach, the resolution of the grid must be fine enough to capture the details of the physical phenomena present in turbulent flows as smaller eddies are captured by DDES if the mesh is refined.

The DDES results reveal the three-dimensional character of the separated flows around the considered bodies: 3D effects and instabilities appear. The span length of the computational domain is therefore an important factor to predict the aerodynamic forces reliably. In general, the amplitudes of the fluctuations of the aerodynamic force coefficients obtained by DDES are reduced if the span length is longer. The time-averaged lift and drag coefficients are also slightly reduced due to an increase in three-dimensionality.

The generated flow fields are processed using the Dynamic Mode Decomposition (DMD) method in order to extract dynamic information about the considered separated flows. The physics of a complex flow problem experiencing separation is challenging and the dynamic behavior of the flow problem can be described by the most dominant dynamic modes. The dynamic mode decomposition of the flow fields also facilitates the comparisons between the different approaches used to analyze the flows, i.e., CFD results and experimental measurements.

For instance, DMD is able to extract the dominant flow structures from the DDES results to explain the asymmetrical vortex shedding in the case of the flow past a flat plate at an angle of attack of 30° and at a Reynolds number of 2×10^4.

Acknowledgements

First of all, I would like to thank my supervisor, Prof. Vincent Terrapon, for offering me the opportunity to do my thesis in the field of Computational Fluid Dynamics (CFD) to predict turbulent flows. I am very grateful for his assistance, his guidance and his attention to detail. Prof. Vincent Terrapon contributed in an important way to the content of this thesis. I also wish to thank the other members of my jury, Prof. Grigorios Dimitriadis, Prof. Tristan Gilet, Prof. Olivier Léonard, Dr. Thomas Andrianne and Prof. Jean-Philippe Ponthot, for the time they spent to read and evaluate this work.

I wish to express my gratitude to Amandine Guissart, David Thomas and Samir Sid from the MTFC (Multiphysics & Turbulent Flow Computation) research group of the University of Liège, for their help and suggestions. Thanks also to Raphael Egan with whom I have shared the same office during this last semester. He really motivated me to work rigorously.

I would also like to thank all the professors who have taught me. It is not possible to name them all here one by one, but their lectures contributed directly or indirectly to the present work. In particular, I thank Prof. Grigorios Dimitriadis who helped me to process some results.

Thanks to all my friends who made these five academic years more enjoyable. I have received encouragement from many of them.

And last but not least, I would like to thank my family who has always supported me. To my parents, thank you for being there and giving me so much, I love you!

Contents

Abstract i

Acknowledgements ii

Contents iv

Figures vii

1 Introduction 1
- 1.1 Overview of the thesis . . . 3

2 Turbulence modelling and simulations 4
- 2.1 Incompressible Navier-Stokes equations . . . 4
- 2.2 Reynolds-averaged Navier-Stokes simulation . . . 4
  - 2.2.1 Spalart-Allmaras model . . . 5
- 2.3 Large-eddy simulation . . . 7
- 2.4 Detached-eddy simulation . . . 8
- 2.5 Delayed detached-eddy simulation . . . 9

3 RANS simulation of a 2D airfoil 11
- 3.1 Configuration description . . . 11
  - 3.1.1 Assumptions and simplifications . . . 11
  - 3.1.2 Experimental and numerical data . . . 12
- 3.2 Numerical model . . . 13
  - 3.2.1 Boundary conditions . . . 13
  - 3.2.2 Initial conditions . . . 14
  - 3.2.3 Mesh description . . . 14
  - 3.2.4 Solution and algorithm control . . . 17
- 3.3 Results . . . 17
  - 3.3.1 Comparison with the experimental and numerical data . . . 18

4 Delayed detached-eddy simulation of an airfoil at high angle of attack 22
4.1 Configuration description . . . 22
4.1.1 Numerical data . . . 22
4.1.2 Experimental data . . . 23
4.1.3 Assumptions and simplifications . . . 23
4.2 Numerical model . . . 23
4.2.1 Boundary conditions . . . 23
4.2.2 Initial conditions . . . 24
4.2.3 Mesh description . . . 24
4.2.4 Numerical schemes . . . 25
4.2.5 Solution and algorithm control . . . 27
4.3 Results . . . 28
4.3.1 Comparison with the experimental and numerical data . . . 29
4.3.2 Grid refinement study . . . 34
4.3.3 Influence of the spanwise period of the computational domain . . . 37

5 Delayed detached-eddy simulation of a flat plate at high angle of attack 42
5.1 Configuration description . . . 42
5.1.1 Experimental data . . . 42
5.1.2 Configuration used for the numerical simulations . . . 43
5.2 Numerical model . . . 43
5.2.1 Mesh description . . . 44
5.3 Results . . . 44
5.3.1 Comparison with the experimental measurements . . . 47

6 Dynamic mode decomposition of CFD results 58
6.1 Dynamic mode decomposition . . . 58
6.2 Applications . . . 60
6.2.1 DMD of the flow fields obtained by 2D URANS . . . 61
6.2.2 DMD of the flow fields obtained by DDES . . . 66
6.2.3 Reconstruction of the DDES flow fields . . . 72
6.2.4 Modal assurance criterion . . . 75

7 Conclusions 78
7.1 Summary . . . 78
7.2 Future perspectives . . . 80

Appendices 82

Bibliography 89

List of Figures

2.1 Grid densities in a boundary layer: (a) DES grid. (b) Ambiguous grid density. (c) LES grid (the local grid spacing $\Delta \ll \delta$). The dotted line represents the mean velocity. The coordinates are non-dimensionalized by the boundary layer thickness δ, from [23]. 9

3.1 NACA 0012 airfoil. 12
3.2 Domain size for the 2D NACA 0012 airfoil case. 13
3.3 Grid in the *xy*-plane. Close-up views: (a) around the airfoil, (b) near the leading edge and (c) near the sharp trailing edge. 15
3.4 First spacing (wall units) along the upper surface of the airfoil. 16
3.5 Lift coefficient of the NACA 0012 airfoil as a function of the angle of attack ($\mathrm{Re} = 6 \times 10^6$). 19
3.6 Drag coefficient of the NACA 0012 airfoil as a function of the lift coefficient ($\mathrm{Re} = 6 \times 10^6$). 19
3.7 Pressure coefficient distribution along the wall of the NACA 0012 airfoil at different angles of attack. 20
3.8 Streamlines around the NACA 0012 airfoil at $\alpha = 15°$. 21

4.1 Domain size in the *xy*-plane for the NACA 0012 airfoil at high angle of attack case. 24
4.2 Mesh I in the *xy*-plane. Close-up views: (a) around the NACA 0012 airfoil, (b) near the leading edge and (c) near the blunt trailing edge. 26
4.3 Evolution of the aerodynamic force coefficients of the NACA 0012 airfoil at $\alpha = 20°$ obtained by DDES: (a) Lift coefficient as a function of time. (b) Drag coefficient as a function of time. The length of the moving average filter is 100 s. 29
4.4 Lift coefficient of the NACA 0012 airfoil as a function of the angle of attack, adapted from [19]. The black symbols represent the numerical results obtained by the present work. 30

4.5 Drag coefficient of the NACA 0012 airfoil as a function of the angle of attack, adapted from [19]. The black symbols represent the present numerical results. 30
4.6 Evolution of the aerodynamic force coefficients of the NACA 0012 airfoil at $\alpha = 60°$ obtained by URANS. 32
4.7 Power spectral density of $C_L(t)$ at $\alpha = 60°$ obtained by URANS. 33
4.8 Streamlines around the wing at $\alpha = 20°$ obtained by DDES. 33
4.9 Surfaces of $Q = 1$, 5 and 10 colored with the kinematic pressure [m^2/s^2] at $\alpha = 60°$ (2D URANS). 35
4.10 Surface of $Q = 10$ colored with the kinematic pressure [m^2/s^2] at $\alpha = 60°$ (DDES). Four different meshes are used: the number of cells increases from Mesh I to Mesh IV. 36
4.11 Evolution of the aerodynamic force coefficients of the NACA 0012 airfoil at $\alpha = 60°$ for different spanwise periods obtained by DDES: (left) Lift coefficient as a function of time. (right) Drag coefficient as a function of time. 38
4.12 Aerodynamic force coefficients of the NACA 0012 airfoil for different spanwise periods. Comparison with the experimental measurements. . . . 39
4.13 Contours of the z-component of the vorticity ω_z in several slices in the xy-plane at an instant of time (obtained by DDES using the resolution of Mesh I with a span length of $4c$). 40

5.1 Geometry of the flat plate. 43
5.2 Domain size in the xy-plane for the inclined flat plate case. 44
5.3 Grid in the xy-plane. Close-up views: (a) around the flat plate, (b) near the leading edge and (c) near the trailing edge. 45
5.4 Time intervals used to evaluate the temporal average of $C_L(t)$. 46
5.5 Evolution of the aerodynamic force coefficients of the flat plate at $\alpha = 30°$ obtained by 2D URANS: (a) Lift coefficient as a function of time. (b) Drag coefficient as a function of time. 48
5.6 Power spectral density of $C_L(t)$ at $\alpha = 30°$ obtained by 2D URANS. . . . 48
5.7 Streamlines around the flat plate at $\alpha = 30°$ obtained by 2D URANS. . . 50
5.8 Pressure contours at different phases of a cycle obtained by 2D URANS (static flat plate at $\alpha = 30°$). 51
5.9 Instantaneous streaklines of the flow past an inclined flat plate ($\alpha = 18°$ and $\mathrm{Re} = 2 \times 10^4$), from [3]. 51
5.10 Surface of $Q = 0.5$ colored with the kinematic pressure [m^2/s^2] at $\alpha = 30°$ (3D URANS, span = $8c$). 52

5.11 Evolution of the aerodynamic force coefficients of the flat plate at $\alpha = 30°$ obtained by 3D URANS (span = $8c$). 53
5.12 Evolution of the aerodynamic force coefficients of the flat plate at $\alpha = 30°$ obtained by 3D URANS (span = $8c$). The DDES solution is used as an initial condition to start the URANS computation. 53
5.13 Evolution of the aerodynamic force coefficients of the flat plate at $\alpha = 30°$ for different spanwise periods obtained by DDES: (left) Lift coefficient as a function of the non-dimensionalized time. (right) Drag coefficient as a function of the non-dimensionalized time. 55
5.14 Power spectral density of $C_L(t)$ at $\alpha = 30°$ obtained by DDES (span = $8c$). 56
5.15 Surface of $Q = 4$ colored with the kinematic pressure [m^2/s^2] at $\alpha = 30°$ (DDES, span = $8c$). 56

6.1 Grid resolution used for the DMD analysis: $\Delta x/c = 0.03125$ and $\Delta y/c = 0.03125$. The reference frame is also shown. 61
6.2 DMD analysis of the 2D URANS flow fields. 62
6.3 Reconstruction of the aerodynamic force coefficients using the first three dominant dynamic modes. The complex conjugate of each selected dynamic mode is also included in the reconstruction. 65
6.4 Comparison between (a) an instantaneous velocity field obtained by 2D URANS and (b) a velocity field reconstructed using the first three dominant dynamic modes at a given time. 65
6.5 DMD amplitude distribution obtained from the sequence of flow fields given by DDES. 66
6.6 DMD analysis of the spanwise-averaged DDES flow fields. 68
6.7 Representation of the modes extracted from the experimental measurements. 71
6.8 DMD amplitude distribution obtained from the phase and spanwise averaged flow fields given by DDES. 73
6.9 Streamlines around the flat plate at $\alpha = 30°$ obtained by reconstruction of the flow fields using the first three dominant dynamic modes (DDES, phase and spanwise average). 74
6.10 Comparison of the three families of modes extracted from different flow fields: (a) DDES (phase average of the flow fields given in a slice) vs. 2D URANS. (b) DDES (phase and spanwise average) vs. 2D URANS. (c) DDES (phase and spanwise average) vs. DDES (phase average of the flow fields given in a slice). 76
6.11 AutoMAC for the set of modes extracted from the DDES flow fields (phase average of the flow fields given in a slice). 77

Chapter 1

Introduction

The present final year project focuses on massively separated external flows. The description of the physics of these kinds of flow is challenging as turbulent flows, which are random and chaotic, involve a large range of scales, high mixing rates, three-dimensional vorticity and dissipation [4].

The motivation to simulate these phenomena is that flow unsteadiness due to large regions of separated flow can occur in many engineering applications and in practical situations.

Among the applications in aeronautics, an illustration is the massively separated flow behind spoilers which are components placed on an aircraft's wing: their deployment reduces the lift and increases the drag. For instance, such devices are used on some large commercial aircraft for landing or the roll motion.

Another application concerns the delta wings which create conical vortices to generate lift. These vortices break down at high angles of attack.

In general, unsteady flows are prevalent during the takeoff and landing phases of a flight and during maneuvers. In the history of aviation, many fatal aircraft incidents occurred due to loss of control in the stall regime, where a large turbulent wake is generated behind the wing. As an example, 147 aircraft (mostly fighters) were lost due to an aerodynamic stall encountered at high angle of attack in the United States in the 1966–1970 period [13]. Accidents of this kind put emphasis on the need for a better understanding and prediction of separated flows.

Unsteady phenomena also occur in many other situations such as the flows around cars, submarines, bridges and high rise buildings, just to name a few.

RANS turbulence models, even the most complex ones, are not able to predict massively separated flows (e.g., the flow past the landing gear of an aircraft) with engineering accuracy; this is particularly the case when the eddies of the flow are highly geometry-specific [25].

Large-Eddy Simulations (LES) have a higher accuracy compared to the existing RANS simulations. However, LES is computationally expensive for an airplane wing because the boundary layer is thin and it covers a large area near the leading edge. Spalart *et al.* [22] estimate the cost for LES on a typical airplane wing free of separation and with undeployed control surfaces. In this paper's study case, the Reynolds number is set near flight values, the aspect ratio of the wing is equal to 8 and the taper ratio is 0.3. The authors show that the number of grid points has to be at least of the order of 10^{11} and the associated number of time steps is about 5×10^6. The required number of floating-point operations will be unmanageable for several decades. The flow around an airplane wing has a wide range of scales; LES may be more appropriate for simpler configurations with a smaller range of scales (e.g., separated flows at lower Reynolds numbers).

A hybrid simulation strategy called Detached-Eddy Simulation (DES) is formulated in order to address the high computing cost of LES. Also, the Delayed Detached-Eddy Simulation (DDES), which is an improved version of the DES technique, is introduced in order to correct some inaccuracies of the original formulation depending on the grid density (see Chapter 2). DDES operates as a RANS simulation in boundary layers and as LES in regions of separated flow. Eddies inside the boundary layers are modeled whereas the detached eddies, which are in the separation regions, are resolved.

The first objective of the present work is to construct a DDES case in OpenFOAM and then to validate the numerical predictions by comparing with data found in the literature (e.g., experimental measurements or numerical results obtained with a similar or a higher fidelity approach). For this step, the chosen configuration is an airfoil at high angle of attack. The problem is challenging since the flow is massively separated.

DDES is three-dimensional; this characteristic raises the following questions:

- How to choose the resolution of the mesh?
- What is the influence of the span length of the computational domain?

These parameters have to be selected appropriately in order to take account of some flow structures which influence the lift and drag coefficients. One of the objectives of this work is to answer these questions.

Another main goal of this thesis is to better understand the physics of an unsteady separated flow. For this step, the flow over an inclined flat plate is studied. The Dynamic Mode Decomposition (DMD) method based on a sequence of flow fields, which are obtained either numerically or from experimental measurements, is used to obtain information about the coherent structures of a flow problem. This technique is especially useful in combination with the DDES approach, where the predicted flow structures in a turbulent wake are disordered. Moreover, the variations of the aerodynamic force coefficients can be related to the extracted flow structures with the DMD analysis.

OpenFOAM 2.3.0 [6] is the open-source tool for Computational Fluid Dynamics (CFD) used in this thesis. It consists of a package of functions for numerical simulations based on the Finite Volume Method (FVM) [10].

1.1 Overview of the thesis

This report is organized as follows. In Chapter 2, the equations governing the motion of fluids for the flow problems considered in the scope of this work are given with the associated hypotheses. The main characteristics of the RANS simulation based on the Spalart-Allmaras (S-A) model and the LES technique are described. Then, the chapter presents the formulation of the DES and DDES approaches.

In Chapter 3, two-dimensional steady-state RANS simulations of a NACA 0012 airfoil at low angles of attack are performed using the Spalart-Allmaras turbulence model. The main purpose of this preliminary study is to validate the RANS predictions of the attached flows obtained using OpenFOAM. The performance of the S-A model is also assessed by comparing the RANS results with experimental data. Moreover, the chapter presents in detail the CFD methodology used to solve the problem.

In Chapter 4, delayed detached-eddy simulations of an airfoil at high angles of attack are performed. On the one hand, this configuration is used to validate the present numerical model in OpenFOAM. On the other hand, a grid refinement study is carried out and the effect of the span length is analyzed. Throughout this report, a particular effort is made to explain the numerical aspects of the models in detail and to verify the consistency of each numerical solution by comparing with results available from other studies.

In Chapter 5, the DDES technique is used to simulate the flow around a flat plate at high angle of attack. Once again, the simulation results are compared with experimental data (force measurements and PIV).

In Chapter 6, the physics of the flow around the inclined flat plate is studied. The Dynamic Mode Decomposition (DMD) method is used to obtain information about the coherent structures of the considered flow problem.

In Chapter 7, the main conclusions of the thesis are summarized and some ideas for future work are presented.

Chapter 2

Turbulence modelling and simulations

In this chapter, the equations governing the motion of fluids for the flow problems considered in the scope of this work are given with the associated hypotheses.

In this thesis, the DDES technique based on the Spalart-Allmaras model is used. After the description of the main characteristics of the RANS simulation and the LES technique (i.e., the two branches of a hybrid LES–RANS approach), the formulation of the DES and DDES approaches is presented.

2.1 Incompressible Navier-Stokes equations

The flow is considered incompressible (i.e., the density ρ is constant) and the fluid is Newtonian. The incompressible Navier-Stokes (N-S) equations (conservation of mass and conservation of momentum) are the governing equations:

$$\partial_t u_i + u_j \partial_j u_i = -\frac{1}{\rho}\partial_i p + \nu \nabla^2 u_i \tag{2.1}$$

$$\partial_j u_j = 0 \tag{2.2}$$

where $\partial_i \equiv \partial/\partial x_i$, $\mathbf{u}$ is the flow velocity vector, p is the pressure and ν is the kinematic viscosity of the fluid.

2.2 Reynolds-averaged Navier-Stokes simulation

The Reynolds decomposition is

$$u_i = \underbrace{U_i}_{\text{Average}} + \underbrace{u_i'}_{\text{Fluctuation}} \tag{2.3}$$

The convective term of the N-S equations is written in conservative form, then the Reynolds decomposition is introduced into the N-S equations and the equations are averaged to obtain the Reynolds-Averaged Navier-Stokes (RANS) equations:

$$\partial_t U_i + U_j \partial_j U_i = -\frac{1}{\rho}\partial_i P + \nu \nabla^2 U_i - \partial_j \underbrace{\overline{u'_j u'_i}}_{\text{Reynolds stress}} \tag{2.4}$$

$$\partial_j U_j = 0 \tag{2.5}$$

The RANS equations are unclosed; a closure model is required for the Reynolds stress.

2.2.1 Spalart-Allmaras model

The Spalart-Allmaras (S-A) model is a one-equation turbulence model for aerodynamic flows based on a transport equation for an effective eddy viscosity $\tilde{\nu}$, derived from empiricism and dimensional analysis [21]. Transport-equation turbulence models are better than algebraic models for complex flows. The implementation of the S-A model in OpenFOAM is based on [21].

The Boussinesq hypothesis is used:

$$-\overline{u'_i u'_j} + \frac{2}{3}k\delta_{ij} = 2\nu_T S_{ij} \tag{2.6}$$

where k is the turbulent kinetic energy, ν_T is the eddy viscosity and S_{ij} is the rate-of-strain tensor:

$$S_{ij} = \frac{1}{2}\left(\frac{\partial U_i}{\partial x_j} + \frac{\partial U_j}{\partial x_i}\right) \tag{2.7}$$

The term $2/3k\delta_{ij}$ of Equation (2.6) is ignored for the S-A model, so that the Reynolds stress is given by

$$-\overline{u'_i u'_j} = 2\nu_T S_{ij} \tag{2.8}$$

There is a nonlinear relation that transforms the effective eddy viscosity $\tilde{\nu}$ to the eddy viscosity ν_T:

$$\nu_T = \tilde{\nu} f_{v1}, \qquad f_{v1} = \frac{\chi^3}{\chi^3 + c_{v1}^3}, \qquad \chi = \frac{\tilde{\nu}}{\nu} \tag{2.9}$$

where ν is the kinematic viscosity. The transport equation for $\tilde{\nu}$ is formulated as follows:

$$\frac{D\tilde{\nu}}{Dt} = P - D + \frac{1}{\sigma}\left[\nabla\cdot((\nu+\tilde{\nu})\nabla\tilde{\nu}) + c_{b2}(\nabla\tilde{\nu})^2\right] \tag{2.10}$$

with the material derivative of $\tilde{\nu}$: $D\tilde{\nu}/Dt \equiv \partial\tilde{\nu}/\partial t + U_i\partial\tilde{\nu}/\partial x_i$. The production term is given by

$$P = c_{b1}(1-f_{t2})\tilde{S}\tilde{\nu} \tag{2.11}$$

and the destruction term is

$$D = \left(c_{w1}f_w - \frac{c_{b1}}{k^2}f_{t2}\right)\left(\frac{\tilde{\nu}}{d}\right)^2 \tag{2.12}$$

where d is the distance to the closest wall, it influences the behavior of the destruction term. The modified vorticity $\tilde{S}$ is evaluated by

$$\tilde{S} = S + \frac{\tilde{\nu}}{\kappa^2 d^2}f_{v2}, \qquad f_{v2} = 1 - \frac{\chi}{1+\chi f_{v1}} \tag{2.13}$$

S is the magnitude of the vorticity:

$$S = \sqrt{2\Omega_{ij}\Omega_{ij}} \tag{2.14}$$

where Ω_{ij} is the rate-of-rotation tensor:

$$\Omega_{ij} = \frac{1}{2}\left(\frac{\partial U_i}{\partial x_j} - \frac{\partial U_j}{\partial x_i}\right) \tag{2.15}$$

The expression of the function f_w is

$$f_w = g\left(\frac{1+c_{w3}^6}{g^6+c_{w3}^6}\right)^{1/6}, \qquad g = r + c_{w2}(r^6 - r), \qquad r = \min\left(\frac{\tilde{\nu}}{\tilde{S}\kappa^2 d^2}, 10\right) \tag{2.16}$$

The function f_{t2} is given by

$$f_{t2} = c_{t3}\exp(-c_{t4}\chi^2) \tag{2.17}$$

The constants appearing in the turbulence model are calibrated using spreading and velocity profiles of free-shear layers and the skin friction in a flat plate boundary layer. Therefore, the S-A model should perform well in these typical canonical flows which are involved in external flows. The constants are $c_{b1} = 0.1355$, $\sigma = 2/3$, $c_{b2} = 0.622$, $\kappa = 0.41$, $c_{w1} = \frac{c_{b1}}{\kappa^2} + \frac{1+c_{b2}}{\sigma}$, $c_{w2} = 0.3$, $c_{w3} = 2$, $c_{v1} = 7.1$, $c_{t3} = 1.2$ and $c_{t4} = 0.5$.

By construction, the effective eddy viscosity is linear near the wall; this behavior simplifies the resolution.

The boundary condition at walls is

$$\tilde{\nu} = 0 \tag{2.18}$$

As stated in [24], for fully turbulent behavior, the recommended boundary condition at the inflow boundary is

$$\frac{\tilde{\nu}}{\nu} = 3 \text{ to } 5 \tag{2.19}$$

The value $\tilde{\nu}/\nu = 3$ gives $\nu_T/\nu \approx 0.2$.

A RANS simulation is thus a simulation of the statistics of turbulence. Turbulent flows are random but Reynolds-averaged Navier-Stokes simulations of massively separated flows do not predict this property correctly. The turbulence model introduces approximations and errors in CFD simulations.

2.3 Large-eddy simulation

For homogenous filters, the filtered Navier-Stokes equations are given by

$$\partial_k \hat{u}_k = 0 \tag{2.20}$$

$$\partial_t \hat{u}_i + \partial_k \hat{u}_k \hat{u}_i = -\frac{1}{\rho}\partial_i \hat{p} + \nu \nabla^2 \hat{u}_i - \partial_j \underbrace{\tau_{ij}^{\text{SGS}}}_{\text{Subgrid-scale stress}} \tag{2.21}$$

where the hat ($\hat{\cdot}$) means filtering and the subgrid-scale stress, which is an unclosed filtered term, is given by

$$\tau_{ij}^{\text{SGS}} = \widehat{u_i u_j} - \hat{u}_i \hat{u}_j \tag{2.22}$$

LES resolves the eddies of turbulence up to a certain scale which depends on the grid spacing, i.e., LES uses filtering, it cuts off small scales. A subgrid-scale (SGS) closure model is introduced and it represents dissipative effects of the small eddies that are not resolved. The model for subgrid scales in LES is less important than the turbulence model in a RANS simulation for the reason that the unresolved small-scale eddies are less critical than large scales as they are more universal and isotropic [4, 5].

For turbulent flows at Re encountered in transportation, the cost of LES of the whole domain including the turbulent boundary layer is too high for the actual computing power

because in such a situation, the grid spacing for the LES calculation has to scale with a size which needs to be much smaller than the boundary layer thickness δ as depicted in Figure 2.1c.

2.4 Detached-eddy simulation

The Detached-Eddy Simulation (DES) approach is formulated in [22].

The destruction term of the S-A model is proportional to $(\tilde{\nu}/d)^2$ (see Equation (2.12)) and the production term is proportional to $\tilde{S}\tilde{\nu}$ (see Equation (2.11)). When the production term balances the destruction term, one can thus write $\tilde{\nu} \sim \tilde{S}d^2$. This relation is similar to the Smagorinsky subgrid closure model for the LES approach which uses Δ, a length proportional to the grid spacing. Therefore, the S-A model can be used as a subgrid-scale model if the distance to the nearest wall d is replaced by a length proportional to Δ. In the DES approach, a length scale $\tilde{d}$ is introduced:

$$\tilde{d} = \min(d, C_{\mathrm{DES}}\Delta) \tag{2.23}$$

where the empirical constant C_{DES} is of the order of 1 (calibrated to 0.65) and Δ is defined as the largest of the grid spacing in all three directions:

$$\Delta = \max(\Delta x, \Delta y, \Delta z) \tag{2.24}$$

- If $d \ll \Delta$, then $\tilde{d} = d$ and the model acts as a S-A turbulence model (RANS behavior); this situation is encountered in boundary layers where the mesh is non-uniform. For a RANS simulation, the mesh is stretched in the wall normal direction (see Figure 2.1a which illustrates a typical RANS or DES grid in a thin boundary layer): the wall normal grid spacing Δy is smaller than d but the grid spacing parallel to the wall Δx (or Δz) is greater than d, so that Δ is greater than d and the length scale $\tilde{d}$ selects the RANS branch.

- If $\Delta \ll d$, then $\tilde{d} = C_{\mathrm{DES}}\Delta$ and the model acts as a subgrid-scale model (LES behavior). The smallest eddies that are resolved scale with Δ.

Therefore, the design of the grid controls the behavior of the model. If the grid is extremely fine in all directions, DES tends to DNS (Direct Numerical Simulation) which means that the accuracy of the numerical predictions can be improved if the grid is refined.

2.5 Delayed detached-eddy simulation

The Delayed Detached-Eddy Simulation (DDES) approach is formulated in [23].

In the DES technique, the behavior of the model is not clear in the region where $d \sim \Delta$ called "grey area". Moreover, the DES formulation has an incorrect behavior when the grid spacing parallel to the wall $\Delta_{\|}$ is smaller than the thickness of the boundary layer δ as illustrated in Figure 2.1b where $\Delta_{\|} \approx \Delta x \approx \Delta z$.

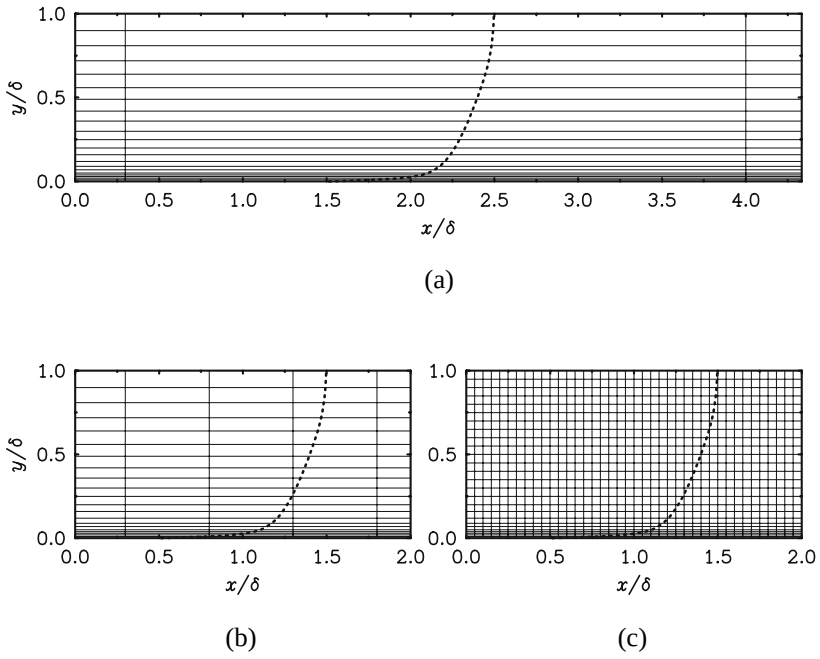

Figure 2.1: Grid densities in a boundary layer: (a) DES grid. (b) Ambiguous grid density. (c) LES grid (the local grid spacing $\Delta \ll \delta$). The dotted line represents the mean velocity. The coordinates are non-dimensionalized by the boundary layer thickness δ, from [23].

Hence, the DES length scale $\tilde{d}$ follows the LES mode in a part of the boundary layer because the grid spacing is fine enough. The eddy viscosity is then reduced and so, the modeled Reynolds stress too. However, the resolution of the grid has not been designed fine enough to support LES content in these regions. This incorrect behavior of the model is known as the Modeled-Stress Depletion (MSD) and a consequence of MSD is that the skin friction is underestimated. This situation can occur after a grid refinement ($\Delta_{\|}$ is low) or when the boundary layers are thick (δ is high) or near separation.

The idea of the delayed detached-eddy simulation approach is to modify the DES limiter in order to maintain the RANS eddy viscosity throughout most of the boundary

layer regardless of the comparison between $\Delta_{\|}$ and δ. The LES function of the method is *delayed* compared to the original formulation, hence the name Delayed DES.

In the DDES formulation, a parameter r_{d} (the subscript d stands for *delayed*) is introduced:

$$r_{\mathrm{d}} = \frac{\nu_T + \nu}{\sqrt{\partial_i u_j \partial_i u_j}\kappa^2 d^2} \tag{2.25}$$

where κ is the Kármán constant. r_d equals 1 in the logarithmic layer and it drops to 0 near the top of the boundary layer. The function f_{d} uses the parameter r_{d}:

$$f_{\mathrm{d}} = 1 - \tanh\left[(8r_{\mathrm{d}})^3\right] \tag{2.26}$$

The constants appearing in the function f_{d} are calibrated by performing tests in a flat plate boundary layer. In LES regions, $r_{\mathrm{d}} \ll 1$, then $f_{\mathrm{d}} \approx 1$ and elsewhere, $f_{\mathrm{d}} \approx 0$. The shape of f_{d} is designed to maintain a RANS solution in boundary layers in the case where Δ is much smaller than δ.

For DDES based on the S-A model, the DES length scale $\tilde{d}$ is modified as follows:

$$\tilde{d} = (1 - f_{\mathrm{d}})d + f_{\mathrm{d}} \min(d, C_{\mathrm{DES}}\Delta) \tag{2.27}$$

If $f_{\mathrm{d}} = 0$, then $\tilde{d} = d$ and the model has a RANS behavior. If $f_{\mathrm{d}} = 1$, then $\tilde{d} = \min(d, C_{\mathrm{DES}}\Delta)$ which corresponds to the original formulation (see Equation (2.23)).

In the original DES formulation, the length scale $\tilde{d}$ is only determined by the grid. In the Delayed DES formulation, the length scale $\tilde{d}$ is also controlled by the eddy viscosity; it is time-dependent, it depends on the solution.

Several test cases simulated using the DDES technique have been studied by Spalart *et al.* (e.g. flat plate boundary layers, a circular cylinder and so on) to validate the behavior of this new formulation [23].

In summary, in the DDES approach, the RANS mode operates in boundary layers where the turbulence model works properly (see Chapter 3) in order to reduce the computational cost (the use of LES to capture regions of thin boundary layer is expensive) and the LES mode operates in regions where the flow is massively separated to capture large scales which are configuration-dependent and anisotropic. LES performs well in free shear flows.

In this thesis, the Spalart-Allmaras model is used as a turbulence model for the RANS mode and as a subgrid-scale model for the LES mode of the DDES approach for smooth transition. All the unsteady RANS simulations presented in this thesis are also performed using the S-A turbulence model.

Chapter 3

RANS simulation of a 2D airfoil

In this chapter, two-dimensional RANS simulations of a NACA 0012 airfoil at low angles of attack are performed using the Spalart-Allmaras turbulence model. The purpose of this preliminary study is to verify that the results given by our RANS simulations performed with OpenFOAM are in agreement with those available in the literature. The validation of the RANS results is necessary since the DDES technique contains a RANS mode.

Moreover, this chapter presents some explications and gives a detailed description about the CFD methodology used to solve the problem. First, the configuration and the assumptions are defined. The experimental and numerical data used for comparison are also given. Then, the numerical aspects of the project are described.

The wall pressure coefficient and the dimensionless force coefficients are analyzed and compared with the experimental data. The flow fields obtained at the maximum angle of attack tested in this chapter are steady-state.

3.1 Configuration description

A 2D NACA 0012 airfoil is considered. Three-dimensional effects are neglected in this chapter (homogeneous in z). The NACA 0012 airfoil given in Figure 3.1 has the following shape parameters: the thickness ratio is 12%, the maximum thickness is located at 30% of the chord from the leading edge and this wing section has no camber. The ordinates of this section type are computed with the formulas defining the 4-digit series of the NACA airfoils.

Moreover, the trailing edge is sharp (i.e., zero-thickness at the trailing edge).

3.1.1 Assumptions and simplifications

The flow is considered incompressible as the Mach number M is $0.15 \lesssim 0.3$ (order of magnitude for the incompressibility condition [2]). Therefore, the density ρ remains con-

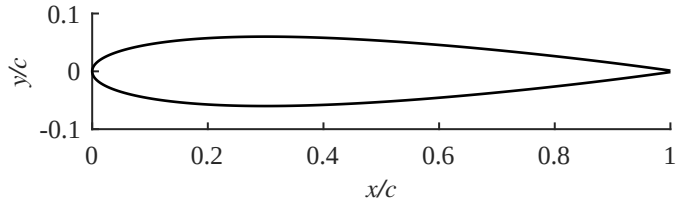

Figure 3.1: NACA 0012 airfoil.

stant and this flow problem is only controlled by the Reynolds number Re, i.e., turbulence does not depend on the fluid, it is a *flow* property. The Reynolds number based on the velocity in the freestream U_∞ and the chord length of the airfoil c is equal to 6×10^6. The freestream velocity can be calculated by

$$\mathrm{Re} = \frac{U_\infty c}{\nu} \quad \Leftrightarrow \quad U_\infty = \frac{\mathrm{Re}\,\nu}{c} \tag{3.1}$$

The flow is isothermal. Tables 3.1 and 3.2 list the parameters of the flow problem.

Property	Symbol	Value
Density	ρ	1.225 kg/m^3
Kinematic viscosity	ν	1.48×10^{-5} m^2/s

Table 3.1: Values of the properties of air at sea level and at 15 °C used in the numerical models.

Quantity	Symbol	Value
Chord length	c	1 m
Reynolds number	Re	6×10^6
Freestream velocity	U_∞	88.8 m/s
Freestream pressure	p_∞	0 Pa

Table 3.2: Data of the problem.

3.1.2 Experimental and numerical data

The present configuration has been simulated using different turbulence models by the NASA Langley Research Center [15]. In this reference, results from several CFD codes (e.g., CFL3D from NASA, GGNS from Boeing and so on) are shown and they all give similar results. In the following, the computed numerical predictions will be compared with those obtained with CFL3D.

Experimental data are also available in the literature for this study case. The force measurements of Ladson [14] and the distribution of the pressure coefficient around the

airfoil measured by Gregory and O'Reilly [8] are used for comparison.

3.2 Numerical model

A case directory is composed of the computational mesh and all configuration files including the boundary and initial conditions, the fluid properties, the turbulence model and its constants, the numerical schemes, the parameters of the solvers, et cetera.

3.2.1 Boundary conditions

The 2D problem is simulated by applying the `empty`[1] boundary type for the front and back faces to not compute in the z-direction.

The boundaries of the computational domain (inlet and outlet) are far from the region of interest in order to minimize their impact on the solution as shown in Figure 3.2.

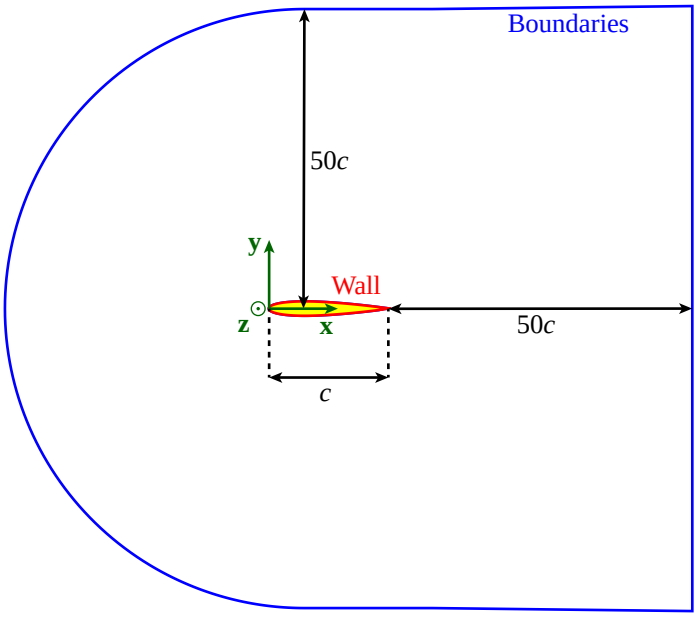

Figure 3.2: Domain size for the 2D NACA 0012 airfoil case.

Table 3.3 indicates the general expressions used to set the boundary conditions in OpenFOAM. This table is also used for the boundary conditions of the cases that will be studied in Chapters 4 and 5.

The inlet corresponds to the portion of the boundary patch where the flux $\rho \mathbf{U}_\infty$ through the boundary patch is negative (into the domain) and the outlet corresponds to the remaining portion where the flux $\rho \mathbf{U}_\infty$ through the boundary patch is positive (out of the domain).

[1] In the text, the `teletypefont family` is used to distinguish the parameters of OpenFOAM.

Quantity	Inlet	Outlet	Wall
p/ρ $[m^2/s^2]$	`zeroGradient`	p_{ref}/ρ	`zeroGradient`
$\mathbf{U}$ $[m/s]$	$(U_\infty \cos(\alpha), U_\infty \sin(\alpha), 0)$	`zeroGradient`	$(0,0,0)$
$\tilde{\nu}$ $[m^2/s]$	3ν (see Section 2.2.1)	`zeroGradient`	0
ν_T $[m^2/s]$	$f(\tilde{\nu})$ (see Equation (2.9))	`zeroGradient`	0

Table 3.3: Boundary conditions in OpenFOAM (Spalart-Allmaras model).

This delimitation therefore depends on the angle of attack α, which is measured in the reference frame given in Figure 3.2, and the normal to the far field boundary patch.

The `zeroGradient` boundary type specifies that the gradient of the quantity is zero in the direction perpendicular to the boundary (Neumann boundary condition). The `fixedValue` boundary type imposes a constant value at the boundary (Dirichlet boundary condition).

The impermeability condition and the no-slip one (viscous fluid flow) are applied at the wall of the solid body.

In OpenFOAM, the kinematic pressure is used by default, i.e., the pressure p is divided by the constant density ρ: p/ρ $[m^2/s^2]$. The flow being incompressible, the absolute value of the pressure is not relevant: only the relative pressure matters and the reference pressure p_{ref} is set to zero.

3.2.2 Initial conditions

The pressure field is zero initially in the whole flow domain. The freestream velocity is used to set a uniform initial velocity field. The inflow boundary condition values are used to set the initial condition of all other quantities.

3.2.3 Mesh description

The quality of the mesh is critical for result accuracy. A structured grid is chosen since it is more efficient than an unstructured one for this study case (see Figure 3.3). Hexahedral cells are used because they are more accurate and with less memory requirements than tetrahedral ones [10]. Discontinuities in mesh cell size are avoided: the cell size varies in a continuous way. Distortions in the mesh are reduced.

Even if the problem is in two dimensions, OpenFOAM requires a 3D mesh; that's why the 2D mesh in the *xy*-plane is extruded in the spanwise direction in order to have at least one volume cell in each direction. All the meshes used in this project are created with the open source software Gmsh [7].

The cells are clustered where the flow varies strongly as can be seen in Figure 3.3. The grid spacing in the irrotational regions, where turbulence is not produced, is much larger than near the wall and wake regions to reduce the computational cost.

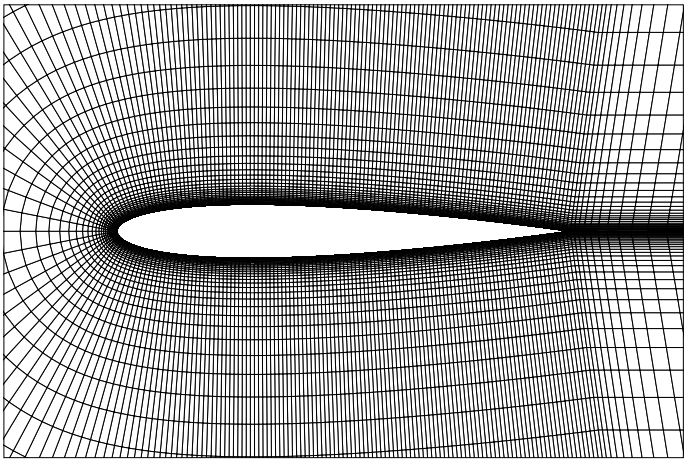

(a)

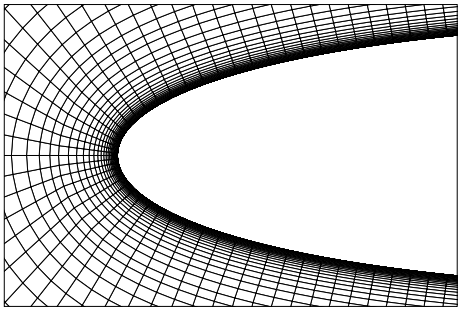

(b)

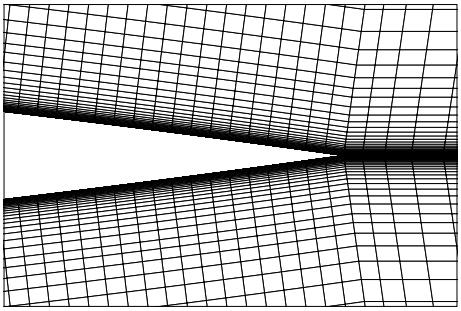

(c)

Figure 3.3: Grid in the *xy*-plane. Close-up views: (a) around the airfoil, (b) near the leading edge and (c) near the sharp trailing edge.

A C-type grid is appropriate for attached flows over an airfoil with a sharp trailing edge. However, there are unnecessary grid points in the zone downstream of the trailing edge with a structured C-type grid (see Figure 3.3c), but this does not increase the computational cost significantly in the case of a 2D steady-state RANS simulation.

The cells are orthogonal to the wall. The first grid points away from the wall are set such that

$$y^+ = \frac{y u_*}{\nu} \lesssim 1, \qquad u_* = \sqrt{\frac{\tau_w}{\rho}}, \qquad \tau_w = \mu \left.\frac{\partial u}{\partial y}\right|_{y=0} \tag{3.2}$$

where y is the distance normal to the surface, μ is the dynamic viscosity, τ_w is the wall shear stress and u_* is the friction velocity. This criterion is required in order to capture the turbulent boundary layer correctly. Therefore, the boundary layer is resolved without using a wall function with the S-A turbulence model. In the present configuration, the first grid point is at $y/c = 1.6 \times 10^{-6}$ and the criterion is verified a posteriori (see Figure 3.4). A grid stretching is applied in the normal direction, the stretching ratio is 1.2.

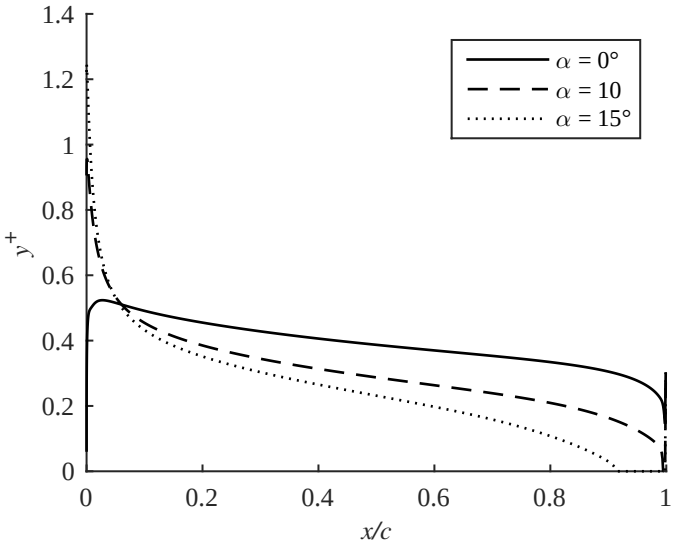

Figure 3.4: First spacing (wall units) along the upper surface of the airfoil.

Table 3.4 gives the number of cells contained in the tested mesh.

	Number of points: around the airfoil	in the normal direction	in the spanwise direction	Number of hexahedra
Mesh	256	88	2	29058

Table 3.4: Characteristics of the grid used for the 2D airfoil case.

3.2.4 Solution and algorithm control

The flow is statistically steady (no time derivative). The Semi Implicit Methods Pressure Linked Equations (SIMPLE) algorithm designed for steady-state problems is used. The steady-state solver for incompressible turbulent flows of OpenFOAM is called `simpleFoam`.

The steady-state solver `simpleFoam` is based on an iterative method; a convergence criterion can be set: if the residuals of all quantities are below a certain tolerance, the computation is stopped.

For statistically-stationary problems, the computation is made more stable by using under-relaxation. The under-relaxation factor is set to 0.3 for the pressure and to 0.7 for other quantities. An under-relaxation factor of 1 corresponds to no under-relaxation (i.e., the change of a variable is not limited between two consecutive iterations).

3.3 Results

For a two-dimensional body, the lift coefficient c_l is defined as follows:

$$c_l = \frac{L'}{\frac{1}{2}\rho_\infty U_\infty^2 c} \tag{3.3}$$

where ρ_∞ is the freestream density and L' is the lift per unit span. The drag coefficient c_d is given by

$$c_d = \frac{D'}{\frac{1}{2}\rho_\infty U_\infty^2 c} \tag{3.4}$$

where D' is the drag per unit span. The pressure coefficient C_p is

$$C_p = \frac{p - p_\infty}{\frac{1}{2}\rho_\infty U_\infty^2} \tag{3.5}$$

where p_∞ is the freestream pressure.

Table 3.5 shows the predicted aerodynamic force coefficients for three angles of attack: $\alpha = 0°$, $10°$ and $15°$.

Model	α	c_l	c_d
RANS S-A	$0°$	≈ 0	8.1920×10^{-3}
	$10°$	1.0778	1.2436×10^{-2}
	$15°$	1.5210	2.1581×10^{-2}

Table 3.5: Results for the NACA 0012 airfoil at angles of attack below the stall angle.

3.3.1 Comparison with the experimental and numerical data

The present numerical results obtained by steady-state RANS simulations using the Spalart-Allmaras turbulence model can be validated by looking at the comparisons with the numerical data (see Figures 3.5, 3.6 and 3.7). Moreover, for the case of a NACA 0012 airfoil at angles of attack below the critical angle of attack leading to a stall, the numerical predictions obtained by steady-state RANS are consistent with the experimental measurements. Therefore, the numerical model (i.e., the size of the computational domain, the mesh, the turbulence model, the boundary conditions, the initial conditions and so on) seems to be appropriate for this study case.

By contrast, in Chapter 4, it will be shown that RANS simulations, even the unsteady computations, do not predict the aerodynamic force coefficients accurately in the case of an airfoil at high angles of attack (above the stall angle).

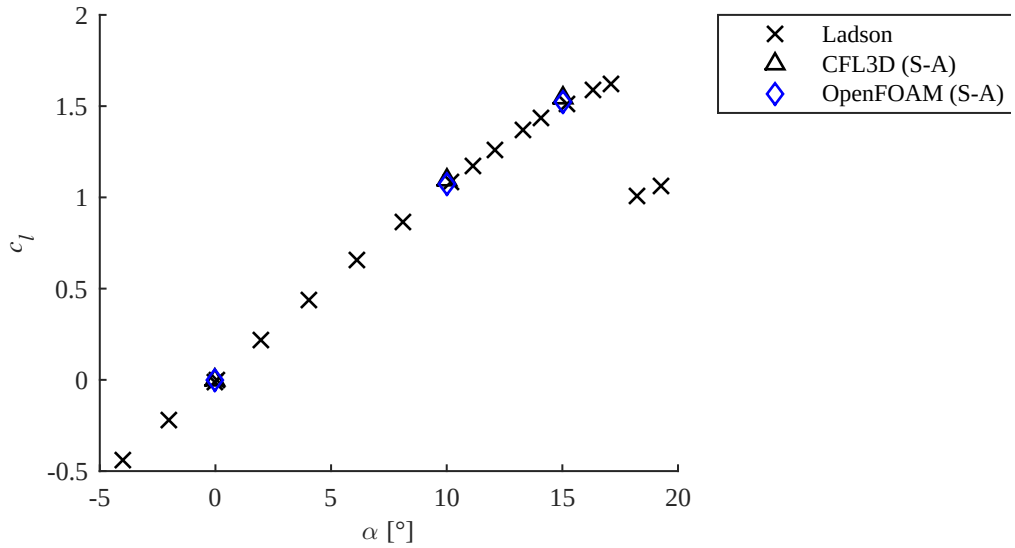

Figure 3.5: Lift coefficient of the NACA 0012 airfoil as a function of the angle of attack ($\mathrm{Re} = 6 \times 10^6$).

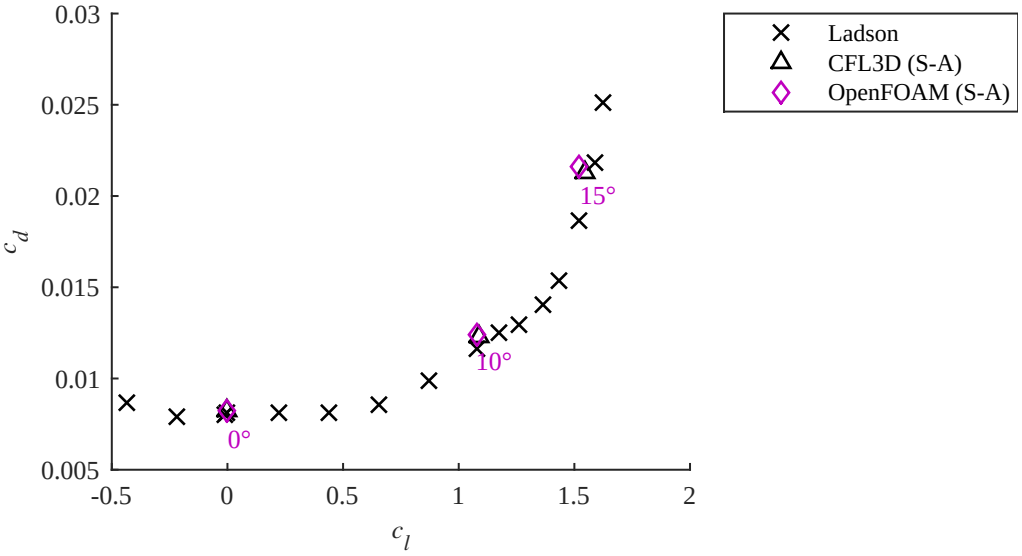

Figure 3.6: Drag coefficient of the NACA 0012 airfoil as a function of the lift coefficient ($\mathrm{Re} = 6 \times 10^6$).

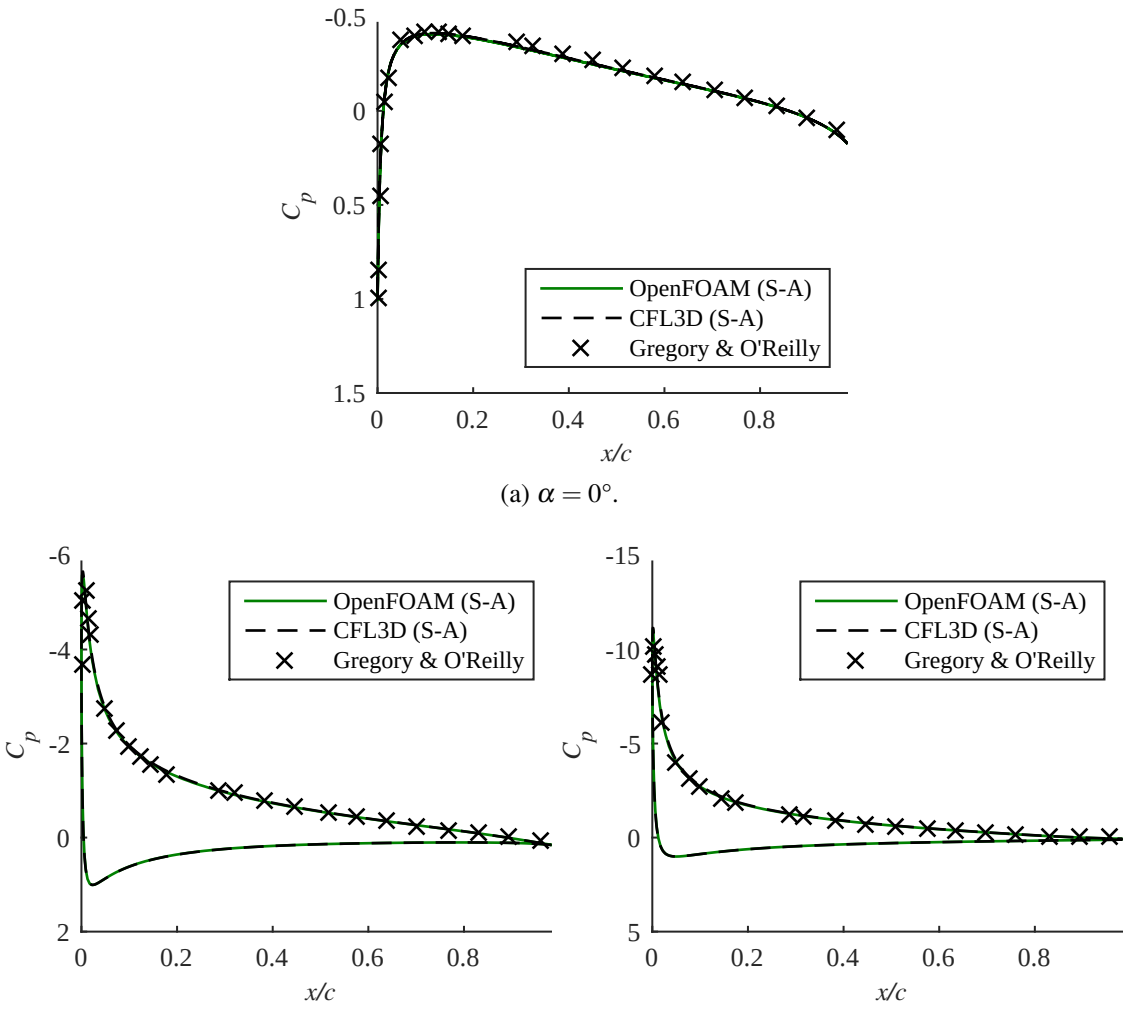

(a) $\alpha = 0°$.

(b) $\alpha = 10°$.

(c) $\alpha = 15°$.

Figure 3.7: Pressure coefficient distribution along the wall of the NACA 0012 airfoil at different angles of attack.

From the graph in Figure 3.5, it can be seen that the section lift coefficient c_l is zero when the angle of attack α is null because the airfoil is symmetrical. The lift is positive (upward) if α is positive. The lift coefficient curve varies almost linearly in the 0° to 12° range and it reaches a maximum for a value of α slightly higher than 15°. The lift decreases after the maximum value.

For $\alpha = 0°$, the stagnation point ($C_p = 1$) is located at the leading edge as the section is symmetrical (see Figure 3.7). For $\alpha = 10°$ and 15°, the stagnation point is located on the lower surface near the leading edge. The pressure on the upper surface increases after the minimum pressure point ($\frac{dp}{ds} > 0$: adverse pressure gradient). The slope of the pressure distribution curve on the upper surface after the suction peak is steeper for $\alpha =$ 15° indicating that the adverse pressure gradient on the upper surface increases as the angle of attack increases.

At low angles of attack, the flow remains attached over a large part of the surface; the separation point is located in the vicinity of the trailing edge. As the angle of attack increases, the separation point moves slightly forward. Regions of massive separation are not observed at $\alpha = 15°$ as can be inferred from the streamlines given in Figure 3.8.

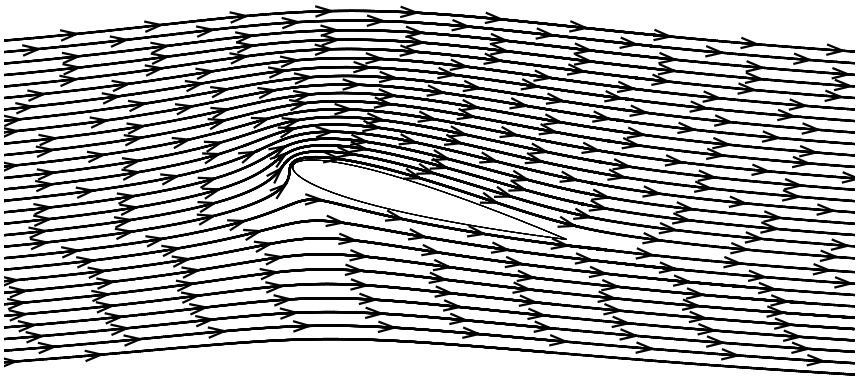

Figure 3.8: Streamlines around the NACA 0012 airfoil at $\alpha = 15°$.

Chapter 4

Delayed detached-eddy simulation of an airfoil at high angle of attack

In this chapter, delayed detached-eddy simulations of an airfoil at high angles of attack are performed. Practical applications of this situation can be found in helicopter blades or in marine propellers in reversed operation, for example [11].

This configuration has already been simulated with the DES approach by Spalart *et al.* [19] and their results are chosen for comparison. This configuration is used to validate the present numerical model in OpenFOAM (i.e., the boundary conditions, the size of the computational domain, the mesh, the numerical schemes, etc.) which is described completely in Section 4.2.

The space discretization introduces numerical errors. A grid refinement study is undertaken in order to have an idea of the evolution of the discretization errors when the mesh is finer. Furthermore, the effect of the span length on the aerodynamic force coefficients is analyzed.

4.1 Configuration description

This section describes the geometry and the related experimental and numerical data that have been chosen. It also explains all assumptions and simplifications that have been made.

4.1.1 Numerical data

The geometry and the conditions of the configuration are based on a paper of Spalart *et al.*, the authors of the DES method [19]. In the paper, the authors use the DES approach but the simulated cases are free of grid problems encountered with this approach (see Section 2.5) as stated in [23]. Also, no grid refinement analysis is presented in the paper.

A NACA 0012 airfoil with a blunt trailing edge is considered as can be seen from Figure 4.2c. The shape of this airfoil is obtained using the original equation for a symmetrical 4-digit NACA airfoil.

The Reynolds number Re based on the chord length of the airfoil is equal to 10^5. Actually, after stall, the dependence of the flow on Re is small in the considered regime [19]. The fluid properties are the same than in Chapter 3 (see Table 3.1). The data of the problem used for the simulations are summarized in Table 4.1.

Quantity	Symbol	Value
Chord length	c	1 m
Reynolds number	Re	10^5
Freestream velocity	U_∞	1.48 m/s
Freestream pressure	p_∞	0 Pa

Table 4.1: Data of the problem.

4.1.2 Experimental data

Experimental force measurements of the same configuration available in [11] are used to confirm the numerical predictions. In the wind-tunnel experiments, the wing, which has the same airfoil (NACA 0012) along the span, is placed between the tunnel walls in order to obtain the aerodynamic characteristics of the airfoil (e.g., the section drag). Indeed, this setup suppresses the wing-tip drag and the induced drag encountered in a rectangular wing model.

4.1.3 Assumptions and simplifications

The flow is not statistically stationary at angles of attack beyond the stall angle (i.e., the angle of attack which gives the maximum lift coefficient). Therefore, unsteady simulations are necessary. Otherwise, the same hypotheses than those presented in Section 3.1.1 are also valid in this chapter.

4.2 Numerical model

This section details the numerical aspects of the model.

4.2.1 Boundary conditions

Three-dimensional simulations are required because separated flows have 3D structures. A periodic condition is used in the spanwise direction (z-direction is the frame of reference

given in Figure 4.1). The periodic boundary condition is specified by applying the `cyclic` patch type at the front and back faces of the computational domain. As a result, the solution is repeating regularly in the spanwise direction. This boundary condition is used since the purpose of the simulations is not to capture the wing-tip vortices appearing in wings with a finite span.

The size of the computational domain is similar to the one used in Chapter 3 (see Figure 4.1). The edge of the domain is circular in the *xy*-plane because an O-type grid is more suitable for the airfoil with a blunt trailing edge.

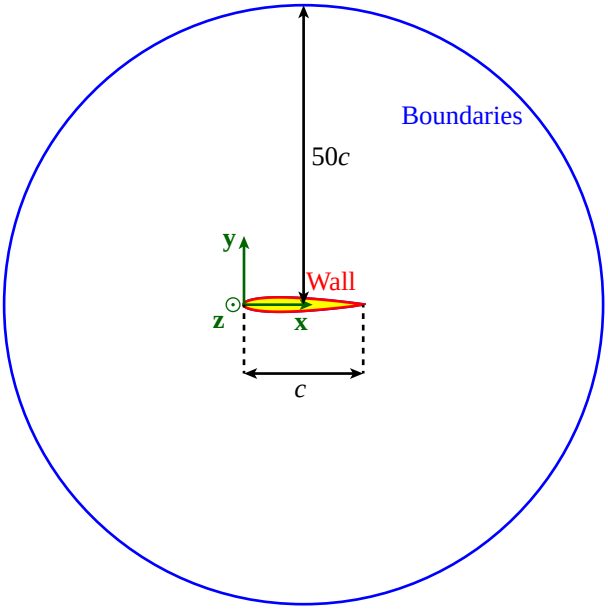

Figure 4.1: Domain size in the *xy*-plane for the NACA 0012 airfoil at high angle of attack case.

4.2.2 Initial conditions

A RANS solution is used as an initial condition to start the DDES calculations even if RANS simulations are not able to predict complex flows with massive separation regions accurately as it will be shown in Section 4.3.

4.2.3 Mesh description

DDES is non-zonal, i.e., there is no explicit interface between the two branches of this hybrid LES–RANS approach in the mesh. So, the advantage is that a precise knowledge about the characteristics of the flow (e.g., the thickness of the boundary layer) is not

necessary for the construction of the mesh. The computational domain has no explicit well-defined RANS regions and LES regions. However, the resolution of the mesh has to be fine enough in regions of interest. The DES grids used in this thesis are constructed following the guidelines given in [20].

The first mesh (Mesh I) is based on the one used in the reference paper [19] in order to compare the different numerical results. The cases using Mesh I are performed to validate our numerical model.

The O-type grid seen in the *xy*-plane is shown in Figure 4.2. A DES grid differs from a LES one in boundary layers as explained in Chapter 2 (see Figure 2.1). Flattened mesh cells are used near the wall. The first grid points away from the wall are set at $y/c = 10^{-4}$ in order to satisfy the criterion given in Equation (3.2). This condition can be verified a posteriori using the command `yPlusLES` of OpenFOAM.

Mesh I has 154 points around the airfoil . The points are clustered near the leading and trailing edges. The number of points in the spanwise direction is 25. The grid is stretched in the wall normal direction with a stretching ratio of 1.2 near the wall. The stretching ratio is then reduced to obtain more isotropic cells in regions of separated flow.

For the grid refinement study, the first mesh is refined in the three directions simultaneously (see Table 4.2). Numerical errors due to discretization are reduced when a mesh is refined.

Mesh	Number of points: around the airfoil	in the normal direction	in the spanwise direction	Number of hexahedra
Mesh I	154	76	25	277,200
Mesh II	206	94	33	613,056
Mesh III	252	110	41	1,098,720
Mesh IV	310	129	50	1,944,320

Table 4.2: Grids used for the grid refinement study. The spanwise period is equal to c. The number of cells increases from Mesh I to Mesh IV.

4.2.4 Numerical schemes

An example of the `fvSchemes` file of an OpenFOAM DDES case is available in Appendix A on page 84. The `fvSchemes` file specifies the numerical schemes.

An implicit second-order backward scheme is used for the time integration. The stability of implicit schemes is better and a larger time step can be used compared to explicit schemes.

Second order schemes are used for the discretization of spatial derivatives as first order schemes are too dissipative numerically, which is inadequate for time-dependent

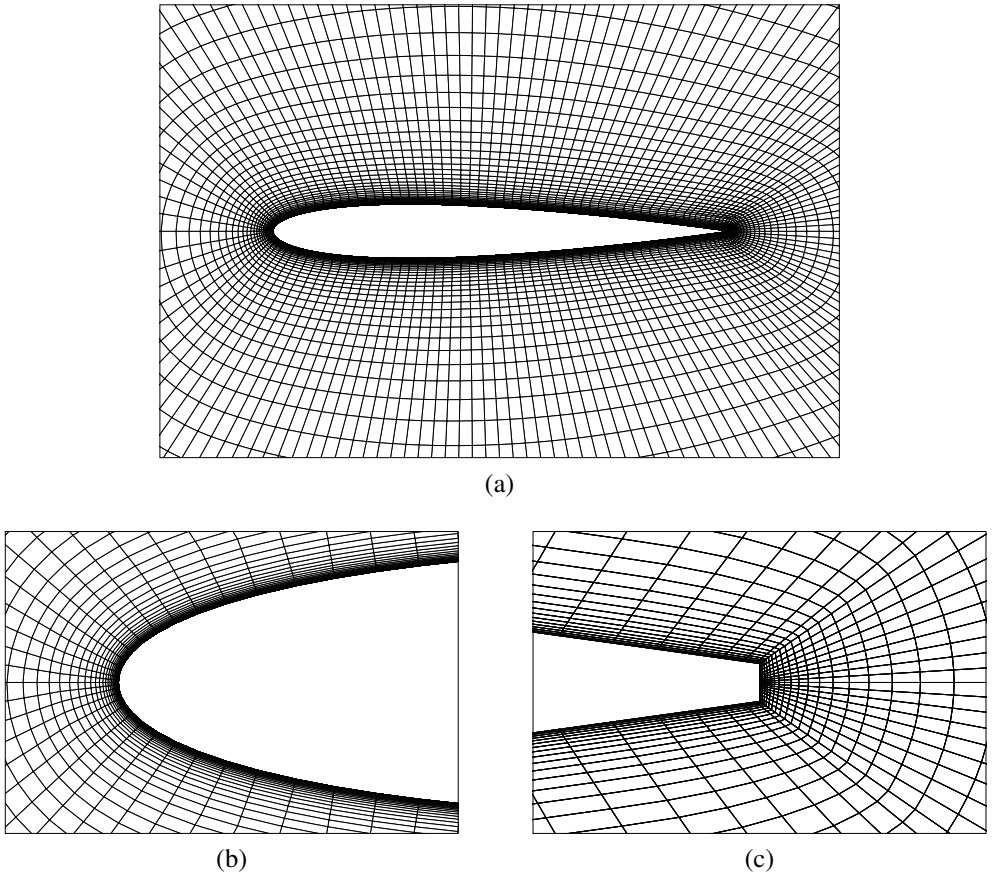

Figure 4.2: Mesh I in the *xy*-plane. Close-up views: (a) around the NACA 0012 airfoil, (b) near the leading edge and (c) near the blunt trailing edge.

problems.

For derivative terms, the standard Gaussian finite volume integration (second order) is chosen for the discretization scheme. As described in [6], the Gaussian integration is based on the summation of values on cell faces that are obtained by interpolation from cell centers.

The `linear` interpolation scheme of OpenFOAM (central differencing) is used for the interpolation of values from cell centers to face centers except for convection terms where convection-specific schemes are used (see `divSchemes` which includes the divergence terms). For example, the Linear-Upwind Stabilized Transport (`LUST`) interpolation scheme can be used in combination with the Gaussian discretization for the convection term of the Navier-Stokes equations. This scheme corresponds to a blend of the `linear-upwind` interpolation scheme with the `linear` one and it has a second order behavior [6]. The scheme is reported to perform well for the LES and DES techniques for external aerodynamics problems as stated in [6]. Diffusion terms are discretized using a central second order scheme. Default parameters are kept for all other entries.

4.2.5 Solution and algorithm control

Partial differential equations are transformed to systems of algebraic equations. There are as many equations as unknowns.

An example of the `fvSolution` file of an OpenFOAM DDES case is available in Appendix A on page 86. The `fvSolution` file specifies the solvers and the associated tolerances and the algorithms. Linear system solvers have to be chosen to compute the quantities. The chosen linear solver to compute the pressure is the Preconditioned Conjugate Gradient (`PCG`) with the Diagonal Incomplete Cholesky (`DIC`) preconditioner. For other variables, the linear solver is the Preconditioned Bi-Conjugate Gradient (`PBiCG`) with the Diagonal Incomplete LU (`DILU`) preconditioner. Preconditioners accelerate convergence by modifying the matrices. Small tolerances are specified for the iterative solvers to reduce iteration errors (see `fvSolution`).

The dominant CPU time is the one associated with the equation for pressure. Solvers influence the rate of convergence. However, if the results present major inaccuracies from a physical point of view, it is not because of the choice of solvers.

The Pressure Implicit Split Operator (PISO) algorithm designed for unsteady problems is used. The transient solver for incompressible turbulent flows of OpenFOAM is called `pisoFoam`.

The choice of the time step Δt is governed by the smallest time scale of the flow that needs to be resolved (physical time step) and the numerical time step for stability. With the data given in Table 4.1, the time step is set to 0.004 s for Mesh I and it has to be

reduced to 0.001 s for Mesh IV in order to have a stable computation. These values of the time step give a Courant-Friedrichs-Lewy (CFL) number of the order of 1 around the airfoil and of the order of 10 in small regions near the leading and trailing edges. The CFL number for the stability condition depends on the flow velocity, the time step and the grid spacing.

Three-dimensional flows require a lot of computing power. The computation is parallelized in order to, on the one hand, decrease the total execution time and, on the other hand, solve such a big problem[1]. OpenFOAM uses the Message Passing Interface (MPI) standard which is the most widely used standard for parallel computing. The computational domain is decomposed and it is distributed on several processors. Each processor computes a subproblem and the processes communicate with each other.

The time step, the number of cores used for the computations and the computation time associated with each DDES case presented in the present chapter are given in Appendix A.

4.3 Results

For a three-dimensional wing, the lift coefficient C_L is defined as follows:

$$C_L = \frac{L}{\frac{1}{2}\rho_\infty U_\infty^2 S} \tag{4.1}$$

where the reference area S is the planform area of the wing. The drag coefficient C_D is given by

$$C_D = \frac{D}{\frac{1}{2}\rho_\infty U_\infty^2 S} \tag{4.2}$$

In what follows, the transient part of the results has been removed to compute the statistics of the aerodynamic force coefficients.

A long simulation time is required in order to compute the time-averaged solutions. The temporal average of the dimensionless force coefficients $\overline{C_L}$ and $\overline{C_D}$ and the associated standard deviations S_{C_L} and S_{C_D} are evaluated using a time interval of 300 s (from $t = 200$ s to $t = 500$ s) as a moving average filter applied to $C_L(t)$ and $C_D(t)$ shows that the mean values are nearly constant on the considered time interval (see Figure 4.3, for example)[2].

[1] "Computational resources have been provided by the Consortium des Équipements de Calcul Intensif (CÉCI), funded by the Fonds de la Recherche Scientifique de Belgique (F.R.S.-FNRS) under Grant No. 2.5020.11".

[2] In the graphs, the blue curves are related to C_L and the red ones to C_D.

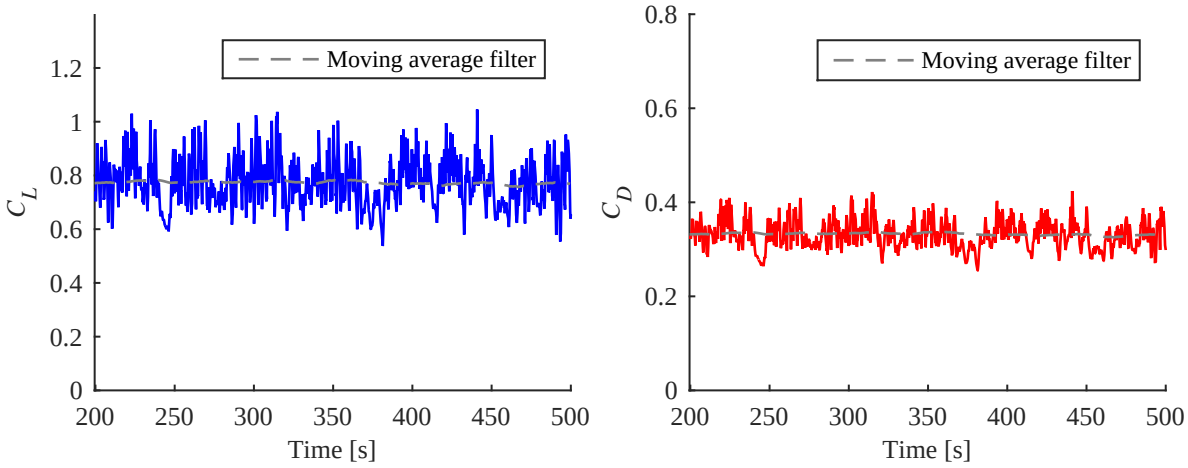

(a) (b)

Figure 4.3: Evolution of the aerodynamic force coefficients of the NACA 0012 airfoil at $\alpha = 20°$ obtained by DDES: (a) Lift coefficient as a function of time. (b) Drag coefficient as a function of time. The length of the moving average filter is 100 s.

Table 4.3 contains the statistics of the aerodynamic force coefficients obtained with Mesh I and from two different simulation approaches: the Unsteady RANS (URANS) simulation using the Spalart-Allmaras turbulence model and the DDES technique also based on the S-A model. The angle of attack α varies from 8° to 60°.

Model	α	$\overline{C_L}$	S_{C_L}	$\overline{C_D}$	S_{C_D}
URANS S-A	8°	0.7881	≈ 0	0.0246	≈ 0
	20°	0.7044	0.0011	0.3009	0.0004
	45°	1.3953	0.2066	1.4499	0.1836
	60°	1.3155	0.2078	2.3119	0.2529
DDES	8°	0.7946	≈ 0	0.0233	≈ 0
	20°	0.7716	0.0865	0.3318	0.0294
	45°	1.1321	0.2497	1.1646	0.2434
	60°	1.0360	0.2307	1.7735	0.3716

Table 4.3: Results for the airfoil at high angles of attack.

The RANS and DDES calculations are performed with the same code, which is better for the comparison of the results of the two approaches.

4.3.1 Comparison with the experimental and numerical data

Figures 4.4 and 4.5 contain the values of C_L and C_D measured experimentally and those predicted numerically.

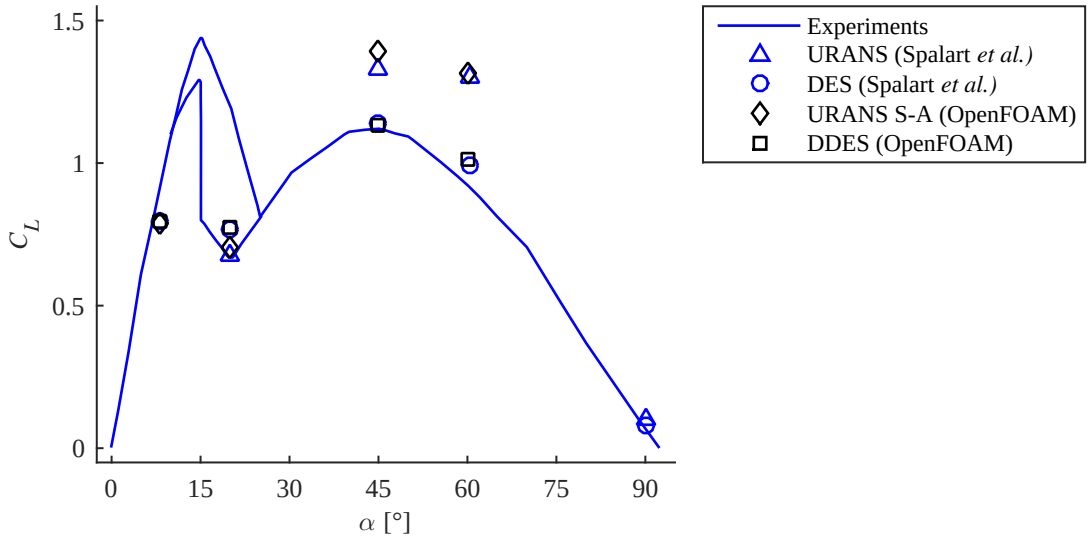

Figure 4.4: Lift coefficient of the NACA 0012 airfoil as a function of the angle of attack, adapted from [19]. The black symbols represent the numerical results obtained by the present work.

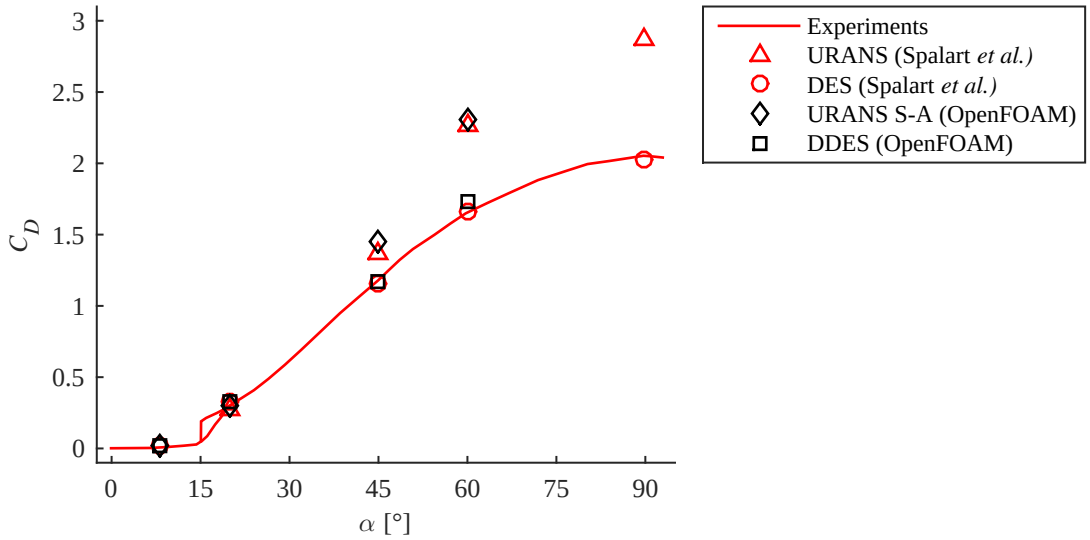

Figure 4.5: Drag coefficient of the NACA 0012 airfoil as a function of the angle of attack, adapted from [19]. The black symbols represent the present numerical results.

The two curves in the 13° to 25° range represent the experimental scatter. An estimation of the experimental scatter is not available for higher angles of attack. Errors and uncertainties associated with the experiments must also be taken into account (e.g., the level of noise in the experimental measurements).

In the present case, a reduction of the lift coefficient occurs when the angle of attack exceeds the stall angle equals to about 15°. This phenomenon due to a separation of the flow on the upper surface of the wing corresponds to the stall. The drag increases significantly beyond the maximum lift coefficient $C_{L_{\max}}$. The lift curve has a local maximum in the vicinity of α equals 45°. For α greater than 45°, the drag predominates and it increases until α equals 90° where it reaches its maximum ($C_{D_{\max}} \approx 2$).

For an angle of attack of 8°, the standard deviations S_{C_L} and S_{C_D} are approximately zero indicating that the flow is statistically steady. The boundary layer remains attached over a large surface of the wing and the results obtained by the RANS and DDES calculations are almost identical. The numerical predictions obtained by RANS are reliable at low angle of attack, which is consistent with the conclusions of Chapter 3.

For an angle of attack higher than about 15°, the solution is clearly unsteady and unsteady computations have to be considered.

From Table 4.3, it can also be seen that for a given span length, the standard deviations increase if the angle of attack increases from 8° to 45° pointing out that the fluctuations of the flow are higher as the regions of separated flow become larger.

URANS simulations

In this chapter, the URANS simulations are two-dimensional. A tree-dimensional URANS simulation will be presented in Chapter 5.

Figures 4.4 and 4.5 show that the URANS predictions given by OpenFOAM as well as those obtained by Spalart *et al.*, which are quite similar, are in poor agreement with the experimental data. The aerodynamic force coefficients are highly overestimated when the flow is massively detached ($\alpha = 45°$ and 60°). For $\alpha = 45°$, the relative error with respect to the experimental value exceeds 20% for both $\overline{C_L}$ and $\overline{C_D}$.

For instance, at $\alpha = 60°$, URANS predicts a periodic solution even if the turbulent flow is highly irregular. Figure 4.6 shows that the dimensionless force coefficients are periodic but they do not correspond to a pure sine function.

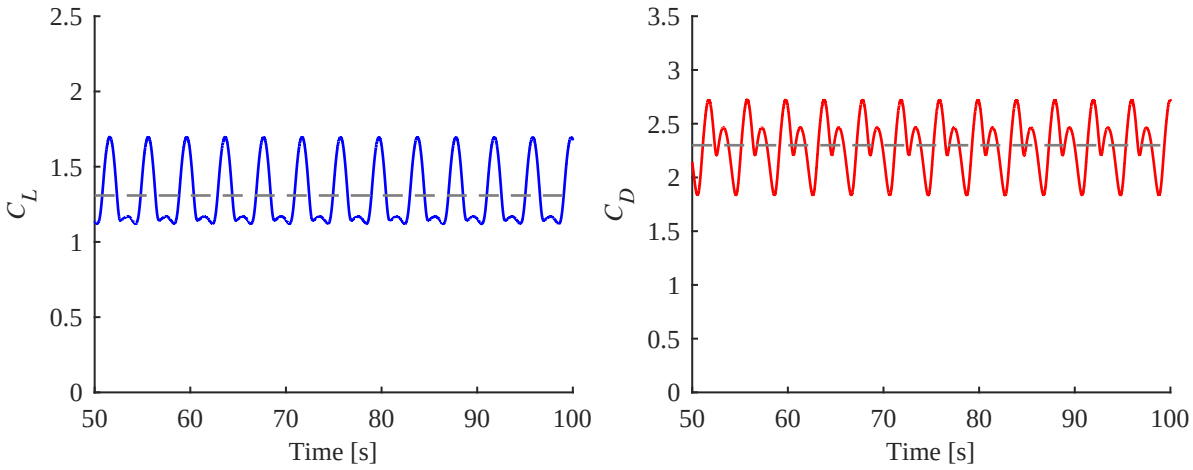

Figure 4.6: Evolution of the aerodynamic force coefficients of the NACA 0012 airfoil at $\alpha = 60°$ obtained by URANS.

Welch's method

The fast Fourier transform directly applied to the aerodynamic force signals yields noisy results, especially when the signals contain random fluctuations (DDES results). The power spectral density of a signal is estimated more properly using the Welch's method, the original paper is cited in the bibliography [27].

The basic idea of the Welch's method consists in sectioning the signal. The time interval of each segment is specified depending on the duration of the entire signal. Then, a modified periodogram of each segment is computed. Averaging these modified periodograms gives the estimate of the power spectral density of the signal. The noise level in the estimated power spectra is reduced with this method.

Also, the segments generally overlap and they are usually multiplied by a window function (e.g., the Hanning window) to avoid sharp truncations of the sequence.

The lift coefficient is an image of the periodic variation of the flow in the wake. Figure 4.7 shows the power spectral density of the lift coefficient estimated by the Welch's method. In the frequency domain, the magnitude of the second harmonic ($f_2 = 0.5$ Hz) is not negligible compared to the magnitude of the fundamental frequency of the flow (first harmonic $f_1 = 0.25$ Hz).

DDES results

For angles of attack higher than the stall angle, the present DDES results are very close to the ones given by Spalart *et al.* as can be seen from Figures 4.4 and 4.5. Discretization

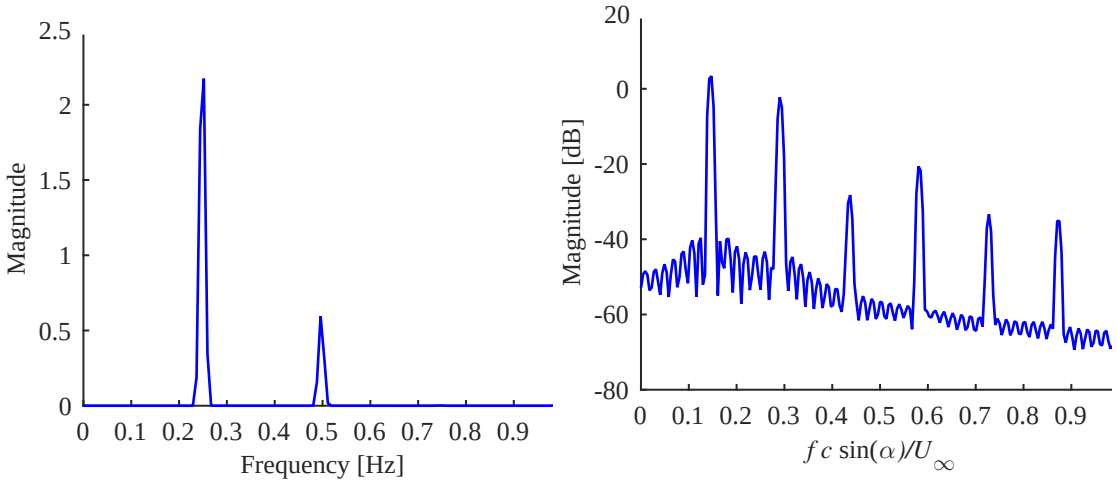

Figure 4.7: Power spectral density of $C_L(t)$ at $\alpha = 60°$ obtained by URANS.

errors or differences in the implementation may be the causes of the small differences. Another important observation is that the DDES predictions are much closer to the experimental measurements compared to the URANS results.

Figure 4.8 illustrates the flow separation on the extrados of the wing predicted by the DDES approach[3]: the streamlines separate from the wall of the body and a recirculating flow region is observed.

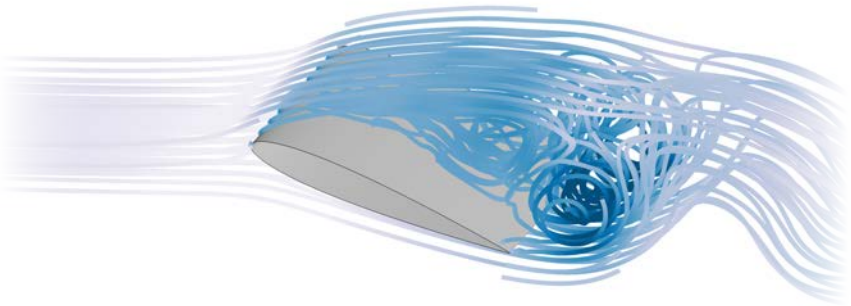

Figure 4.8: Streamlines around the wing at $\alpha = 20°$ obtained by DDES.

The flow separation is driven by the effect of viscosity. The adverse pressure gradient present on the upper surface of the airfoil is large enough to cause massive flow separation. The separation point corresponds to the point where the wall shear stress τ_w vanishes because $\left.\frac{\partial u}{\partial y}\right|_w = 0$.

[3]The figure in the cover page represents the streamlines around the wing at $\alpha = 60°$ obtained by DDES.

For the airfoil beyond the stall angle of attack, the aerodynamic forces are functions of time due to the flow separation which introduces unsteadiness.

It can be seen from Figure 4.5 that the point at $\alpha = 60°$ is the farthest from the experimental curve. Moreover, the difference between the URANS and DDES results is large for $\alpha = 60°$. The grid refinement analysis and the study of the influence of the span length will be made for this particular case.

4.3.2 Grid refinement study

A grid refinement decreases numerical errors. For RANS simulations, if the mesh is refined, the numerical solution converges to the exact solution of the RANS and S-A model equations. Once the grid convergence is achieved, the variation of the solution will be negligible if the grid is refined even more (grid independence). However, the turbulence model is not able to capture all the physics of turbulent flows. Consequently, accuracy cannot be improved unlimitedly by refining the mesh with RANS simulations; this is not the case with LES or DES. It is for this reason that the grid refinement study is conducted only with the DDES approach.

Table 4.4 shows that the mean aerodynamic force coefficients $\overline{C_L}$ and $\overline{C_D}$ do not vary significantly when the grid is refined.

Mesh	$\overline{C_L}$	S_{C_L}	$\overline{C_D}$	S_{C_D}
Mesh I	1.0360	0.2307	1.7735	0.3716
Mesh II	1.0389	0.2235	1.7876	0.3709
Mesh III	1.0338	0.2062	1.7696	0.3315
Mesh IV	1.0347	0.2067	1.7643	0.3141

Table 4.4: Results of the grid refinement study ($\alpha = 60°$ and the length of the span is c).

The resolution of Mesh I is sufficient to predict the aerodynamic forces rather accurately. The mean values given by Mesh I and Mesh IV are quite similar, the relative errors are more noticeable for the standard deviations:

$$\varepsilon_{\text{rel},\overline{C_L}} = \left| \frac{\overline{C_{L_{\text{Mesh IV}}}} - \overline{C_{L_{\text{Mesh I}}}}}{\overline{C_{L_{\text{Mesh IV}}}}} \right| = 0.13\%, \qquad \varepsilon_{\text{rel},S_{C_L}} = \left| \frac{S_{C_{L_{\text{Mesh IV}}}} - S_{C_{L_{\text{Mesh I}}}}}{S_{C_{L_{\text{Mesh IV}}}}} \right| = 11.61\% \tag{4.3}$$

$$\varepsilon_{\text{rel},\overline{C_D}} = 0.52\%, \qquad \varepsilon_{\text{rel},S_{C_D}} = 18.31\% \tag{4.4}$$

The study of the influence of the length of the span is carried out with Mesh I to limit the computational cost.

Vortex identification

Vortices of incompressible flows can be identified using the Q-criterion. An eddy corresponds to a region where Q, the second invariant of the velocity gradient tensor $\nabla\mathbf{u}$, is positive [12]:

$$Q = \frac{1}{2}\left(u_{i,i}^2 - u_{i,j}u_{j,i}\right) = -\frac{1}{2}u_{i,j}u_{j,i} = \frac{1}{2}\left(\|\Omega\|^2 - \|\mathbf{S}\|^2\right) > 0 \tag{4.5}$$

where

$$\|\mathbf{S}\| = [\mathrm{tr}(\mathbf{S}\mathbf{S}^T)]^{1/2}, \qquad S_{ij} = \frac{1}{2}(u_{i,j} + u_{j,i}) \tag{4.6}$$

$$\|\Omega\| = [\mathrm{tr}(\Omega\Omega^T)]^{1/2}, \qquad \Omega_{ij} = \frac{1}{2}(u_{i,j} - u_{j,i}) \tag{4.7}$$

So, the vorticity magnitude is greater than the shear strain rate for the regions verifying this criterion.

Turbulence is modeled with the URANS simulations and only unsteady mean flow structures are captured. This characteristic can be visualized using the Q-criterion: Figure 4.9 shows the vortex shedding identified by positive isosurfaces of Q.

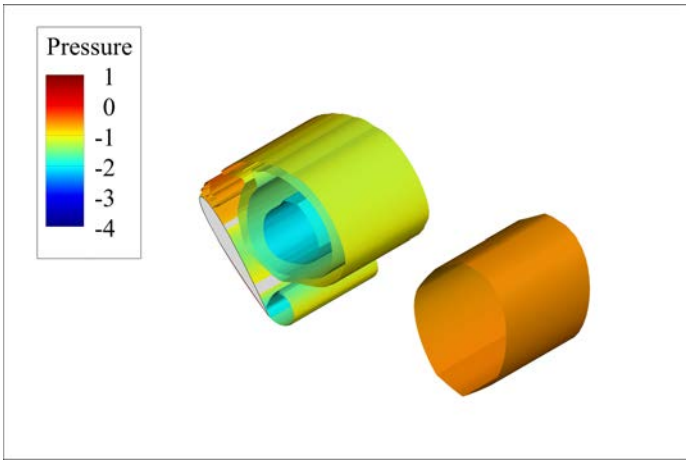

Figure 4.9: Surfaces of $Q = 1$, 5 and 10 colored with the kinematic pressure [m^2/s^2] at $\alpha = 60°$ (2D URANS).

The pressure in a vortex core is lower than the reference pressure. The flow remains attached on the lower surface of the airfoil.

Figure 4.10 illustrates that smaller scales in space are captured by finer meshes with the DDES approach.

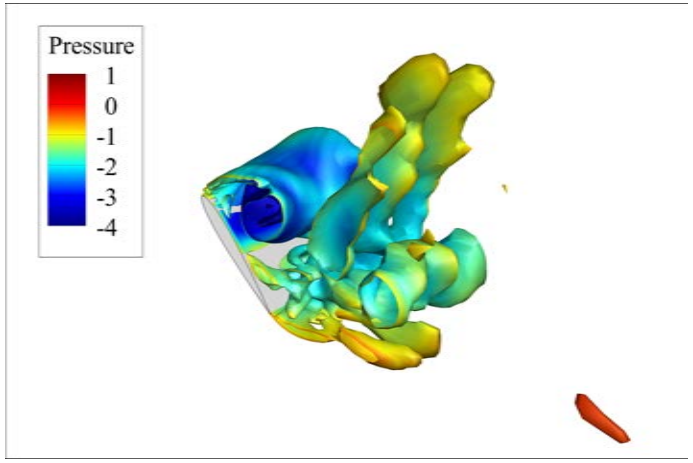

(a) DDES, Mesh I.

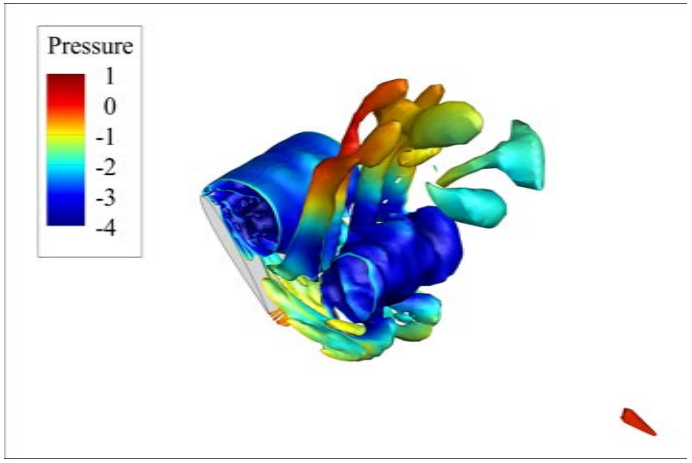

(b) DDES, Mesh II.

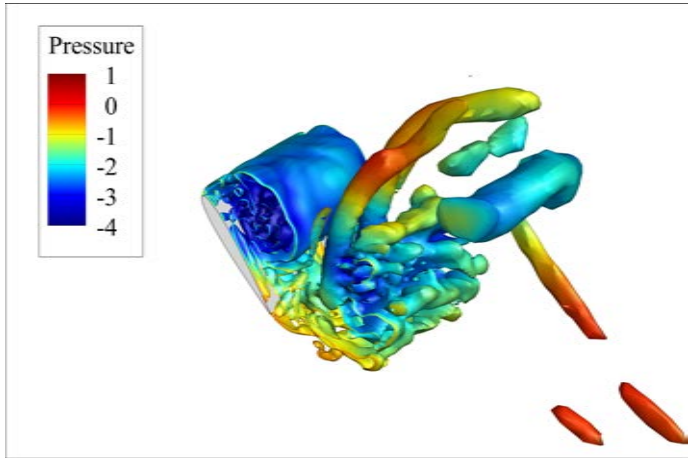

(c) DDES, Mesh III.

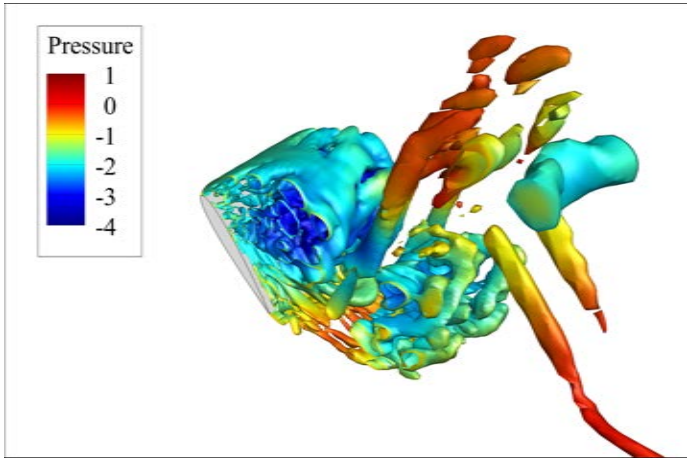

(d) DDES, Mesh IV.

Figure 4.10: Surface of $Q = 10$ colored with the kinematic pressure $[m^2/s^2]$ at $\alpha = 60°$ (DDES). Four different meshes are used: the number of cells increases from Mesh I to Mesh IV.

The turbulent eddies visualized by the Q-criterion are smaller if the number of grid points is augmented from Mesh I to Mesh IV. Eddies are not very fine with Mesh I. The accuracy of DDES in predicting the massively separated flow is improved with finer meshes since smaller eddies are resolved by the LES mode of DDES.

From Figure 4.10, it can be concluded that the physical approximation of two-dimensionality does not hold any more at high angles of attack.

4.3.3 Influence of the spanwise period of the computational domain

In this part, the span is increased to quantify the effect of the flow structures determined in a larger computational domain. In what follows, the resolution of Mesh I is used for the analysis as mentioned above.

Table 4.5 contains the statistics of $C_L(t)$ and $C_D(t)$ for different spanwise periods of the computational domain: c, $2c$ and $4c$. It can be inferred that the standard deviations S_{C_L} and S_{C_D} decrease when the span length increases indicating that the amplitudes of the variations of the aerodynamic force coefficients decrease (the data points are closer to the corresponding mean value, they are less dispersed). Also, the mean values $\overline{C_L}$ and $\overline{C_D}$ are slightly reduced if the span is longer.

Length of the span	$\overline{C_L}$	S_{C_L}	$\overline{C_D}$	S_{C_D}
c	1.0360	0.2307	1.7735	0.3716
$2c$	0.9634	0.1267	1.6395	0.1934
$4c$	0.9539	0.1110	1.6220	0.1701

Table 4.5: Results for different spanwise periods ($\alpha = 60°$ and the resolution of Mesh I is used for the DDES calculations).

Figure 4.11 shows the evolution of the lift and drag signals over time. A diminution of the amplitudes of the fluctuations is observed when the span length is increased.

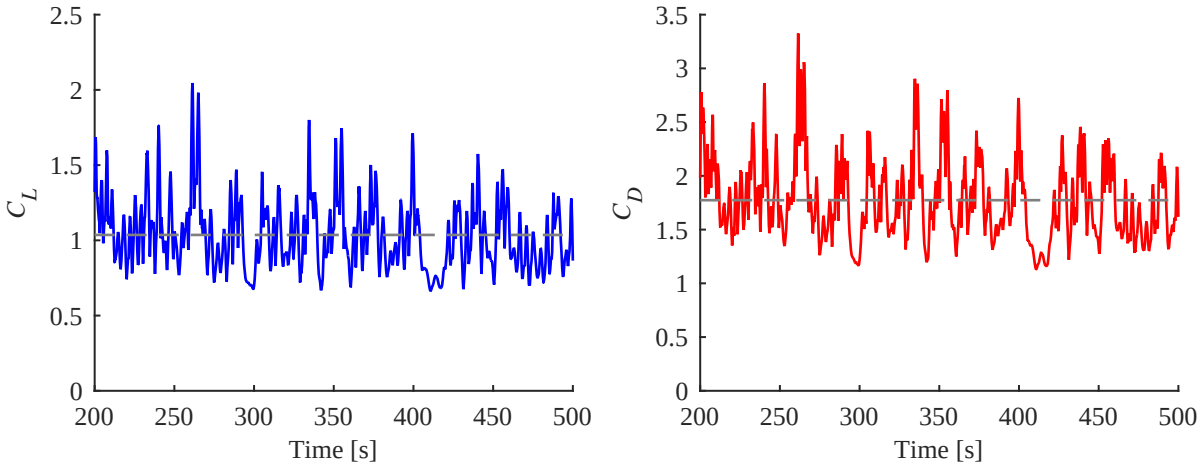

(a) DDES, span = c.

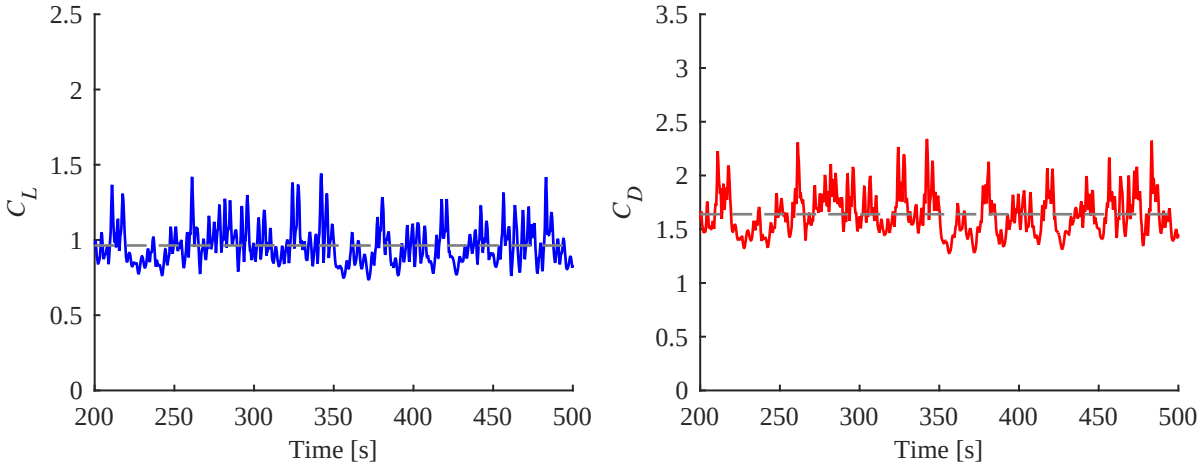

(b) DDES, span = $2c$.

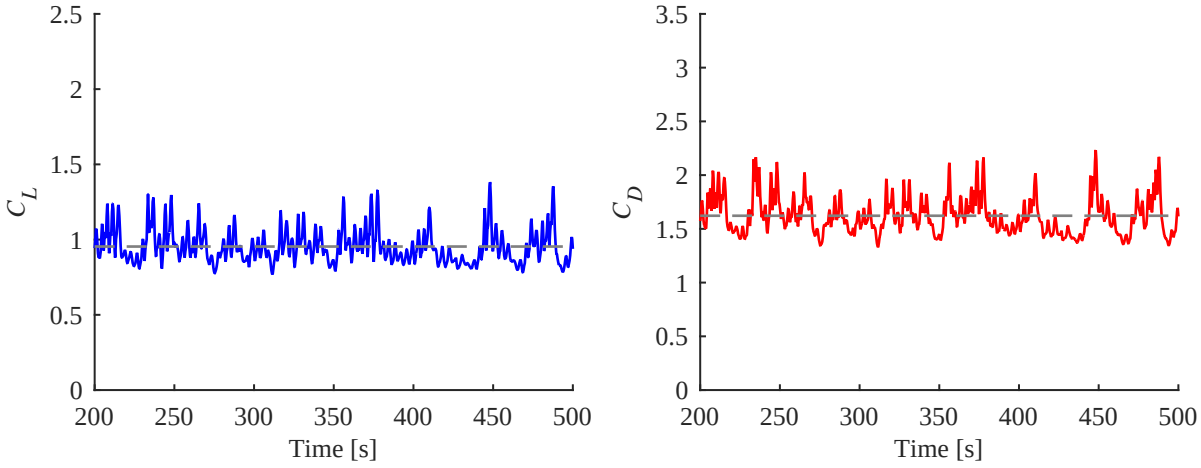

(c) DDES, span = $4c$.

Figure 4.11: Evolution of the aerodynamic force coefficients of the NACA 0012 airfoil at $\alpha = 60°$ for different spanwise periods obtained by DDES: (left) Lift coefficient as a function of time. (right) Drag coefficient as a function of time.

The numerical values tend to converge to the experimental values when the length of the span is increased as can be seen more clearly in Figure 4.12. The numerical predictions obtained by DDES for a span of $4c$ correspond quite well to the experimental measurements.

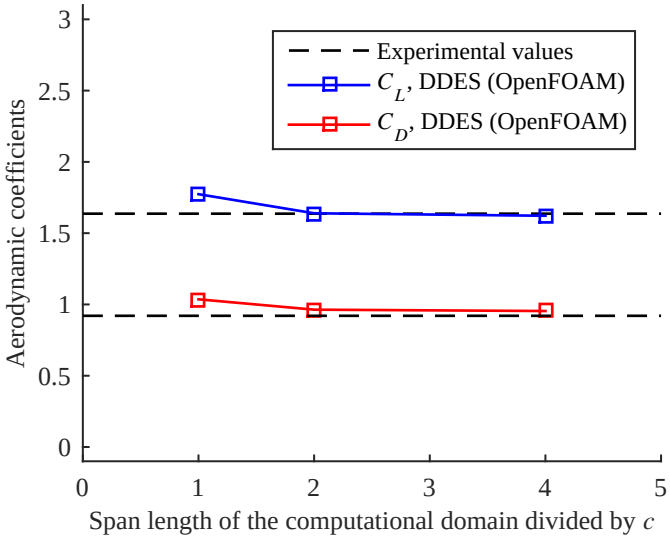

Figure 4.12: Aerodynamic force coefficients of the NACA 0012 airfoil for different spanwise periods. Comparison with the experimental measurements.

Due to three-dimensional effects, a vortex which is shed downstream is not exactly at the same phase everywhere along the span. As an example, Figure 4.13 shows a leading-edge vortex at a given time to illustrate this idea. It can be seen that the part of the vortex seen in the plane $z = c$ is slightly shifted compared to the one in the plane $z = 2c$ or $z = 3c$. In the example of Figure 4.13, the visualization of the z-component of the vorticity ω_z reveals that the leading-edge vortex in $z = c$ detaches from the body and the formation of the trailing-edge vortex begins. By contrast, the leading-edge vortex in $z = 3c$ is closer to the airfoil and the trailing-edge vortex is not yet visible at this particular instant.

The variations of the dimensionless force coefficients are partly connected to the vortex-shedding process (the relation will be explained in Chapter 6 for an inclined flat plate configuration). The 3D effects (the deviations) become more important when the span is longer and the spanwise average used to compute the global quantities C_L and C_D reduces the amplitudes of the fluctuating part of the aerodynamic force coefficients. A diminution of the time-averaged dimensionless force coefficients is also observed.

The spanwise vorticity ω_z over the lower surface of the airfoil is insignificant (see Figure 4.13).

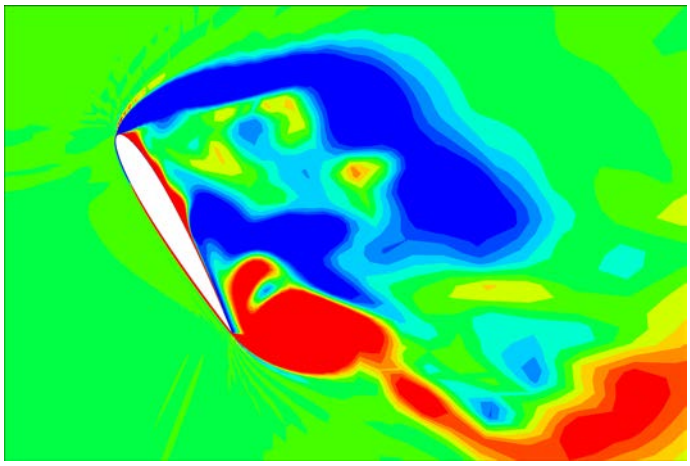

(a) $z/c = 1$.

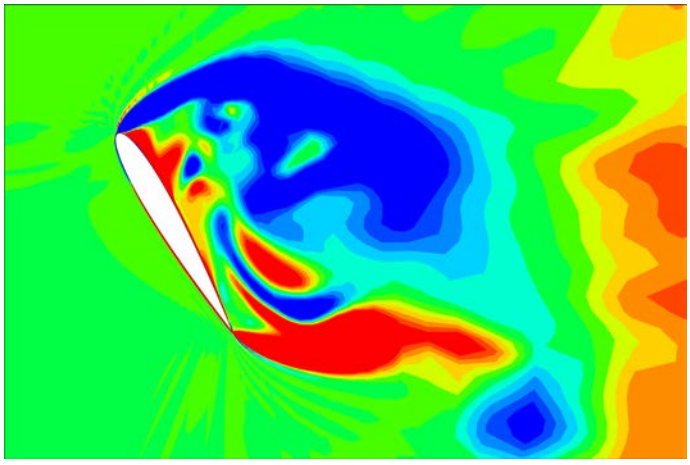

(b) $z/c = 2$.

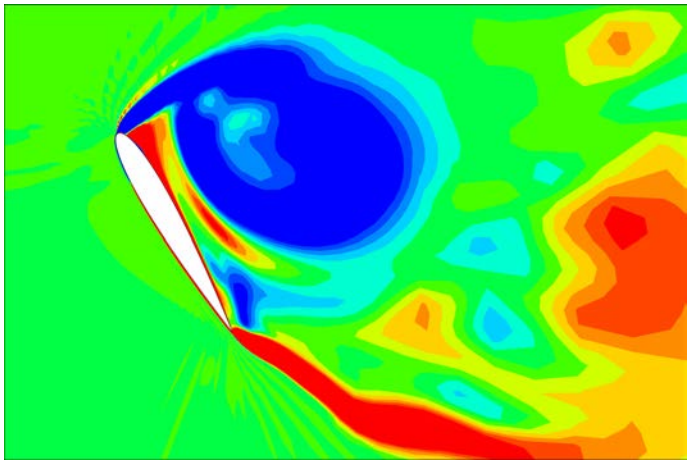

(c) $z/c = 3$.

Figure 4.13: Contours of the z-component of the vorticity ω_z in several slices in the xy-plane at an instant of time (obtained by DDES using the resolution of Mesh I with a span length of $4c$).

To sum up, a poor agreement is found between the unsteady RANS results and the experimental measurements of the aerodynamic force coefficients. However, the RANS simulations are much cheaper than the DDES computations. So, the RANS approach may be interesting to obtain orders of magnitude rapidly but a higher fidelity approach is required to achieve engineering accuracy.

The present DDES predictions are consistent with the numerical results obtained by a similar approach [19]. Therefore, the present numerical models can be validated. Moreover, the accuracy of the dimensionless force coefficients predicted by the DDES approach is superior compared to the URANS simulations as they are in much better agreement with the experimental data.

If the mesh is refined, the accuracy of the results obtained by DDES is better as smaller eddies are captured but the computational cost increases, i.e., there is a trade-off between computing power and fidelity.

The DDES results reveal the three-dimensional character of the separated flow around the airfoil at high angle of attack. A vortex is not constant along the span; 3D effects and instabilities appear. The length of the span must be long enough to capture the longer wavelengths of these 3D instabilities and the resolution of the grid must be fine enough to capture the details of the physics of the turbulent flow.

The length of the span of the computational domain is an important factor to predict the aerodynamic forces reliably. Ideally, the span length should be chosen as close as possible to the geometry considered in the experiment or in the real flow problem.

Chapter 5

Delayed detached-eddy simulation of a flat plate at high angle of attack

Now that the choice of all simulation parameters has been presented and a validation study has been carried out in Chapter 4, the DDES technique is applied to another configuration: the flow around a flat plate at high angle of attack.

Once again, the statistics of the aerodynamic force coefficients obtained by numerical simulations (DDES and URANS) and measured experimentally are compared to verify that there is no major discrepancy between the different approaches.

Then, the physics of the flow is studied in more detail compared to the previous configuration as it will be presented in Chapter 6 which is actually complementary to the present chapter.

5.1 Configuration description

5.1.1 Experimental data

For this part, the experimental data are provided by Amandine Guissart from the MTFC research group of the University of Liège. Aerodynamic force measurements are available. In addition, the Particle Image Velocimetry (PIV) technique has been used. These experimental measurements are used to validate the numerical methods.

PIV is a flow visualization technique used to determine a velocity field like a numerical simulation. The available PIV results for comparison are 2D: the velocity field is determined in a slice normal to the span (the velocity vectors have two components; the component in the spanwise direction is not measured). Therefore, the Dynamic Mode Decomposition (DMD) of the CFD results, which will be explained in Chapter 6, will also be performed in a 2D slice to compare the coherent features of the separated flow predicted numerically with those obtained from experimental measurements.

In the experiments, it is not possible to know exactly the duration of the vortex-shedding period if the flat plate is static because the vortex-shedding process is not perfectly periodic. The shedding period changes slightly over time and these variations are random. Therefore, it is not possible to have the same phase over several periods when the measurement is taken.

Small vibrations at the frequency corresponding to the mean Strouhal number are imposed, so that the vortex shedding is forced at the imposed frequency. This situation is referred to as the *forced case* in the following sections. With the forced case, the PIV images can be taken at known phases over several periods. The PIV measurements are available for the forced case but the level of noise is higher in the force signals compared to the static case. Moreover, a deformation of the mesh to simulate an oscillating body is out of the scope of this present work, so that the parameters for the numerical simulations are based on the static case of the experiments. Nevertheless, a qualitative comparison with the forced case is presented in Chapter 6 to check the coherence of the numerical predictions.

In the experiments, the length of the chord c_{exp} is 7.62 cm (8 inches), the length of the span b_{exp} is 59 cm, which gives an aspect ratio $AR_{\text{exp}} = b_{\text{exp}}/\bar{c}_{\text{exp}}$ of about 7.7. The thickness t_{exp} is $6.25\%\, c_{\text{exp}}$. Two different values are used for the Reynolds number: 2×10^4 and 4×10^4 (see Table 5.3).

5.1.2 Configuration used for the numerical simulations

The Reynolds number based on the chord length is 2×10^4 (the computational cost is therefore reduced compared to the previous configuration). The thickness t is equal to 6.25% of the chord length c and the edges are rounded (semicircles) as can be seen in Figure 5.1.

Figure 5.1: Geometry of the flat plate.

The angle of attack α is constant and it is equal to 30°.

5.2 Numerical model

The numerical parameters of the present case (fluid properties, boundary conditions, numerical schemes and so forth) are the same than those described in Chapter 4. Only the

parameters specific to the inclined flat plate case are presented in this section.

The radius of the computational domain is set to $50c$ (see Figure 5.2).

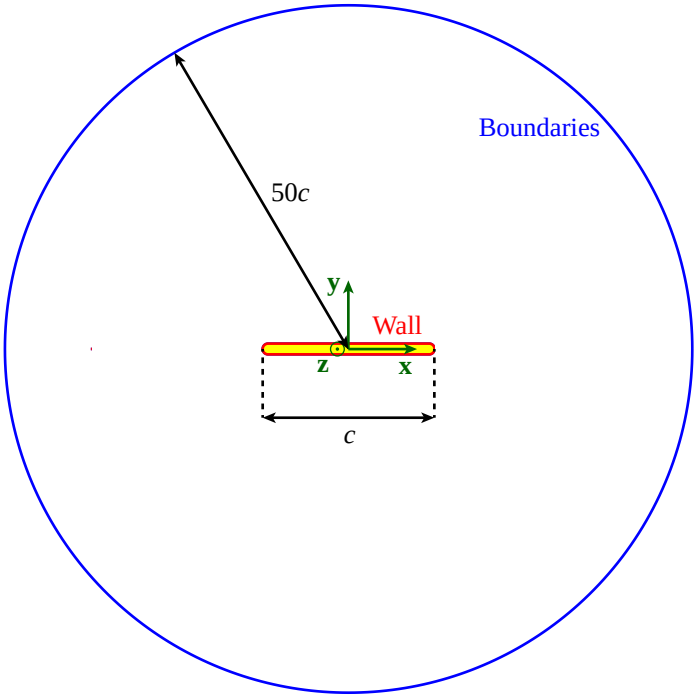

Figure 5.2: Domain size in the xy-plane for the inclined flat plate case.

5.2.1 Mesh description

Flattened mesh cells are used near the wall. The first grid points away from the wall are set at $y/c = 3.8 \times 10^{-4}$ in order to satisfy the criterion given in Equation (3.2).

The resolution of the mesh is shown in Figure 5.3 and it is similar to Mesh II used in Chapter 4.

Three different span lengths are considered: c, $4c$ and $8c$. The meshes do not change over time; the flat plate remains static. The characteristics of these meshes are given in Table 5.1.

5.3 Results

The quality of the predictions given by the numerical simulations is evaluated by comparing the mean dimensionless force coefficients and the corresponding standard deviations,

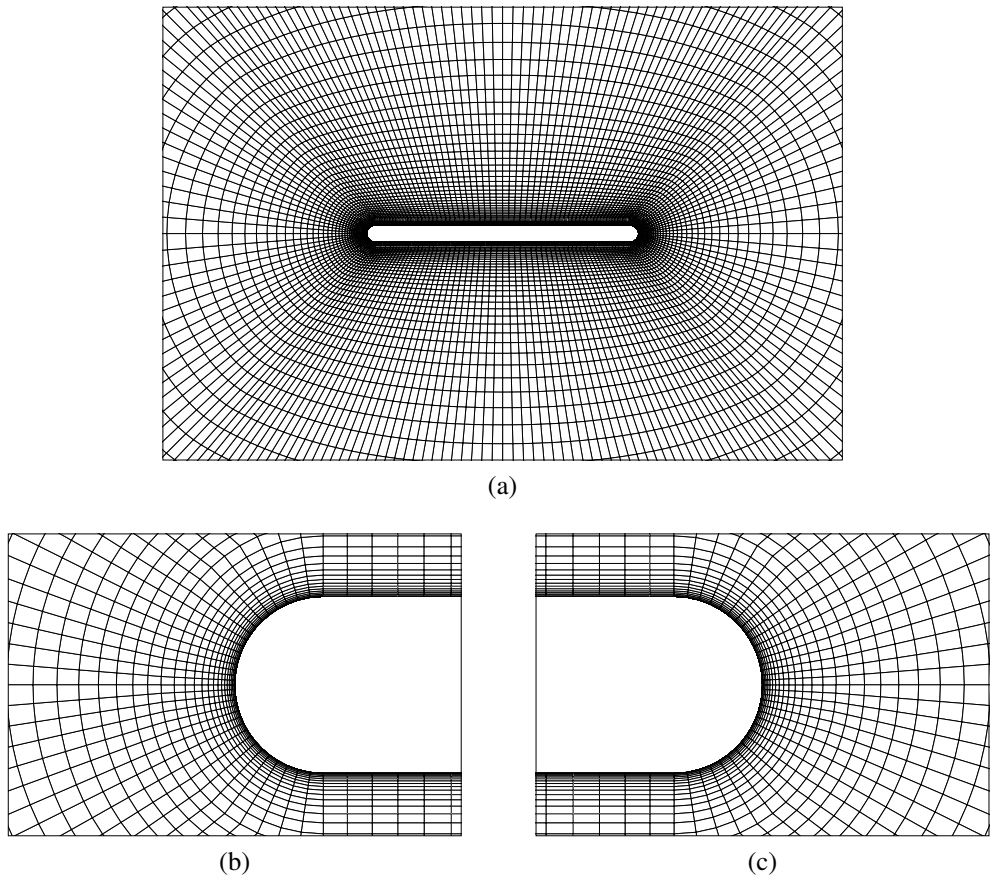

Figure 5.3: Grid in the *xy*-plane. Close-up views: (a) around the flat plate, (b) near the leading edge and (c) near the trailing edge.

Spanwise period	Number of points:			Number of hexahedra
	around the plate	in the normal direction	in the spanwise direction	
c	200	86	32	527,000
$4c$	200	86	128	2,159,000
$8c$	200	86	256	4,335,000

Table 5.1: Characteristics of the grids used for the inclined flat plate case.

the Strouhal number and the separated flow structures (in Chapter 6) with the experimental results.

The unsteadiness of the separated flow is measured by the dimensionless Strouhal number St which is calculated by

$$\mathrm{St} = \frac{f_s \, c \sin \alpha}{U_\infty} \tag{5.1}$$

where f_s stands for the fundamental frequency of the flow and $c \sin \alpha$ is the chosen characteristic dimension (in the experiments as well as in the numerical simulations).

For the DDES cases, a time-averaged solution is calculated over a duration of 850 s ($\approx$ 76 cycles). This time interval appears to be sufficient to have converged results for the DDES calculation using the mesh with a span length of $8c$, which is the closest to the geometry used in the experiments, as can be inferred from Figure 5.4 and Table 5.2

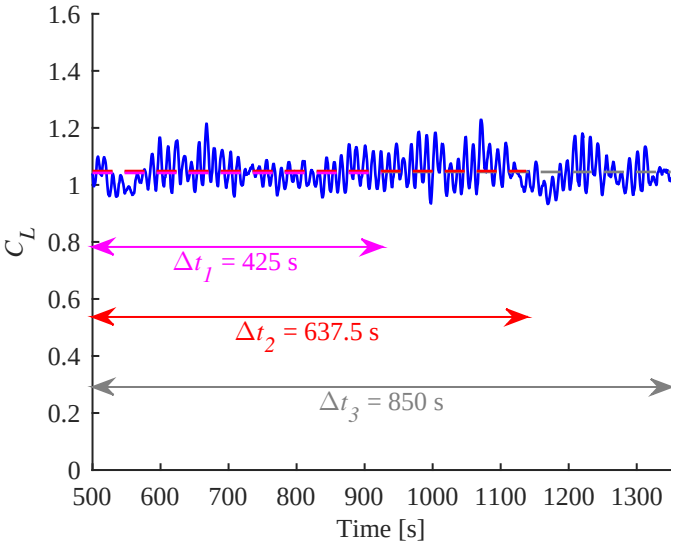

Figure 5.4: Time intervals used to evaluate the temporal average of $C_L(t)$.

Interval	$\overline{C_L}$	$\overline{C_D}$
$\Delta t_1 = 425$ s	1.0419	0.6373
$\Delta t_2 = 637.5$ s	1.0486	0.6414
$\Delta t_3 = 850$ s	1.0455	0.6395

Table 5.2: Mean lift and drag coefficients as functions of the considered time interval.

5.3.1 Comparison with the experimental measurements

Table 5.3 summarizes the results found for the present configuration.

Model	Re	$\overline{C_L}$	S_{C_L}	$\overline{C_D}$	S_{C_D}	St
Experiment (static)	2×10^4	1.05	0.05	0.62	0.04	0.158
Experiment (static)	4×10^4	0.97	0.04	0.62	0.03	0.159
Experiment (forced)	4×10^4	1.05	0.07	0.67	0.05	0.156
2D URANS	2×10^4	1.1805	0.1943	0.7403	0.0667	0.152
3D URANS (span = $8c$)	2×10^4	1.1881	0.1801	0.7434	0.0623	0.151
DDES (span = c)	2×10^4	1.1471	0.1873	0.7089	0.0873	0.152
DDES (span = $4c$)	2×10^4	1.0625	0.0839	0.6499	0.0412	0.151
DDES (span = $8c$)	2×10^4	1.0455	0.0526	0.6395	0.0249	0.151

Table 5.3: Results for the flat plate at high angle of attack ($\alpha = 30°$).

URANS simulations

The two-dimensional unsteady RANS predictions of the dimensionless force coefficients are globally higher than the experimental measurements. The same tendency was observed in the case of the NACA 0012 airfoil at high angles of attack (see Figures 4.4 and 4.5). Table 5.3 indicates that the corresponding standard deviations are also overestimated.

As explained earlier, smaller eddies will not be obtained after a grid refinement in the case of the RANS simulations and the accuracy of the results cannot be improved significantly by refining the mesh knowing that the mesh that is used here is quite fine.

The Strouhal number determined numerically is a little underestimated compared to the experimental value.

In the following figures, the transient part of the results is not shown as the analysis of a signal with respect to frequency does not include the transient part. The URANS simulation using the Spalart-Allmaras model produces a periodic solution as can be seen in Figure 5.5.

The predicted flow is unsteady: the wake oscillates periodically as reflected by the evolution of the signal $C_L(t)$.

The aerodynamic force coefficients are sinusoidal. A sharp peak[1] is clearly visible in the power spectral density of $C_L(t)$ at the fundamental frequency of the flow f_s, which corresponds to the shedding frequency (see Figure 5.6a). The magnitude of the other harmonics is negligible compared to the magnitude associated with the fundamental frequency. A semilogarithmic plot reveals the harmonics as shown in Figure 5.6b.

[1]The peak associated with the fundamental frequency in the Welch's power spectral density estimate [27] is sometimes not perfectly symmetrical depending on the sampling frequency, so that a correction can be required to evaluate the Strouhal number St more precisely (e.g., the Half Power Point method).

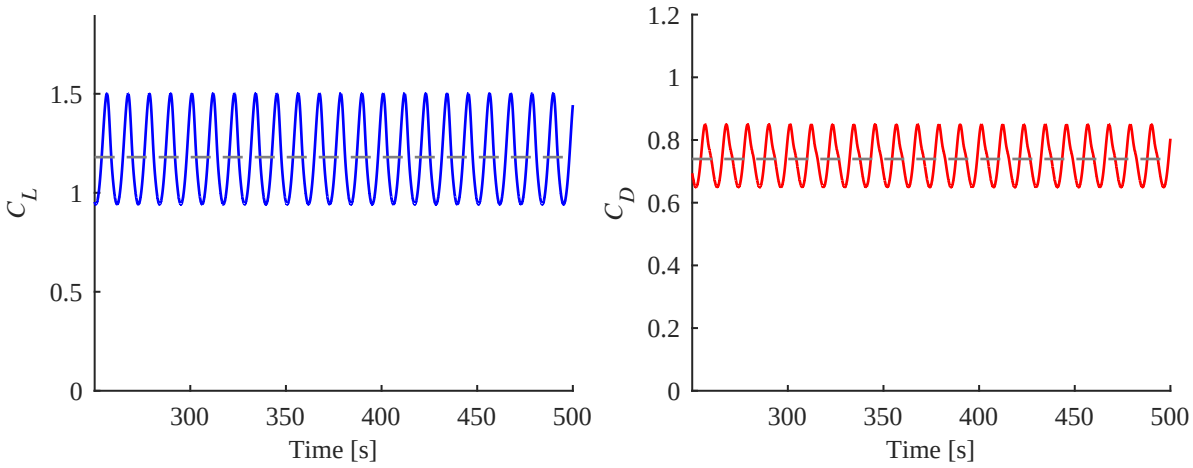

Figure 5.5: Evolution of the aerodynamic force coefficients of the flat plate at $\alpha = 30°$ obtained by 2D URANS: (a) Lift coefficient as a function of time. (b) Drag coefficient as a function of time.

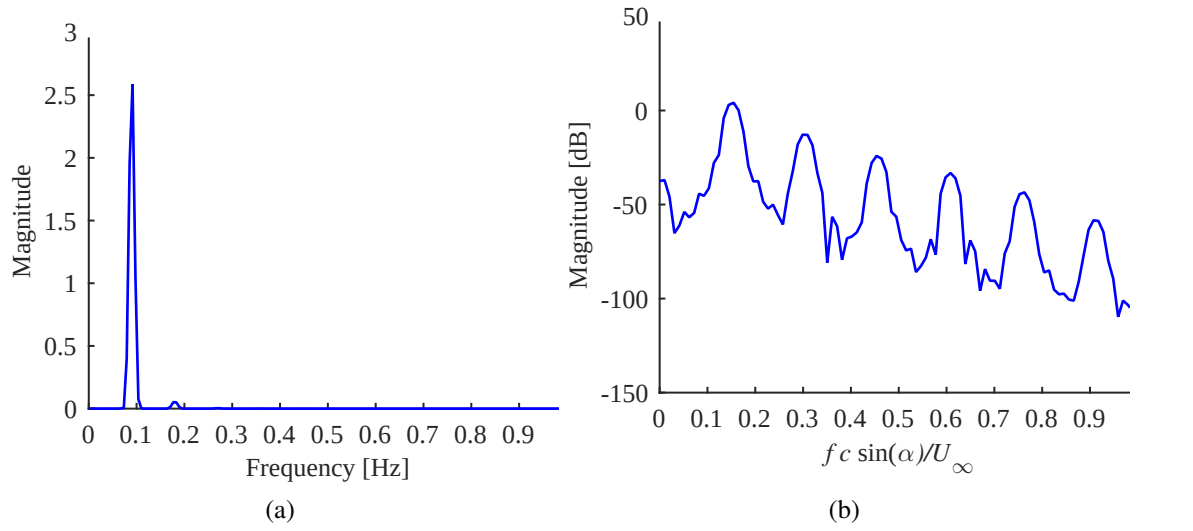

Figure 5.6: Power spectral density of $C_L(t)$ at $\alpha = 30°$ obtained by 2D URANS.

The visualization of the evolution of the flow is quite simple in the case of a two-dimensional unsteady RANS simulation. Figure 5.7 shows four snapshots of the flow which are taken at different phases of one period T_s (in the figure, the period starts at a maximum of C_L which is easier to locate).

The following observations can be inferred:

- The point at $t = 0$ (or $t = T_s$) corresponds to a maximum of the lift coefficient. A large recirculation region above the upper surface of the flat plate is visible. The rotation is clockwise (↻) and the freestream flow is from left to right, so that the recirculation region is created from the flow which separates at the leading edge. Moreover, a detached counterclockwise-rotating vortex is present in the wake.

- At $t = T_s/4$, the lift coefficient is decreasing. A vortex begins to develop near the trailing edge, the rotation is counterclockwise (↺).

- The point at $t = T_s/2$ corresponds to a minimum of the lift coefficient. A vortex near the trailing edge is clearly visible in Figure 5.7c. The created trailing-edge vortex is close to the wall of the flat plate at this particular instant of time.

- At $t = 3T_s/4$, the lift coefficient is increasing. The trailing-edge vortex is shed from the wall of the flat plate (near the trailing edge). The detached trailing-edge vortex is transported downstream by the mean flow.

  A recirculation region develops on the upper part of the flat plate from the leading edge.

The vortex-shedding process is not symmetrical. The Strouhal number corresponding to this unsteady process is estimated at 0.152 based on the signal $C_L(t)$ obtained by the URANS simulation.

All these observations are similar to the conclusions given by Breuer and Jovicic [3]. In this paper, the authors study the flow past a flat plate at $\alpha = 18°$ and $\mathrm{Re} = 2 \times 10^4$ using LES. The value of the angle of attack used in the paper, which is smaller than the one used in the present configuration, is high enough to obtain a separated flow (see Figure 5.9).

The pressure contours given in Figure 5.8 show that the vortex close to the trailing edge is strong while the pressure in the large recirculation region is more uniform. Actually, the formation and shedding of the trailing-edge vortex mainly controls the unsteady behavior of the separated flow [3].

It seems a priori that several coherent flow structures are involved in the evolution of the flow over time. The Dynamic Mode Decomposition (DMD) method will separate the contribution of each dynamic mode as it will be explained in Chapter 6.

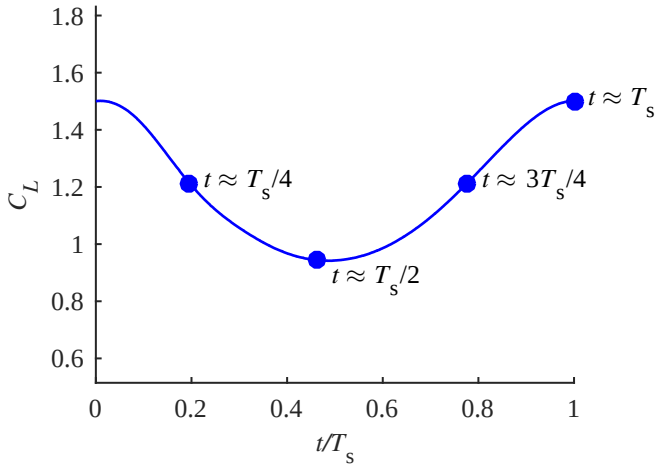

(a) Evolution of the lift coefficient over one period T_s.

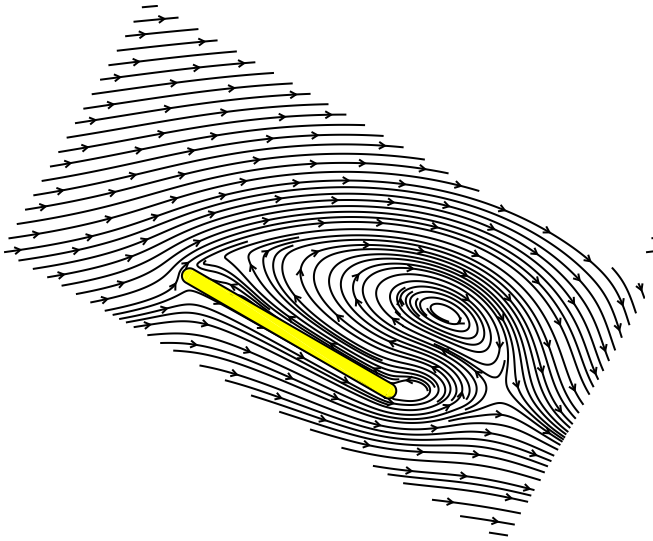

(b) $t \approx T_s/4$.

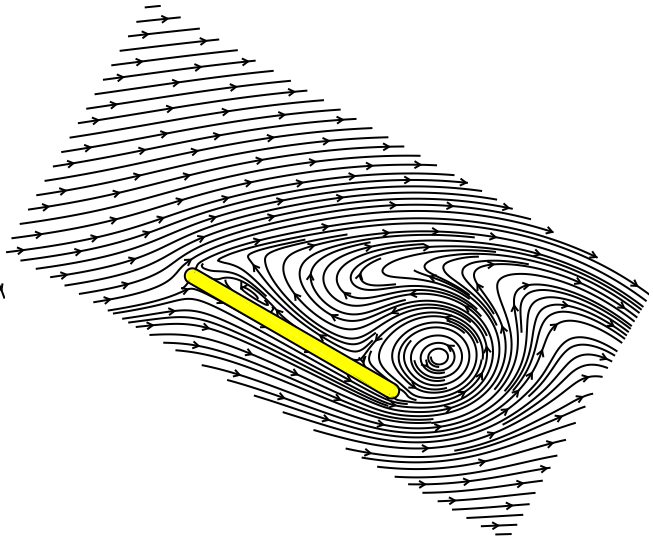

(c) $t \approx T_s/2$.

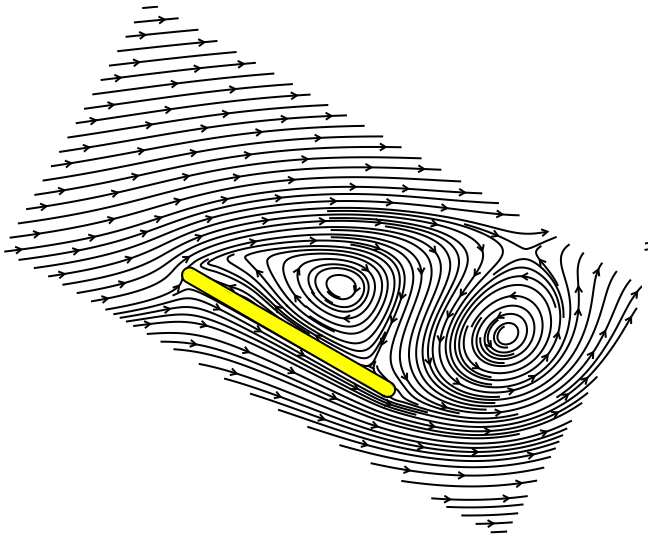

(d) $t \approx 3T_s/4$.

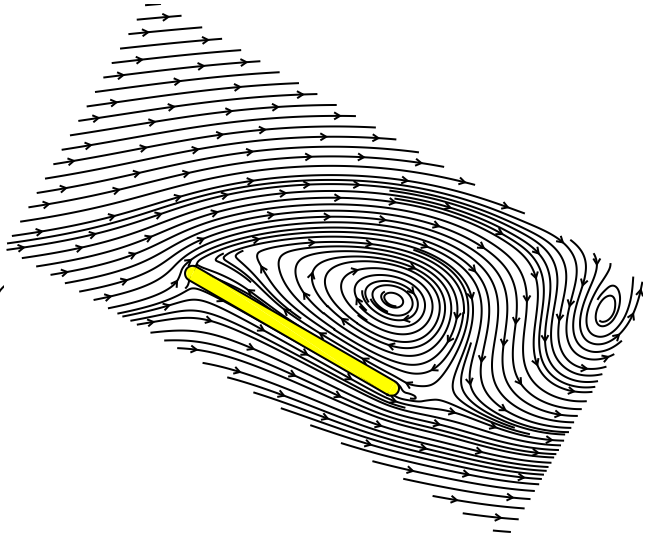

(e) $t \approx T_s$.

Figure 5.7: Streamlines around the flat plate at $\alpha = 30°$ obtained by 2D URANS.

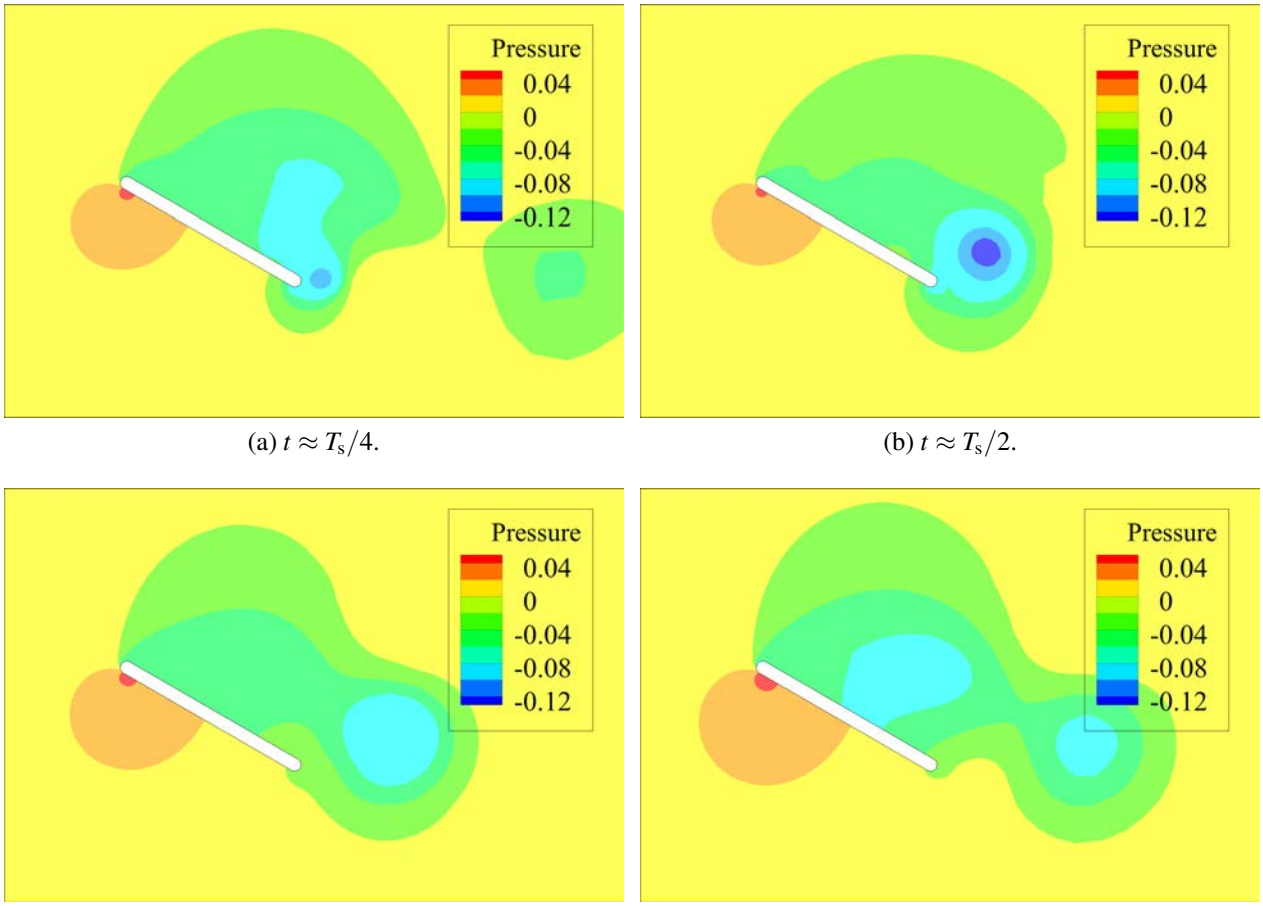

(a) $t \approx T_s/4$.

(b) $t \approx T_s/2$.

(c) $t \approx 3T_s/4$.

(d) $t \approx T_s$.

Figure 5.8: Pressure contours at different phases of a cycle obtained by 2D URANS (static flat plate at $\alpha = 30°$).

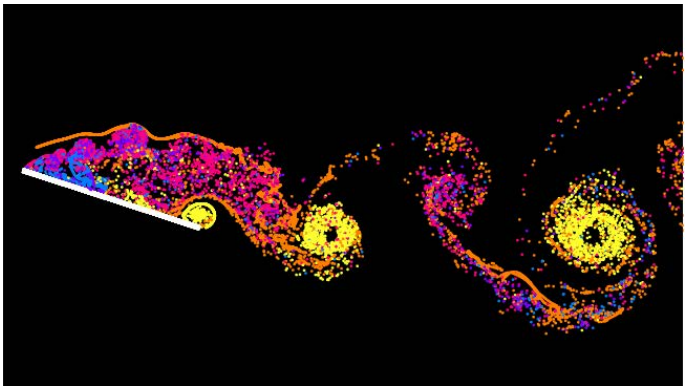

Figure 5.9: Instantaneous streaklines of the flow past an inclined flat plate ($\alpha = 18°$ and $\mathrm{Re} = 2 \times 10^4$), from [3].

A three-dimensional unsteady RANS simulation using the mesh with a spanwise period of $8c$ is performed to see if the 3D effects modify the results.

From Figure 5.10, it can be inferred that three-dimensional effects appear in the wake with a 3D URANS simulation. The snapshot of the flow given in the figure corresponds to an instant when the trailing-edge vortex begins to develop (the shear layer rolls-up). The turbulent eddies are not captured by the 3D URANS simulation; the vortices that are shed downstream are large and smooth.

The imposed spanwise periodicity condition is also observable from Figure 5.10.

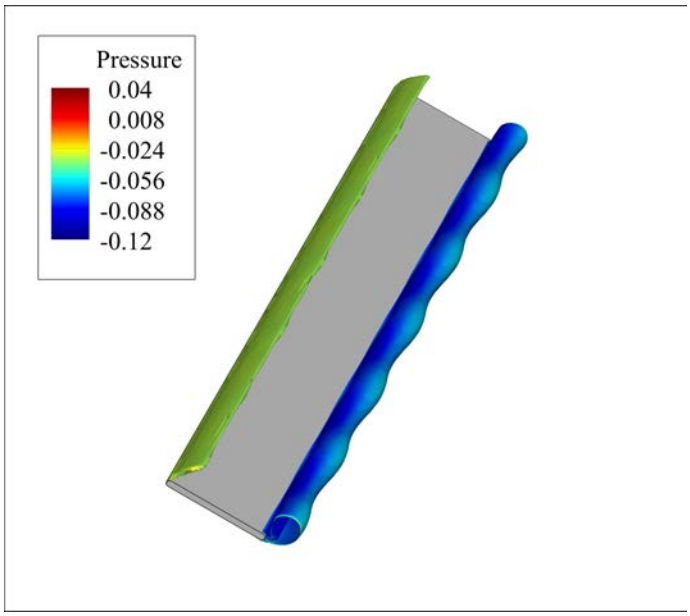

Figure 5.10: Surface of $Q = 0.5$ colored with the kinematic pressure [m^2/s^2] at $\alpha = 30°$ (3D URANS, span = $8c$).

The evolution of the dimensionless force coefficients remains periodic as illustrated in Figure 5.11.

If the flow fields of a DDES calculation are used as an initial condition to start the 3D URANS simulation using the S-A model, the solution converges to the same stable limit cycle than in Figure 5.11 after a few vortex-shedding periods as shown in Figure 5.12.

The statistics of the aerodynamic force coefficients and the Strouhal number are of the same order of magnitude than those obtained by a 2D URANS simulation (see Table 5.3). In conclusion, no significant improvement is achieved by performing a three-dimensional URANS simulation with the S-A turbulence model. In Chapter 6, only the results given by the 2D URANS simulation are considered.

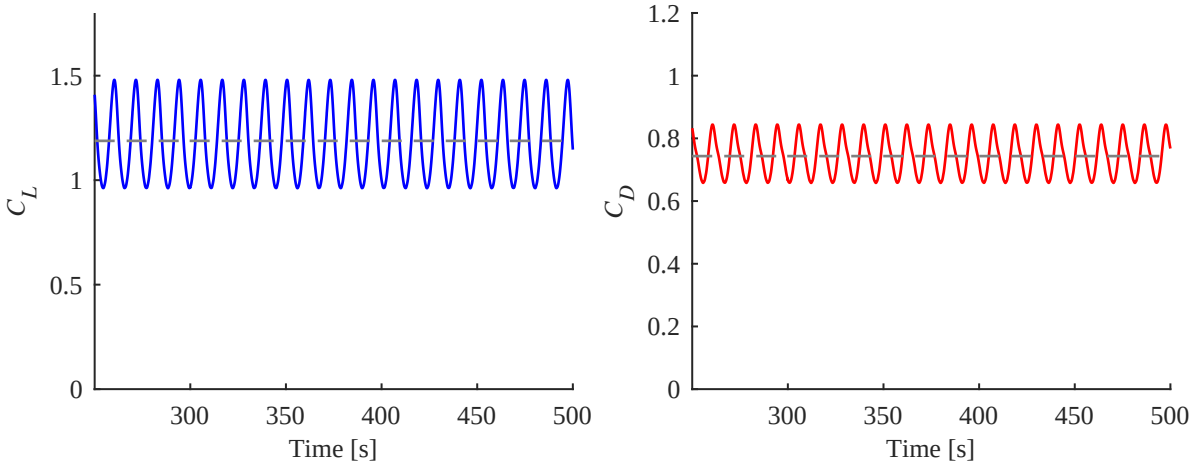

Figure 5.11: Evolution of the aerodynamic force coefficients of the flat plate at $\alpha = 30°$ obtained by 3D URANS (span = $8c$).

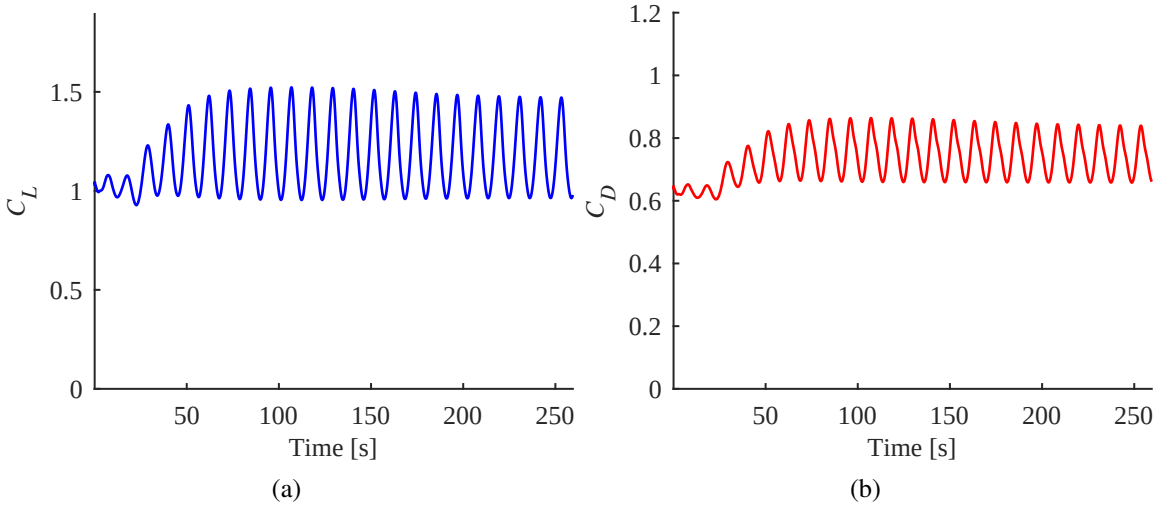

Figure 5.12: Evolution of the aerodynamic force coefficients of the flat plate at $\alpha = 30°$ obtained by 3D URANS (span = $8c$). The DDES solution is used as an initial condition to start the URANS computation.

DDES results

The Strouhal number of each DDES case given in Table 5.3 is only an estimate (mean value). A precise value cannot be determined because the dominant period ($\approx 1/f_s$) is not exactly constant over time.

In Figure 5.13, the time t is non-dimensionalized using the freestream velocity U_∞ and the chord length c in order to facilitate comparison with other numerical or experimental data of the same case using a different chord length or different fluid properties.

The standard deviations S_{C_L} and S_{C_D} are the smallest for the case where the spanwise period is equal to $8c$ indicating that the dispersion of the data values is the smallest. So, the amplitudes of the fluctuations of the dimensionless force coefficients decrease when the span length is increased, which is consistent with the observations seen in Chapter 4. This decrease is even more visible by looking at the signals for a span of c and those for a span of $8c$ (see Figure 5.13). Also, the mean of the coefficients decreases slightly.

Considering the DDES results with a span equal to $8c$, the relative errors with respect to the statistics obtained experimentally (static case, $\mathrm{Re} = 2 \times 10^4$) are given by

$$\varepsilon_{\mathrm{rel},\overline{C_L}} = \left| \frac{\overline{C_{L_{\mathrm{exp}}}} - \overline{C_{L_{\mathrm{DDES}}}}}{\overline{C_{L_{\mathrm{exp}}}}} \right| = \left| \frac{1.05 - 1.0455}{1.05} \right| = 0.43\% \tag{5.2}$$

$$\varepsilon_{\mathrm{rel},\overline{C_D}} = \left| \frac{\overline{C_{D_{\mathrm{exp}}}} - \overline{C_{D_{\mathrm{DDES}}}}}{\overline{C_{D_{\mathrm{exp}}}}} \right| = \left| \frac{0.62 - 0.6395}{0.62} \right| = 3.15\% \tag{5.3}$$

$$\varepsilon_{\mathrm{rel,St}} = \left| \frac{\mathrm{St_{exp}} - \mathrm{St_{DDES}}}{\mathrm{St_{exp}}} \right| = \left| \frac{0.158 - 0.151}{0.158} \right| = 4.43\% \tag{5.4}$$

The time-averaged dimensionless forces are consistent with those measured experimentally.

The standard deviation S_{C_D} is a bit lower than the experimental value (see Table 5.3). The span is slightly longer in the numerical model ($8c$) than in the experiments ($\approx 7.7c$). Moreover, a periodicity condition is imposed in the spanwise direction for the simulations. These factors may partly explain the differences.

A dominant frequency is revealed by the power spectral density of the lift coefficient (see Figure 5.14a). The dominant frequency corresponds to a Strouhal number of about 0.151 and it is associated with the evolution of the coherent structures present in the separated flow as it will be shown in Chapter 6. The dominant frequency found by DDES is slightly lower than the forcing frequency used in the experiment. Moreover, the frequency spectrum has a low frequency content.

In the semilogarithmic plot given in Figure 5.14b, the harmonics of the dominant frequency are not identifiable because with the DDES approach, the large scales are captured and the predicted flow contains disordered turbulent eddies. By contrast, a URANS

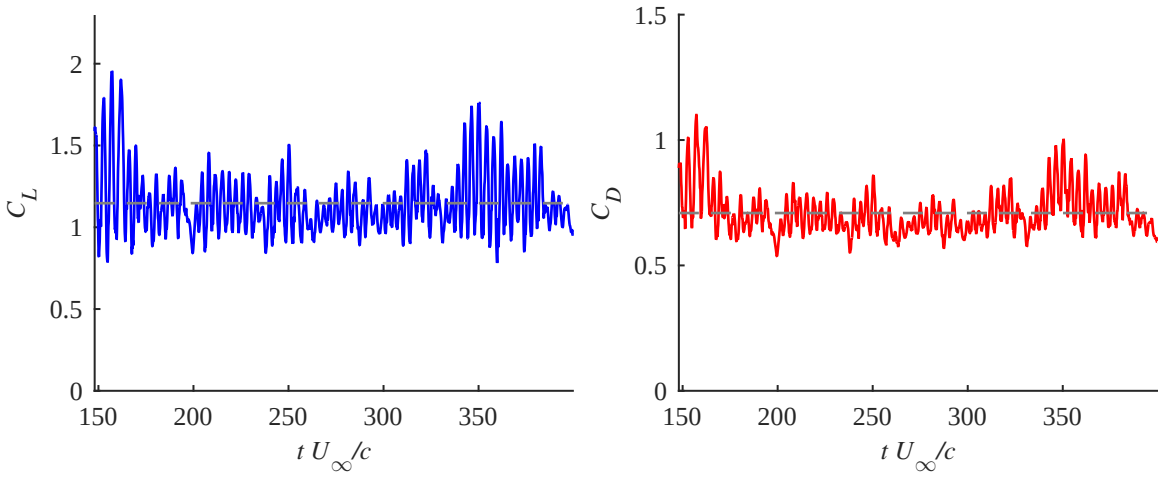

(a) DDES, spanwise period = c.

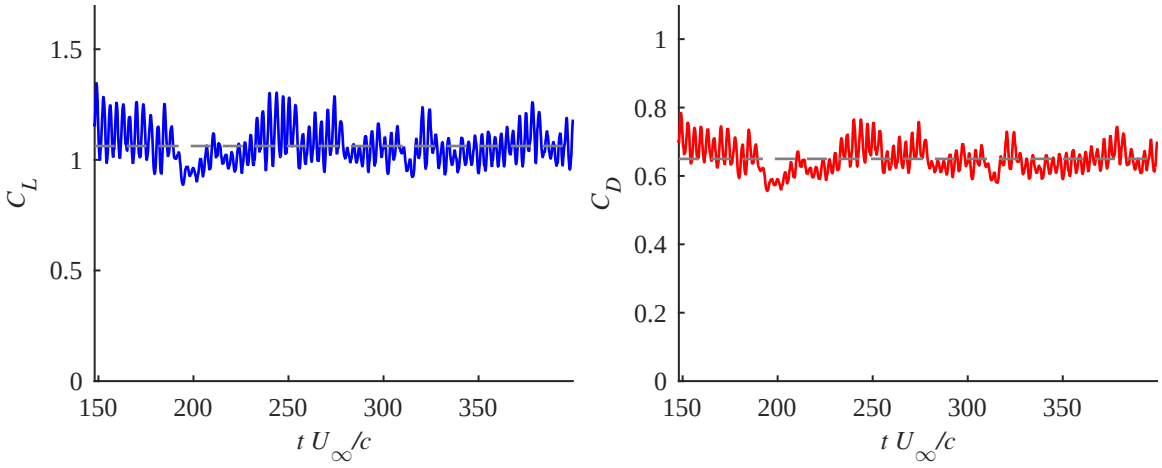

(b) DDES, spanwise period = $4c$.

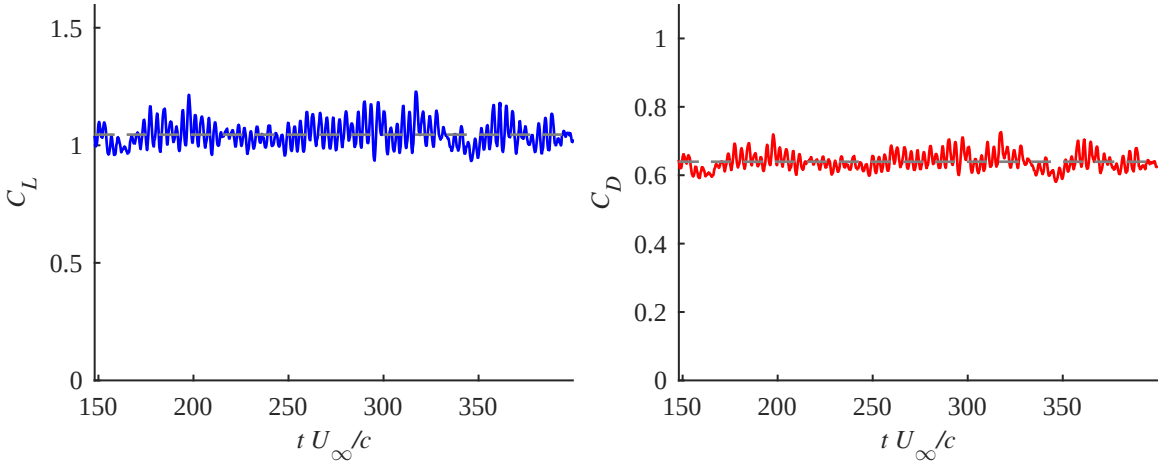

(c) DDES, spanwise period = $8c$.

Figure 5.13: Evolution of the aerodynamic force coefficients of the flat plate at $\alpha = 30°$ for different spanwise periods obtained by DDES: (left) Lift coefficient as a function of the non-dimensionalized time. (right) Drag coefficient as a function of the non-dimensionalized time.

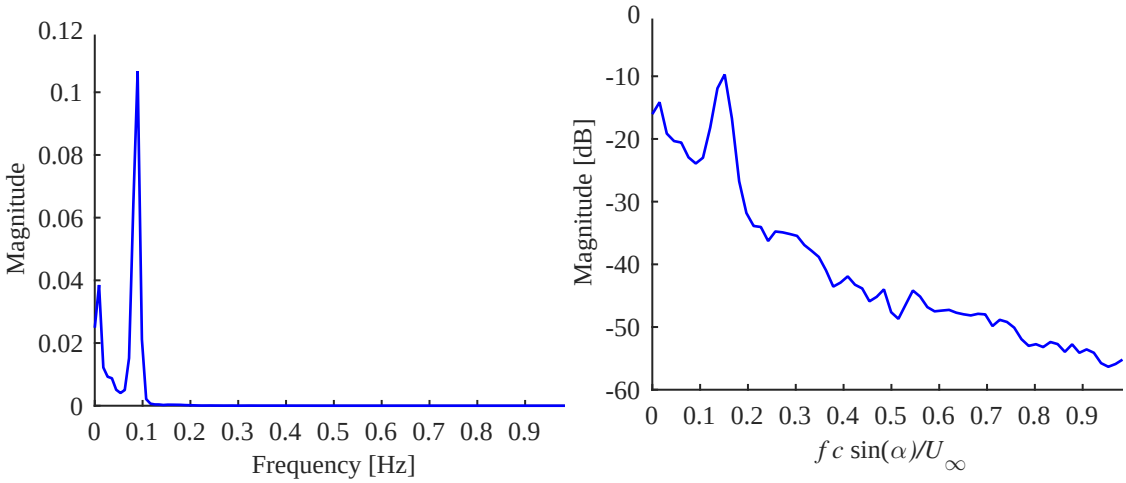

Figure 5.14: Power spectral density of $C_L(t)$ at $\alpha = 30°$ obtained by DDES (span = $8c$).

simulation gives a periodic solution and the harmonics of the fundamental frequency are observable.

In Figure 5.15, small eddies near the wall are visualized by choosing a high value of Q which depends on the flow problem.

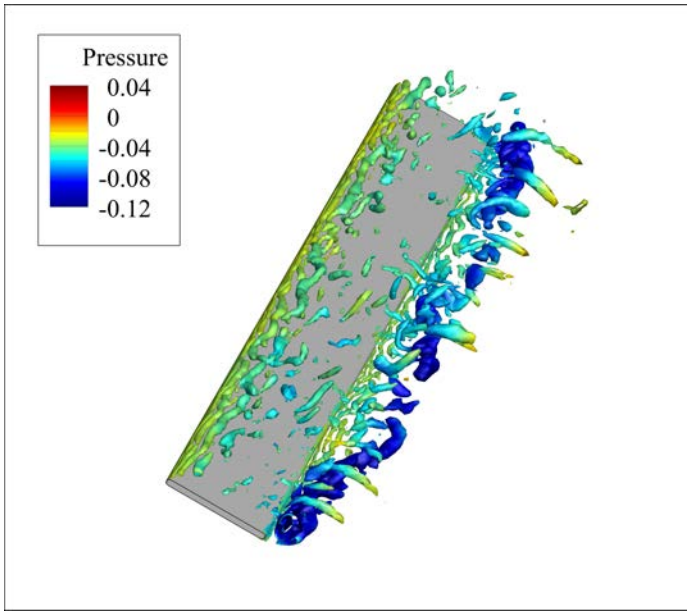

Figure 5.15: Surface of $Q = 4$ colored with the kinematic pressure [m^2/s^2] at $\alpha = 30°$ (DDES, span = $8c$).

The vortex shedding is essentially a three-dimensional phenomenon. The flow components in the spanwise direction have to be taken into account to predict the aerody-

namic forces acting on the flat plate accurately. It is difficult to understand the relation between the aerodynamic force coefficients and the flow structures by looking directly at the evolution of the turbulent flow over time in the case of a flow predicted by DDES (see Figure 5.15); that's why the dynamic mode decomposition method will be used in Chapter 6.

In short, the unsteady RANS simulations using the Spalart-Allmaras model, even three-dimensional, are not able to achieve the accuracy of DDES.

The flow past a flat plate at an angle of attack of 30° contains separation and large scale unsteadiness. From a qualitative point of view, the URANS simulations are able to capture the unsteady nature of the flow.

As already observed in Chapter 4, the general tendency is that the amplitudes of the fluctuations of the aerodynamic force coefficients predicted by DDES are reduced if the span is increased and the mean values are slightly smaller.

The DDES case where the span length is equal to $8c$ produces results that are consistent with the experimental force data.

Chapter 6

Dynamic mode decomposition of CFD results

In this chapter, the Dynamic Mode Decomposition (DMD) method is used in order to obtain information about the coherent structures of a flow problem. The formulation of the decomposition method is summarized at the beginning of the present chapter.

The DMD analysis of the flow fields given by the numerical simulations of Chapter 5 is presented to compare the dynamic modes obtained from each approach.

This chapter also shows the dynamic modes extracted from the experimental measurements for comparison.

A quantitative comparison of the modes extracted from the different numerical results evaluated by the Modal Assurance Criterion (MAC) concludes this chapter.

6.1 Dynamic mode decomposition

The Dynamic Mode Decomposition (DMD) method is detailed in [18, 9].

A sequence of N flow fields or snapshots is represented by a matrix $\mathbf{V}_1^N$:

$$\mathbf{V}_1^N = \{\mathbf{v}_1, \mathbf{v}_2, \mathbf{v}_3, \ldots, \mathbf{v}_N\} \tag{6.1}$$

where $\mathbf{v}_i$ is a vector representing the ith flow field. It is assumed that two consecutive snapshots $\mathbf{v}_i$ and $\mathbf{v}_{i+1}$ are separated by a constant time step Δt. Moreover, a constant linear mapping $\mathbf{A}$ is assumed between two consecutive snapshots:

$$\mathbf{v}_{i+1} = \mathbf{A}\mathbf{v}_i \tag{6.2}$$

The sequence of snapshots can thus be formulated as a Krylov sequence:

$$\mathbf{V}_1^N = \{\mathbf{v}_1, \mathbf{A}\mathbf{v}_1, \mathbf{A}^2\mathbf{v}_1, \ldots, \mathbf{A}^{N-1}\mathbf{v}_1\} \tag{6.3}$$

The purpose of the present decomposition technique is to extract the dynamic characteristics of the physical system described by the matrix $\mathbf{A}$ which is usually not known a priori.

If the sequence of snapshots $\mathbf{V}_1^N$ includes a sufficiently large number of snapshots, the dominant features of the physical system are captured by $\mathbf{V}_1^N$. Therefore, it may be assumed that the snapshots are linearly dependent beyond a certain number. The last snapshot $\mathbf{v}_N$ is then written as a linear combination of the previous snapshots $\{\mathbf{v}_1, \mathbf{v}_2, \mathbf{v}_3, \ldots, \mathbf{v}_{N-1}\}$:

$$\mathbf{v}_N = \mathbf{V}_1^{N-1}\mathbf{a} + \mathbf{r} \tag{6.4}$$

where $\mathbf{a} = (a_1 \quad a_2 \quad \ldots \quad a_{N-1})^T$ and $\mathbf{r}$ is the residual vector. According to [17], the following matrix relation can then be written:

$$\mathbf{A}\mathbf{V}_1^{N-1} = \mathbf{V}_2^N = \mathbf{V}_1^{N-1}\mathbf{S} + \mathbf{r}\mathbf{e}_{N-1}^T \tag{6.5}$$

where $\mathbf{S}$ is a companion matrix given by

$$\mathbf{S} = \begin{pmatrix} 0 & & & & a_1 \\ 1 & 0 & & & a_2 \\ & \ddots & \ddots & & \vdots \\ & & 1 & 0 & a_{N-2} \\ & & & 1 & a_{N-1} \end{pmatrix} \tag{6.6}$$

and $\mathbf{e}_{N-1}^T$ is the $(N-1)$th unit vector: $\mathbf{e}_{N-1}^T = (0 \quad 0 \quad \ldots \quad 1)$.

By construction, some of the eigenvalues of the matrix $\mathbf{A}$ are approximated by those of the companion matrix $\mathbf{S}$. The last column of $\mathbf{S}$, which contains the components of $\mathbf{a}$, is unknown. The vector $\mathbf{a}$ can be obtained by calculating the least-squares solution of (6.4) through a QR decomposition of the sample sequence $\mathbf{V}_1^{N-1}$. However, in practice, the decomposition algorithm using the companion matrix $\mathbf{S}$ is ill-conditioned and the first two dominant dynamic modes of the physical process can be extracted at most.

A more robust computation is obtained using a full matrix $\tilde{\mathbf{S}}$. First, a singular value decomposition of $\mathbf{V}_1^{N-1}$ is evaluated:

$$\mathbf{V}_1^{N-1} = \mathbf{U}\Sigma\mathbf{W}^* \tag{6.7}$$

where $\mathbf{U}$ and $\mathbf{W}^*$ (the conjugate transpose of $\mathbf{W}$) are unitary matrices and Σ is a rectan-

gular diagonal matrix containing the singular values of $\mathbf{V}_1^{N-1}$. Then, the singular value decomposition is substituted in (6.5) to get

$$\mathbf{U}^* \mathbf{A} \mathbf{U} = \mathbf{U}^* \mathbf{V}_2^N \mathbf{W} \Sigma^{-1} = \tilde{\mathbf{S}} \tag{6.8}$$

The dynamic modes are then given by

$$\Phi_i = \mathbf{U} \mathbf{y}_i \tag{6.9}$$

where $\mathbf{y}_i$ is the ith eigenvector of $\tilde{\mathbf{S}}$:

$$\tilde{\mathbf{S}} \mathbf{y}_i = \mu_i \mathbf{y}_i \tag{6.10}$$

and the associated frequencies correspond to the imaginary part of

$$\lambda_i = \frac{\log(\mu_i)}{\Delta t} \tag{6.11}$$

Choice of the time step

The constant time step between two consecutive snapshots must be small enough in order that relevant dynamic processes can be extracted from the data sequence.

According to the Nyquist criterion, the sampling frequency must be at least two times the characteristic frequency of a process in order to identify this process.

Schmid, the author of the DMD method, recommends to choose a sampling frequency equal to about three times the Nyquist limit for the dynamic mode decomposition [18].

6.2 Applications

In this part, the inclined flat plate configuration of Chapter 5 is considered. The DMD method is applied to two sets of numerical data: the flow fields given by the two-dimensional URANS simulation and the ones given by the DDES approach where the span length is equal to $8c$.

The formulation of DMD is only based on the sequence of data $\mathbf{V}_1^N$ and therefore composite data can also be processed.

The velocity components in the xy-plane combined with the global aerodynamic force coefficients are used to perform the dynamic mode decomposition to link the flow structures with the variations of $C_L(t)$ and $C_D(t)$. The numerical flow field data are available at the grid points given in Figure 6.1. This size of the subdomain is large enough to include the vortex-shedding process as shown earlier (see Figure 5.7).

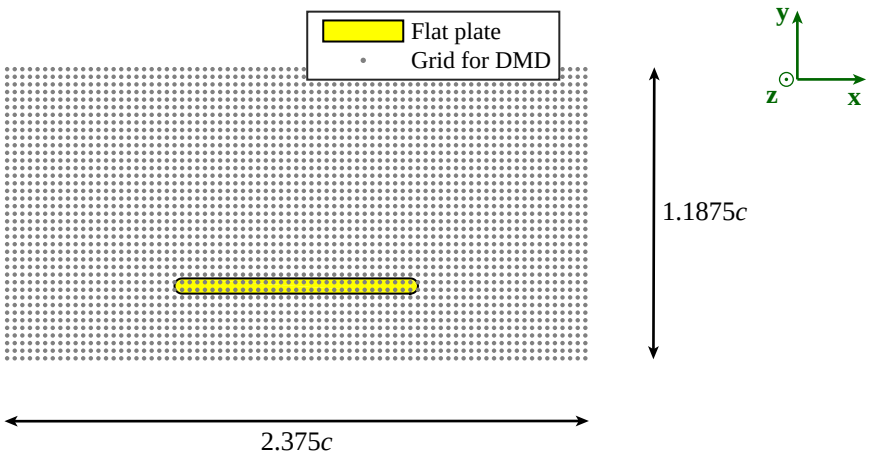

Figure 6.1: Grid resolution used for the DMD analysis: $\Delta x/c = 0.03125$ and $\Delta y/c = 0.03125$. The reference frame is also shown.

The size and resolution of the window are also chosen knowing that a long time interval has to be considered to have converged solutions and to take account of the low frequency content in the case of the DDES results. Moreover, about 20 snapshots are considered per shedding period. So, the memory requirements will be significant and the computational cost of DMD increases if the size of the matrix $\mathbf{V}_1^N$ increases. In addition, the regions where the mesh is coarse introduce numerical dissipation.

6.2.1 DMD of the flow fields obtained by 2D URANS

The URANS simulation gives a periodic solution for the inclined flat plate case. Therefore, the time step depends on the vortical flow structures that are shed by the body: the sampling frequency is chosen equal to about 20 times the fundamental frequency. The tenth harmonic (10 times the fundamental frequency) can thus be identified according to the Nyquist criterion and the third harmonic can be determined satisfactory by the dynamic mode decomposition according to Schmid's suggestion [18].

DMD provides the dynamic modes and their corresponding frequency and amplitude. Figure 6.2 shows the DMD amplitude distribution as a function of frequency ($= \Im(\lambda_i)$, see Equation (6.11)) in a semilogarithmic plot.

The modes are sorted by descending amplitude. The first three dominant dynamic modes are illustrated by a velocity plot. The mean flow mode ($f = 0$ Hz) is included in the graphics.

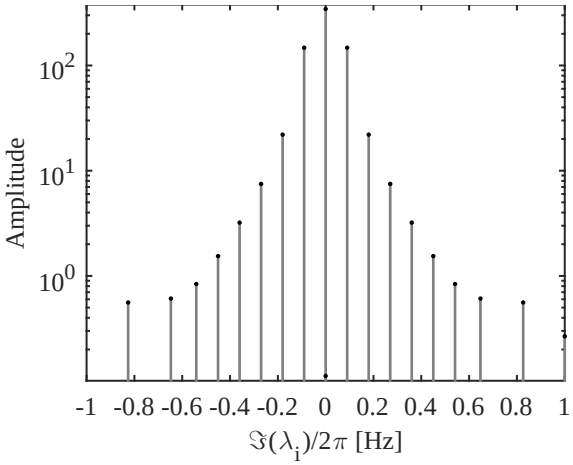

Mode	Dimensionless frequency	$A/A_{\max}$
1	0	1
2	0.152	0.1424
3	0.304	0.0298
4	0.456	0.0119
5	0.608	0.0056

(a) DMD amplitude distribution.

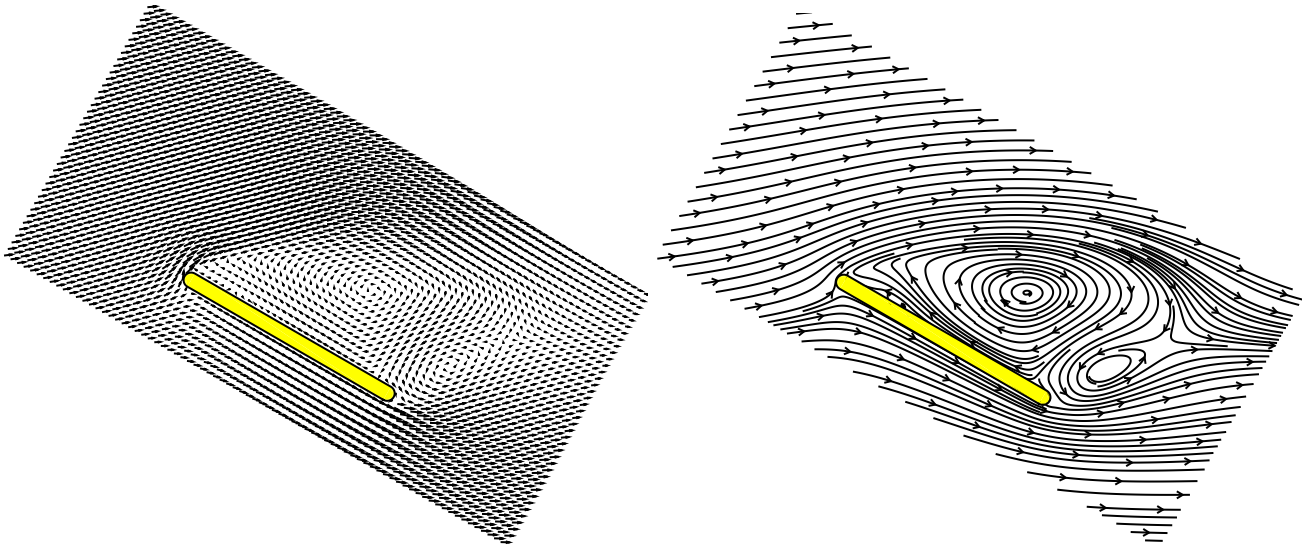

(b) Mode 1 ($f = 0$ Hz, $A/A_{\max} = 1$).

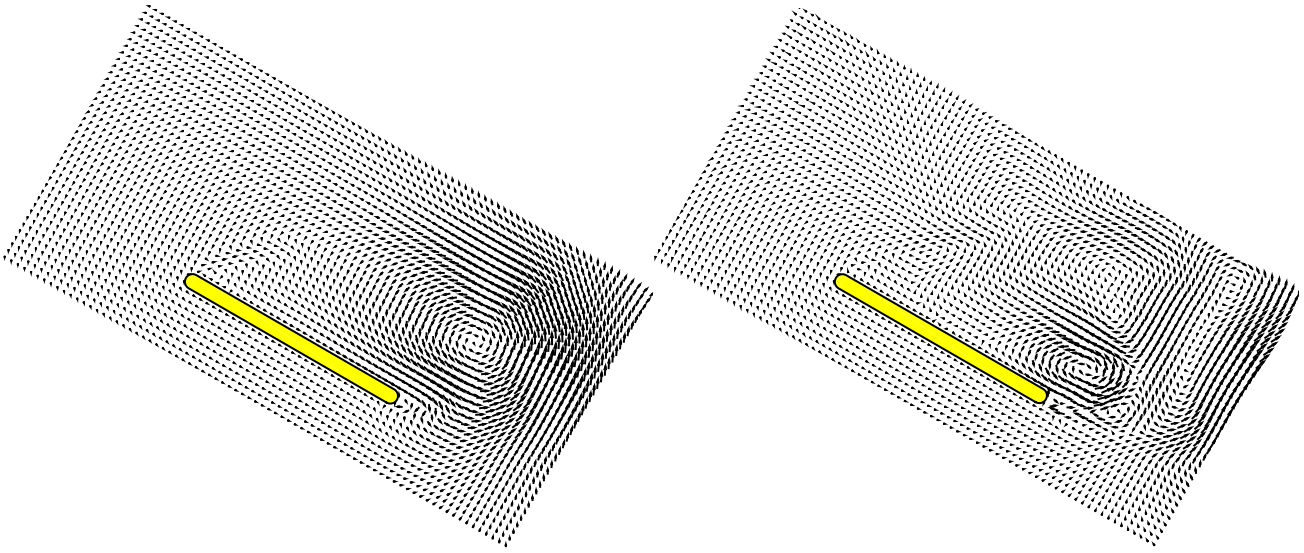

(c) Mode 2 ($f = 0.0900$ Hz, $A/A_{\max} = 0.1424$).

(d) Mode 3 ($f = 0.1800$ Hz, $A/A_{\max} = 0.0298$).

Figure 6.2: DMD analysis of the 2D URANS flow fields.

The mean flow mode appears once. The DMD amplitude distribution as a function of frequency is symmetrical with respect to $\Im(\lambda_i) = 0$ because the input data are real [18].

A peak is clearly visible at the fundamental frequency f_s in the frequency spectrum given in Figure 6.2a. The other harmonics (i.e., integer multiples of f_s) are also present but their amplitude is smaller than the amplitude associated with f_s.

The table in Figure 6.2a shows that the normalized amplitude of the modes beyond the third one is very low indicating that the contribution of the modes at high frequency to the dynamics of the system is weak.

The velocity plots indicate that the vortices can be identified with the components of the velocity vector in the *xy*-plane that have been used to construct the snapshot sequence for the decomposition. The following remarks can be deduced:

- The first mode is the constant mode ($f = 0$ Hz) and it corresponds to the contribution of the mean flow.

  In the first mode, the incoming streamlines upstream of the separation point at the leading edge detach from the surface of the flat plate (see Figure 6.2b). A large region of recirculating flow develops in the wake downstream of the separation point.

  A smaller vortex forms near the trailing edge.

- The velocity plot of the second dynamic mode depicted in Figure 6.2c shows a vortex close to the trailing edge.

  The frequency associated with the second mode corresponds to a Strouhal number St ($= fc\sin(\alpha)/U_\infty$) equal to 0.152.

  The Strouhal number has already been estimated at about 0.152 from the evolution of the lift coefficient as a function of time (see Table 5.3 and Figure 5.6 of Chapter 5).

  The unsteady behavior of the separated flow around the static flat plate at $\alpha = 30°$ and $\mathrm{Re} = 2 \times 10^4$ is mainly controlled by the formation and shedding of the trailing-edge vortex. The vortex shedding is not symmetrical.

- The mode at the second harmonic also shows a vortex near the trailing edge but the flow pattern is less coherent compared to Mode 2. The amplitude associated with the third mode is lower than the one of the second mode.

- The other spatial modes are not presented since they are not pertinent.

Reconstruction of the flow fields using the most dominant dynamic modes

The snapshot sequence can be reconstructed using the dynamic modes. For example, for the velocity field at an instant t, one has [9]

$$\mathbf{u}(x,y,t) = \sum_{k=1}^{N} \underbrace{a_k^{\mathrm{DMD}}}_{\text{Amplitude}} \underbrace{\exp(\lambda_k^{\mathrm{DMD}} t)}_{\text{Time evolution}} \underbrace{\Phi_k^{\mathrm{DMD}}(x,y)}_{\text{Spatial mode}} \tag{6.12}$$

If all modes are included in the summation of Equation (6.12), then the original flow field is recovered.

Table 6.1 indicates the errors associated with the statistics of the dimensionless force coefficients when the most dominant modes are considered. If only the mean flow mode is retained, then the vibration amplitude of the reconstructed lift and drag signals is zero and the associated standard deviations are null (the relative errors are equal to one in the first row of Table 6.1).

The modes that are relevant are essentially the first three modes. For instance, if the first three dynamic modes are considered, the reconstructed samples coincide very well with the original samples used for the decomposition as illustrated in Figure 6.3.

Number of retained modes	$\left\lvert \frac{\overline{C_{L_{\mathrm{URANS}}}} - \overline{C_{L_{\mathrm{approx}}}}}{\overline{C_{L_{\mathrm{URANS}}}}} \right\rvert$	$\left\lvert \frac{S_{C_{L_{\mathrm{URANS}}}} - S_{C_{L_{\mathrm{approx}}}}}{S_{C_{L_{\mathrm{URANS}}}}} \right\rvert$	$\left\lvert \frac{\overline{C_{D_{\mathrm{URANS}}}} - \overline{C_{D_{\mathrm{approx}}}}}{\overline{C_{D_{\mathrm{URANS}}}}} \right\rvert$	$\left\lvert \frac{S_{C_{D_{\mathrm{URANS}}}} - S_{C_{D_{\mathrm{approx}}}}}{S_{C_{D_{\mathrm{URANS}}}}} \right\rvert$
1	0.0801	100	0.0158	100
2	0.0256	1.1110	0.0228	1.5702
3	0.0154	0.1248	0.0140	0.2733
4	0.0139	0.0636	0.0137	0.0806
5	0.0154	0.0447	0.0151	0.0457

Table 6.1: Relative errors associated with the time-averaged aerodynamic force coefficients and the associated standard deviations as functions of the number of retained modes in the reconstruction. The complex conjugate of each selected mode is also included in the reconstruction. Error values are in percent.

The lift and drag signals are not in phase. The phase difference is observable in Figure 6.3: $C_D(t)$ is slightly delayed compared to $C_L(t)$.

In the case of the 2D URANS simulation, the reconstruction of the sequence of velocity fields using the most dominant dynamic modes yields to the same snapshots of the flow presented in Figure 5.7 of Chapter 5. As an example, Figure 6.4 shows one original snapshot and a reconstructed snapshot at the same instant.

The implementation of the reconstruction algorithm is validated because the two streamline plots are not distinguishable.

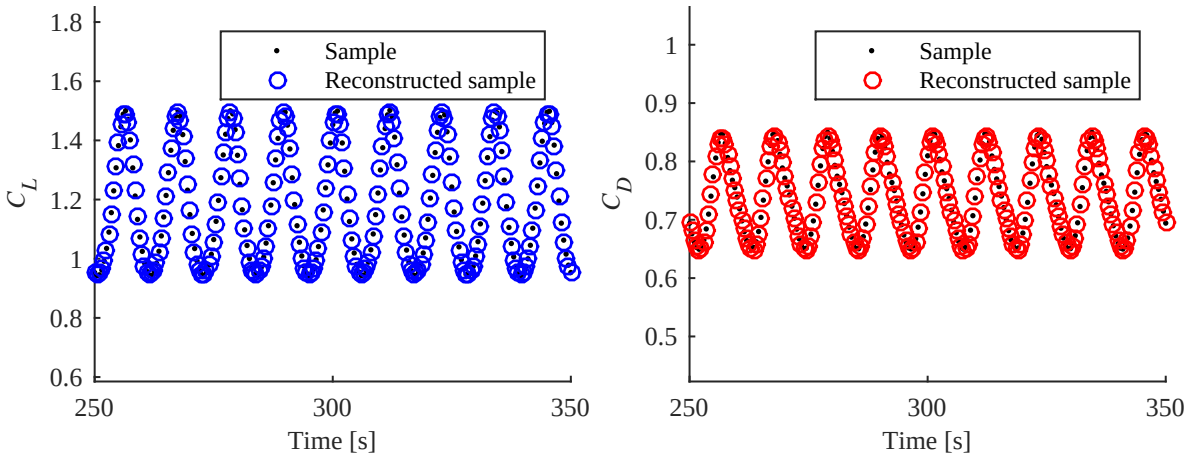

Figure 6.3: Reconstruction of the aerodynamic force coefficients using the first three dominant dynamic modes. The complex conjugate of each selected dynamic mode is also included in the reconstruction.

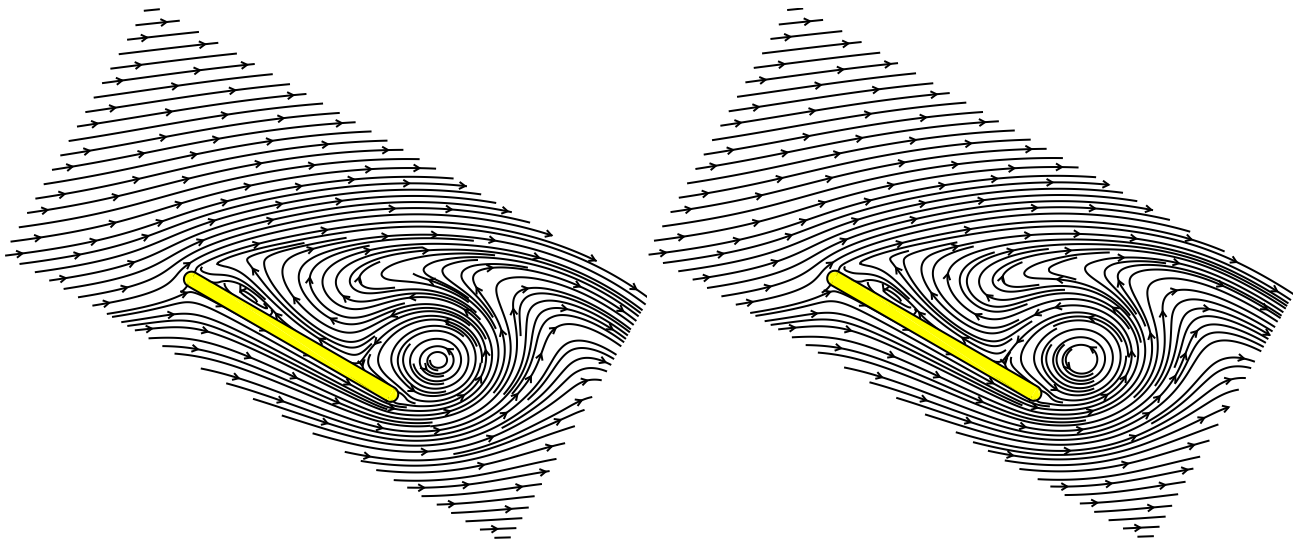

Figure 6.4: Comparison between (a) an instantaneous velocity field obtained by 2D URANS and (b) a velocity field reconstructed using the first three dominant dynamic modes at a given time.

6.2.2 DMD of the flow fields obtained by DDES

2D flow fields

A slice normal to the z-direction is taken; the location of the plane in the span does not matter because of the imposed periodicity condition in the spanwise direction. The amplitude and the frequency of the flow structures extracted from the sequence of velocity fields contained in a cross section are represented in Figure 6.5.

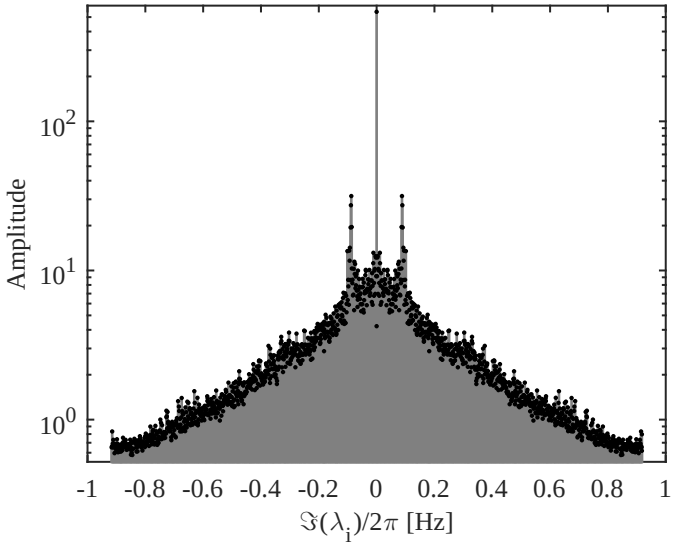

Figure 6.5: DMD amplitude distribution obtained from the sequence of flow fields given by DDES.

Figure 6.5 shows that the level of noise in the results obtained by a decomposition directly applied to the evolution of the two-dimensional flow fields over time is high due to the fact that large-scale turbulent eddies are captured by the DDES technique and so the numerical results are not as smooth as in a URANS simulation.

Nevertheless, the dominant Strouhal number is located near 0.151 (or $f \approx 0.09$ Hz).

A low frequency content exists too but a well-defined peak is not observable in this range.

Phase averaging of the flow fields

In this section, the (quasi-)periodic vortex shedding is analyzed using a phase-averaging technique. A unique 2D slice is chosen like in the case of the PIV measurements.

The Strouhal number St is estimated at about 0.151 (see Table 5.3 and Figure 5.14 of Chapter 5) and the reference shedding period T_s (= $1/f_s$) to be used to calculate a phase average of the flow fields is deduced.

20 phases uniformly distributed on the reference period T_s are chosen. The sampling period is thus $T_s/20$. The time step between the snapshots has to be constant for the dynamic mode decomposition.

The entire simulation time interval is from $t = 500$ s to $t = 1350$ s but the phase-averaged solution is computed on a portion of this interval. The reason is that the vortex-shedding process predicted by the DDES approach is not exactly periodic as the flat plate is static in the numerical model. This behavior is also observed in the static case of the experiments as mentioned earlier.

The phase average of the flow fields is calculated over approximately 50 shedding cycles in a time interval where the shedding period varies the least.

Ideally, the flat plate should vibrate in the simulations like in the forced case of the experiments and a long simulation time should be considered to compute the phase-averaged solution. The experimental measurements are acquired over a much longer time interval.

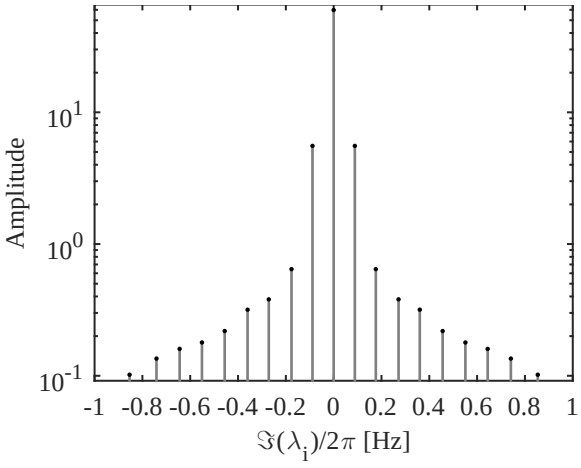

Mode	Dimensionless frequency	$A/A_{\max}$
1	0	1
2	0.150	0.0930
3	0.298	0.0108
4	0.458	0.0064
5	0.608	0.0053

(a) DMD amplitude distribution.

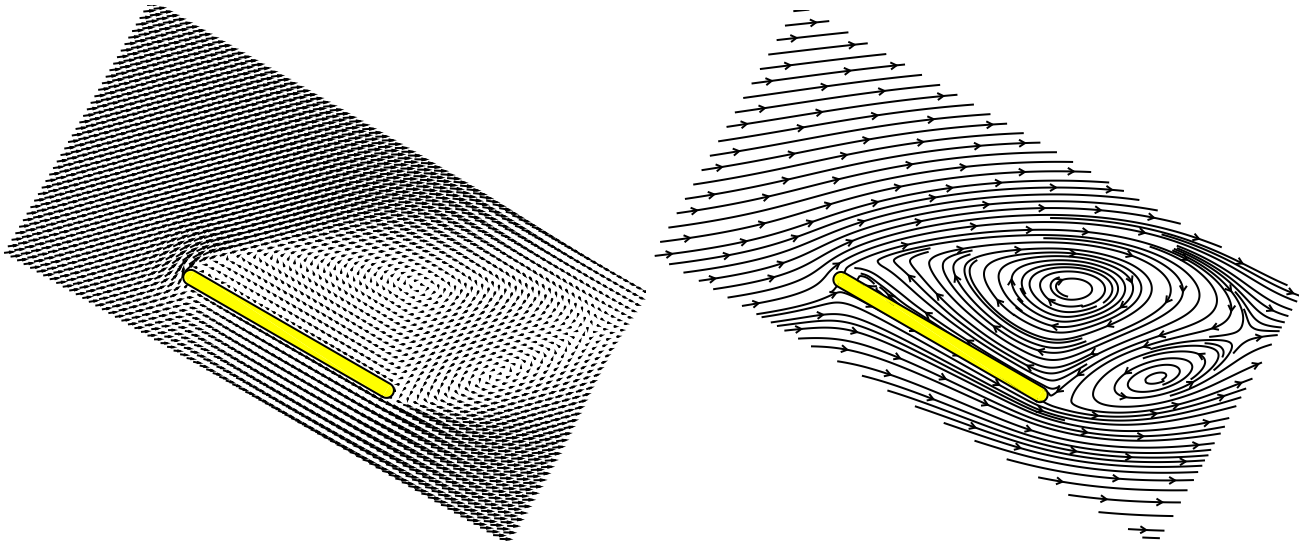

(b) Mode 1 ($f = 0$ Hz, $A/A_{\max} = 1$).

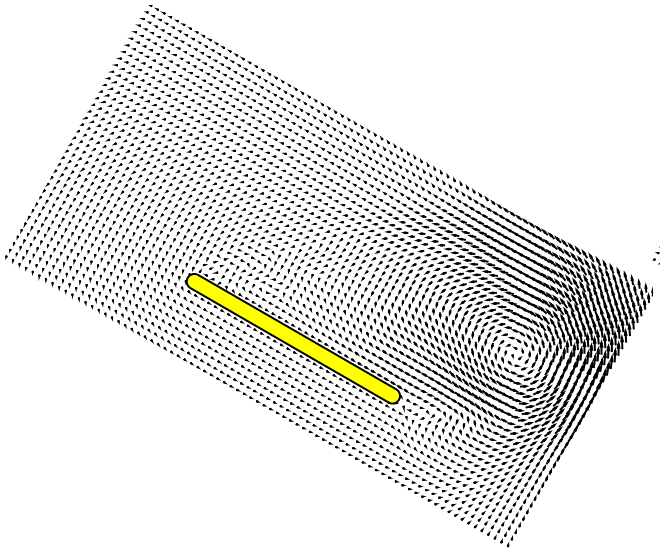

(c) Mode 2 ($f = 0.0886$ Hz, $A/A_{\max} = 0.0930$).

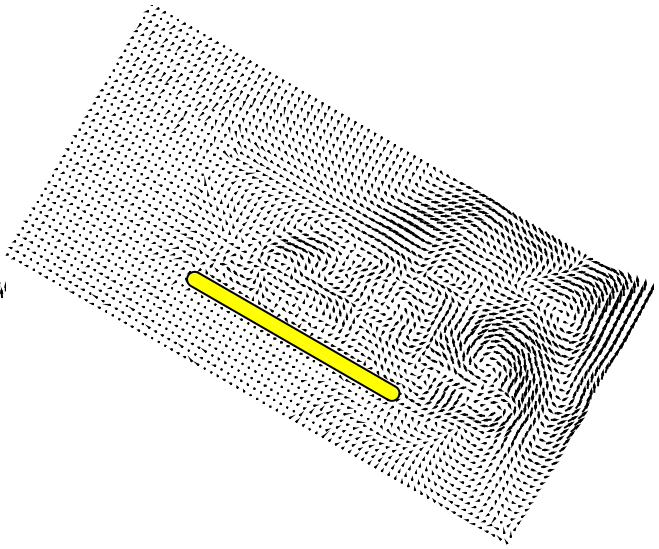

(d) Mode 3 ($f = 0.1763$ Hz, $A/A_{\max} = 0.0108$).

Figure 6.6: DMD analysis of the spanwise-averaged DDES flow fields.

The phase-averaging operation reduces the noise level in the results as the random fluctuations are smoothed. The frequencies lower than the frequency associated with St $\approx$ 0.151 are removed by the phase averaging as reflected by the amplitude distribution given in Figure 6.6a.

The frequency spectrum obtained from the phase-averaged velocity fields of the separated flow shows a peak at 0 Hz (mean flow mode) and the harmonics. The fundamental frequency (or first harmonic) is associated with a Strouhal number of 0.150.

The amplitude of the dynamic modes (without considering the mean flow mode) is slightly smaller compared to the DMD analysis carried out with the 2D URANS simulation. The difference may be due to the fact that the velocity component in the z-direction is not considered for the decomposition. Indeed, DDES is three-dimensional and the vortex shedding is essentially a three-dimensional phenomenon too. In the case of a 2D URANS simulation, the flow components in the z-direction are not computed and the vortex shedding is contained in the xy-plane.

Figure 6.6 shows that the first two dominant spatial modes are consistent with those extracted from the URANS results. Nevertheless, some differences exist: the size of the recirculation regions and the location of the vortex cores are not exactly identical in both approaches. The third mode, which has a lower amplitude, is more irregular in the case of the DDES results.

The spatial modes will be compared quantitatively using the Modal Assurance Criterion (MAC) in Section 6.2.4.

The velocity field of the second mode shows a vortex close to the trailing edge of the flat plate. This vortex is shed periodically.

Comparison with the DMD analysis of the experimental data

Table 6.2 and Figure 6.7 give the results of the dynamic mode decomposition of the velocity fields obtained by Particle Image Velocimetry (PIV) in the case where the flat plate is forced to vibrate.

A rigorous quantitative comparison is not possible for the following reasons. First, as mentioned earlier, the Reynolds numbers are not the same: $\mathrm{Re} = 4 \times 10^4$ in the forced case of the experiments and $\mathrm{Re} = 2 \times 10^4$ in the numerical simulations. Then, the Strouhal number determined numerically and the imposed value in the experiment do not match exactly because the flat plate does not oscillate at the forcing frequency like in the experimental setup.

Table 6.2 shows that the order of magnitude of the dimensionless frequencies and the normalized amplitudes are rather close to those given by the DMD analysis of the phase-averaged DDES velocity fields.

Mode	Dimensionless frequency	$A/A_{\max}$
1	0	1
2	0.156	0.1140
3	0.312	0.0147
4	0.468	0.0058
5	0.624	0.0031

Table 6.2: Dimensionless frequency and amplitude associated with each dynamic mode (experimental velocity fields).

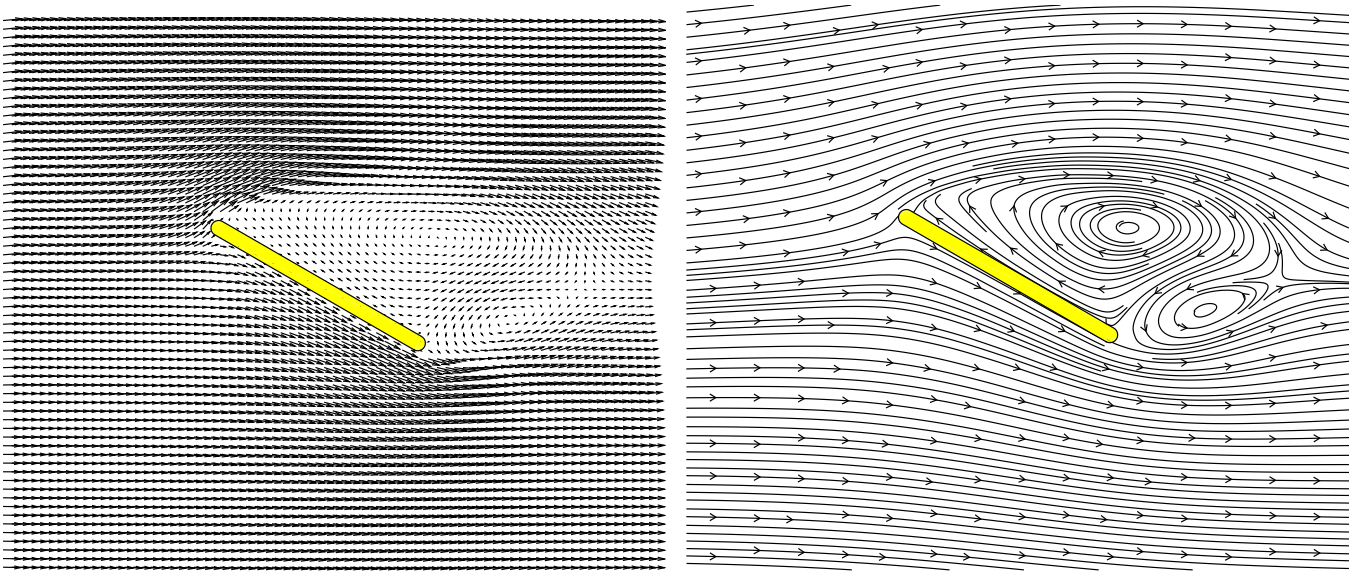

(a) Mode 1.

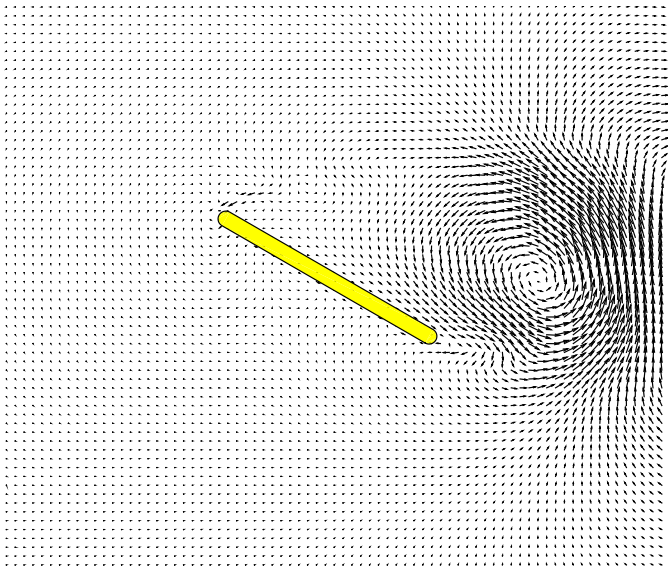

(b) Mode 2.

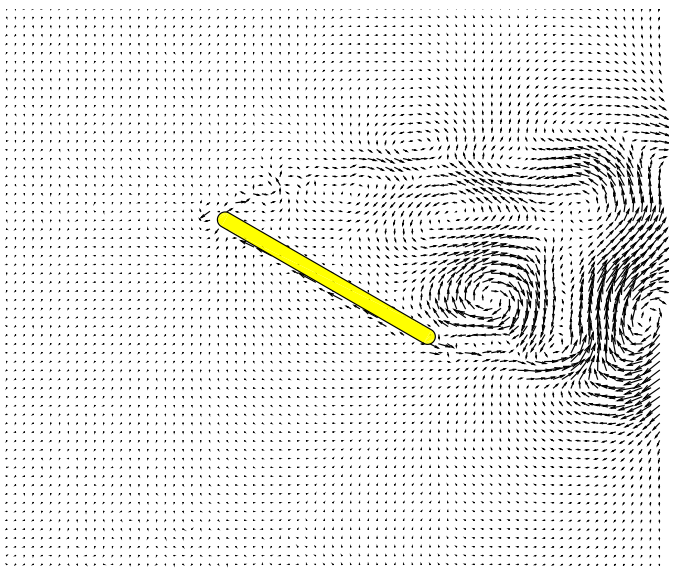

(c) Mode 3.

Figure 6.7: Representation of the modes extracted from the experimental measurements.

From a qualitative point of view, the two first spatial modes extracted from the experimental flow fields are similar to those obtained from numerical results. The third mode, which is of smaller amplitude, is more difficult to compare because the velocity plot is irregular in the wake.

Among the numerical simulations, the dynamic mode decomposition of the phase-averaged DDES velocity fields is the closest to the experimental one demonstrating that the separated flow is predicted more accurately with DDES.

6.2.3 Reconstruction of the DDES flow fields using dominant dynamic modes

In this section, the relation between the flow structures and the aerodynamic force coefficients is studied with the purpose of a better understanding of the physics of the unsteady flow. The quantities C_L and C_D are added to the sequence of data fields.

Phase and spanwise averaging of the flow fields

If a slice is taken for the DMD analysis, the lift and drag coefficients, which are global quantities, do not correspond exactly to the section dimensionless force coefficients which are not easy to determine. Consequently, the DDES results are averaged in the spanwise direction (spatial average).

The first idea was to write the velocity vector at each point of a uniform mesh generated by extruding the 2D grid presented in Figure 6.1 in the z-direction. This approach may be practicable for the mesh where the spanwise period is c using the required sampling period ($\approx T_s/20$) and a sufficiently long simulation time to have converged solutions. However, the memory requirements at each time step are quite high for the meshes with a higher spanwise period ($4c$ and $8c$). Moreover, the interpolation of the mesh values to a uniform grid slows down the computation. In the scope of this work, only 8 slices in the xy-plane and uniformly distributed along the span are kept to compute the spanwise-averaged flow fields.

Figure 6.8 illustrates that the normalized amplitudes are lower than those obtained before averaging the flow fields in the spanwise direction. This attenuation highlights once again the three-dimensional nature of the separated flow.

In Figure 6.9, the flow is described by the first three dominant modes extracted from the snapshots of the flow.

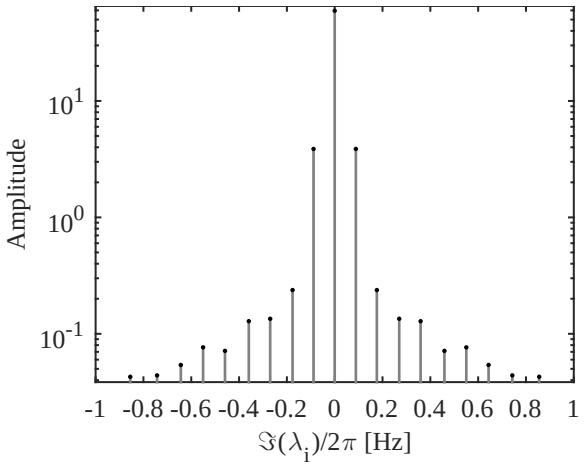

Mode	Dimensionless frequency	$A/A_{\max}$
1	0	1
2	0.149	0.0651
3	0.298	0.0040
4	0.456	0.0023
5	0.607	0.0022

Figure 6.8: DMD amplitude distribution obtained from the phase and spanwise averaged flow fields given by DDES.

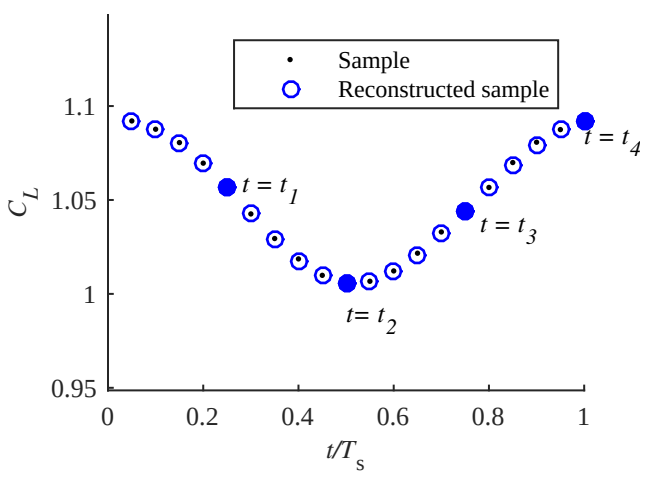

(a) Evolution of the lift coefficient over one period T.

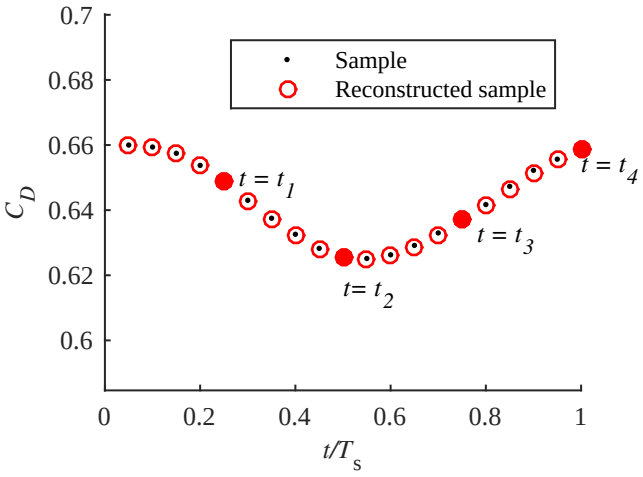

(b) Evolution of the drag coefficient over one period T.

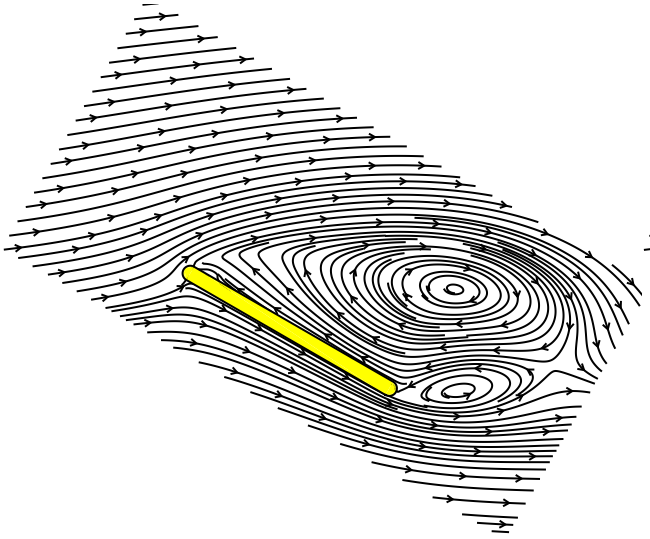

(c) $t = t_1$.

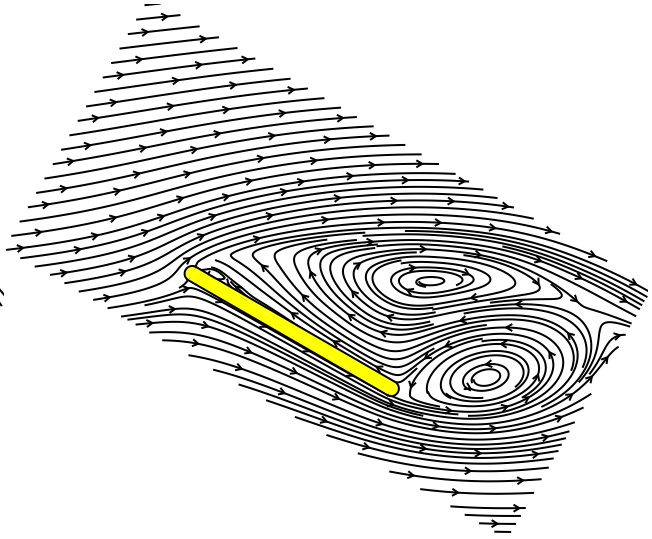

(d) $t = t_2$.

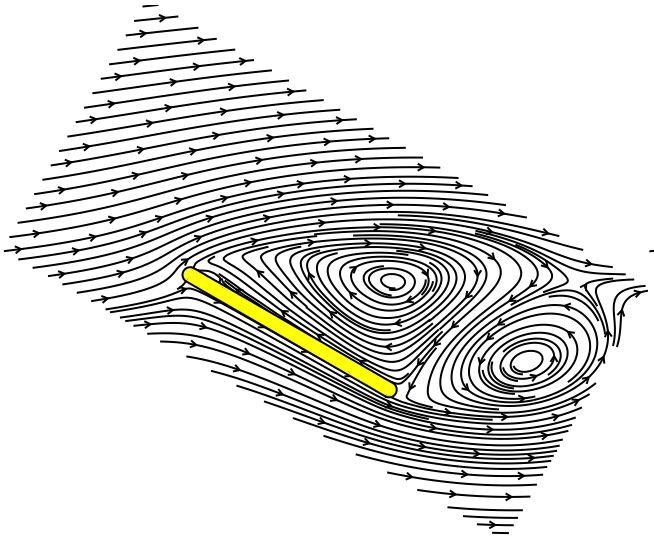

(e) $t = t_3$.

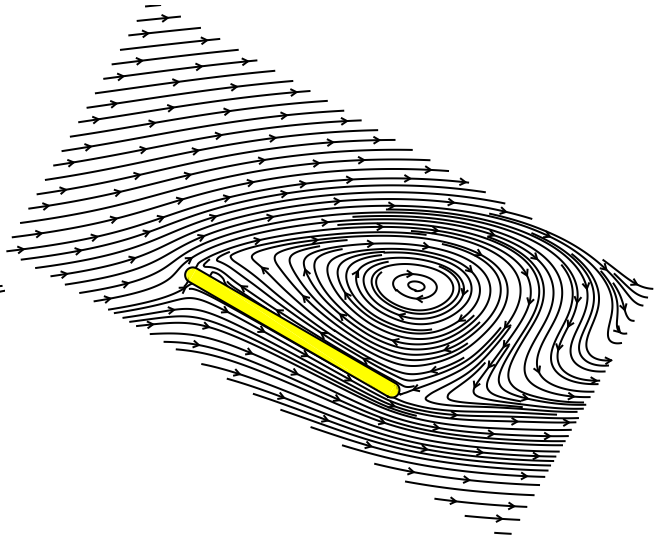

(f) $t = t_4$.

Figure 6.9: Streamlines around the flat plate at $\alpha = 30°$ obtained by reconstruction of the flow fields using the first three dominant dynamic modes (DDES, phase and spanwise average).

The contributions of the vortices to the coefficients C_L and C_D can be directly deduced from the different phases given in Figure 6.9.

Actually, the same flow evolution than the one that has already been described in Figure 5.7 of Chapter 5 is essentially found after reconstruction of the DDES data sequence. The main differences concern the size of the flow structures and the center of the core of the vortices that are involved in the dynamics of the wake.

Once again, it can be seen that the formation and shedding of the trailing-edge vortex (Mode 2) influence the recirculation regions (Mode 1). The drag coefficient is slightly delayed compared to the lift coefficient as can be noticed from Figures 6.9a and 6.9b.

In brief, DMD gives the main flow structures and the value of the aerodynamic force coefficients associated with these structures. The evolution of these coefficients can be related to the evolution of the selected flow structures through this analysis. The dynamic mode decomposition technique is complementary to CFD simulations, particularly to the DDES (or LES) approach as only the most relevant dynamic modes can be retrieved to describe the evolution of the flow over time.

6.2.4 Modal assurance criterion

The Model Assurance Criterion (MAC) is a frequently used technique to compare mode shapes [1]. Considering two families of modes $\mathbf{x}^{\{1\}}$ and $\mathbf{x}^{\{2\}}$, the modal assurance criterion between the *i*th mode of the first family and the *j*th mode of the second family is calculated by

$$\mathrm{MAC}\left(\mathbf{x}_{(i)}^{\{1\}},\mathbf{x}_{(j)}^{\{2\}}\right) = \left(\frac{\mathbf{x}_{(i)}^{\{1\}^T}\mathbf{x}_{(j)}^{\{2\}}}{\left\|\mathbf{x}_{(i)}^{\{1\}}\right\|\left\|\mathbf{x}_{(j)}^{\{2\}}\right\|}\right)^2 \tag{6.13}$$

A quantitative comparison is given by the value of the criterion which is included in $[0,1]$: if MAC is equal to 1, then the correlation is perfect.

The MAC matrices represented in Figure 6.10 are used for the comparison of the modes identified from the numerical results presented in this chapter.

From Figures 6.10a and 6.10b, it may be inferred that an acceptable agreement is noticed between the first two spatial modes extracted from the URANS and DDES flow fields. However, the similarity is weak between the third modes. The spatial modes at higher frequencies are not correlated.

From Figure 6.10c, it can be concluded that the two families of modes (from phase and spanwise averaged DDES flow fields and from phase-averaged DDES flow fields in one cross section) are quite close for the first three dominant modes, justifying the use

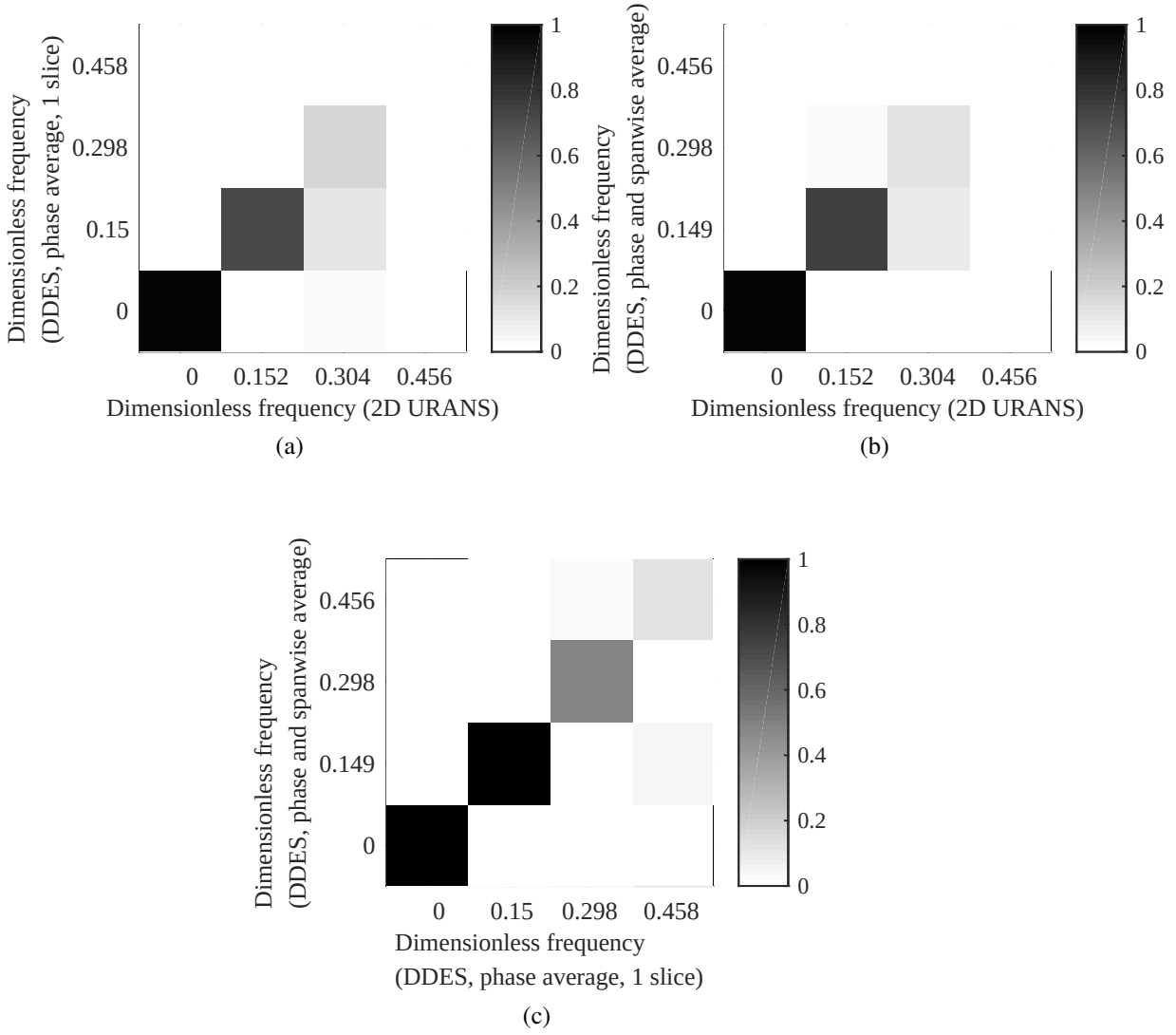

Figure 6.10: Comparison of the three families of modes extracted from different flow fields: (a) DDES (phase average of the flow fields given in a slice) vs. 2D URANS. (b) DDES (phase and spanwise average) vs. 2D URANS. (c) DDES (phase and spanwise average) vs. DDES (phase average of the flow fields given in a slice).

of 2D PIV to study the spatial modes in two dimensions. The concordance is less good between the fourth modes.

The modes of a family can also be compared with themselves to verify that the number of samples is high enough or the spatial resolution is adequate. The AutoMAC matrix, which is a particular case of the MAC matrix, is shown in Figure 6.11 for the modes identified from the DDES phase-averaged flow fields and it indicates that the off-diagonal values are small. Therefore, the spatial discretization and the temporal one used in this chapter have been appropriately chosen because aliasing is avoided [1].

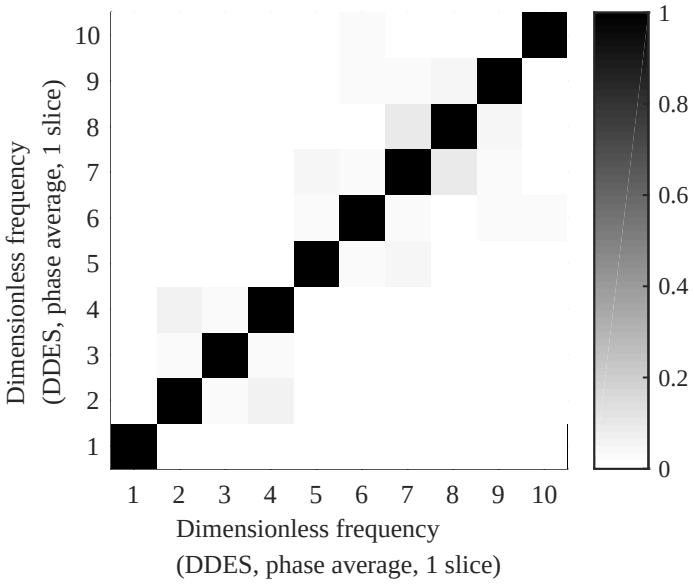

Figure 6.11: AutoMAC for the set of modes extracted from the DDES flow fields (phase average of the flow fields given in a slice).

Chapter 7

Conclusions

7.1 Summary

The first problem considered in this thesis is the flow around a NACA 0012 airfoil at angles of attack below the stall angle. In these cases, the thin boundary layers remain attached over a large surface of the airfoil and the numerical predictions obtained by a two-dimensional steady-state RANS simulation using the Spalart-Allmaras model are in satisfactory agreement with the experimental data found in the literature. The S-A model has rather good performance for attached or mildly separated flows and the RANS computation is efficient.

Then, two configurations have been considered: the flows around a NACA 0012 airfoil at a wide range of angles of attack and a static flat plate at an angle of attack equal to 30°. These problems are challenging because the flows are massively separated.

For the NACA 0012 case, the objective is to test the delayed detached-eddy simulation based on the Spalart-Allmaras model in OpenFOAM. Several sets of simulations are performed:

- First, for a given grid (size and resolution), several angles of attack are tested: $\alpha =$ 8°, 20°, 45° and 60°. The purpose of this set of cases is to validate the DDES solutions obtained using OpenFOAM.

  On the one hand, the present results are compatible with the numerical data given by Spalart *et al.* [19] indicating that there is no major inconsistency in our settings.

  On the other hand, beyond the stall, the DDES predictions are remarkably close to the experimental measurements of the aerodynamic force coefficients. Additionally, for these cases, two-dimensional unsteady RANS simulations using the S-A turbulence model reveal that the URANS predictions are overestimated especially

when large regions of massive separation are present in the flow at high angle of attack.

The prediction of turbulent flows presenting large scale unsteadiness is challenging. An unsteady RANS simulation predicts a periodic behavior while the DDES approach is able to capture the chaotic behavior of massively separated flows, which is reflected by the evolution of the dimensionless force coefficients.

- Second, a grid refinement study is performed. Finer turbulent eddies are captured by DDES if the mesh is refined and there is a trade-off between simulation fidelity and computational cost.

- Lastly, the analysis of the effect of the span length shows that this parameter has a significant influence on the aerodynamic forces. Ideally, the span length should therefore be chosen as close as possible to the geometry considered in the experiment or in the real flow problem.

  The general tendency is that the amplitudes of the fluctuations of the aerodynamic force coefficients predicted by DDES are reduced if the span is increased

  The time-averaged lift and drag coefficients are also slightly reduced due to an increase in three-dimensionality (increased exchange of momentum in the spanwise direction).

For the flat plate case, from a quantitative point of view, the same conclusions than the previous geometry are basically found. Once again, the unsteady RANS simulations using the S-A model, even three-dimensional, are not able to achieve the accuracy of DDES. The DDES predictions are consistent with the available experimental data: the relative error is about 0.43% for $\overline{C_L}$ and about 3.15% for $\overline{C_D}$ with the numerical results obtained with the mesh where the span length is $8c$. These results are quite promising.

Furthermore, the generated flow fields are processed using the Dynamic Mode Decomposition (DMD) method in order to extract dynamic information about the flow. The dynamic behavior of a complex flow problem can be represented by the most dominant dynamic modes. The DMD analysis allows us to better understand the vortex shedding:

- The mean flow mode reveals a large recirculation zone above the surface of the inclined flat plate.

- The dynamic mode associated with the Strouhal number corresponds to a (quasi)-periodic formation and shedding of a vortex close to the trailing edge, which disturbs the flow around the body. This mode controls mainly the unsteady behavior of the separated flow around the static flat plate.

  The vortex shedding is therefore not symmetrical.

The dynamic mode decomposition of the flow fields also facilitates the comparisons between the different approaches used to analyze the flow, i.e., CFD results and experimental measurements. The most dominant flow structures extracted from the PIV data show the same flow features than those obtained numerically, from a qualitative point of view.

7.2 Future perspectives

All the simulations of the present work use the Spalart-Allmaras model. An analysis of the influence of the turbulence model was beyond the scope of this thesis. Simulations using different turbulence models could be carried out to illustrate the strengths and deficiencies of the models. For instance, the NACA 0012 airfoil has already been simulated at high angles of attack and at a Reynolds number $\mathrm{Re} = 10^5$ using the Menter Shear Stress Transport (SST) turbulence model [26]. As shown in the paper, the URANS simulations using this two-equation model lead to poor agreements with the experimental measurements. The differences are even more important than the Spalart-Allmaras model. This example suggests that the S-A model is a good choice for this particular aerodynamic configuration but a further investigation is required.

This thesis focuses on aerodynamic flows. It may be interesting to evaluate the performance of the present simulation approach for other types of flow such as channel flows (e.g., the turbulent flow over a backward-facing step in a channel).

DES may be suitable for engineering applications where the use of LES is too expensive as DES is a less costly approach compared to LES.

Also, the present thesis does not give a complete answer to the low frequency content of the separated flow around the inclined flat plate. With the analyses presented in Chapters 5 and 6, a well-defined dominant low frequency is not present and the identification of the flow structures associated with the low frequency content is challenging. Moreover, the low frequency content may be due to three-dimensional effects (e.g., in the spanwise direction).

In Chapter 6, the vortex shedding has been studied in two dimensions. This approach has the disadvantage that the spanwise flow components are not considered. The flows predicted by the DDES method contain three-dimensional eddies. Another research direction is to investigate the mixing in the spanwise direction, which may influence the vortex shedding and the mean flow.

For the dynamic mode decomposition method, it could be interesting to compare the results obtained by using a sequence of scalar quantities such as ω_z, the spanwise component of the vorticity, or Q, the second invariant of the velocity gradient tensor.

Finally, a future research direction may be to use a numerical model where the mesh

can deform in order to impose small vibrations on the flat plate to be as close as possible to the forced case of the experiments presented in Chapter 5. Actually, the reasons for the discrepancies between the numerical and experimental results may be due to the fact that the flat plate does not vibrate in the numerical simulations.

In this final year project, we have explained the methodology to perform DDES in OpenFOAM. We hope that this thesis can serve as an example for future investigations in the field of dynamics of fluid flows as there are many other interesting aspects that can be studied.

Appendix A

Computation time

All the simulations of this thesis have been run in the NIC4 cluster. The University of Liège hosts the NIC4 cluster which has the following features as documented in `http://www.ceci-hpc.be/`:

- 128 compute nodes with two 8-cores Intel E2650 processors at 2.0 GHz.
- 4 GB of RAM per core.
- The nodes are interconnected with a QDR Infiniband network and they have exclusive access to a fast 144 TB FHGFS parallel filesystem.

Table A.1 contains the computation time associated to each DDES case presented in Chapter 4. It is important to mention that the indicated periods are not very representative as they do not take account of the time related to the following steps:

- The construction of the case (the construction of the mesh in particular). The meshes are created using the open source software Gmsh [7] and they are imported to OpenFOAM using the command `gmshToFoam`.
- To initiate a DDES calculation, the solution from the two-dimensional mesh of a RANS simulation is interpolated to the three-dimensional mesh used for DDES. In OpenFOAM, the `mapFields` command is used for this mapping process.
- The domain decomposition to run the application in parallel on distributed processors, this step is done using the command `decomposePar`.
- The reconstruction of the mesh and data after the simulation is completed. The corresponding command in OpenFOAM is `reconstructPar`.
- The post-processing step: for example, the computation of the magnitude of the velocity (`foamCalc mag U`), the vorticity field (`vorticity`), the second invariant of the velocity gradient tensor (`Q`), et cetera.

- The queued time, which corresponds to the period between the submission of the job and the beginning of its execution at the start of a simulation, or to continue a simulation that has stopped because of the time limit. A job can wait several days in the queue before starting to run depending on the jobs located in the queue.
- The simulation results have to be downloaded from the directory in the cluster to the local directory. It is more efficient to write the flow fields in binary (`writeFormat binary` in the `controlDict` file).

Mesh	Spanwise period	Time step [s]	Computation time (format: `day:hour:minute`)
Mesh I	c	0.004	`00:16:57`
Mesh II	c	0.002	`02:06:10`
Mesh III	c	0.002	`03:21:46`
Mesh IV	c	0.001	`20:13:22`
Mesh I	$2c$	0.004	`01:09:40`
Mesh I	$4c$	0.004	`03:09:51`

Table A.1: Computation time of the DDES cases presented in Chapter 4. The simulations run in parallel on 60 cores of the NIC4 cluster. The simulations end at $t = 500$ s with the data given in Table 4.1.

For Mesh I and for given solver tolerances, the computation in parallel on several nodes of the NIC4 cluster appears to be faster with the choice of solvers and preconditioners given on page 86 compared to other available linear solvers such as the Generalized Geometric-Algebraic Multi-Grid (`GAMG`) solver. Nevertheless, complete simulations with other settings are required in order to be able to choose the optimal parameters, especially for the case using Mesh IV where the computation time is high.

For Mesh IV, in addition to the high number of cells, the time step is four times smaller than the one for Mesh I. Indeed, the finer the mesh is, the smaller the time step has to be for stability. A further investigation is necessary to choose the optimal number of processors as a function of the number of cells knowing that the queued time may increase even more if the number of processors increases.

A.1 `fvSchemes` file for an OpenFOAM DDES case

```
/*--------------------------------*- C++ -*----------------------------------*\
| =========                 |                                                 |
| \\      /  F ield         | OpenFOAM: The Open Source CFD Toolbox           |
|  \\    /   O peration     | Version:  2.3.0                                 |
|   \\  /    A nd           | Web:      www.OpenFOAM.org                      |
|    \\/     M anipulation  |                                                 |
\*---------------------------------------------------------------------------*/
FoamFile
{
    version     2.0;
    format      ascii;
    class       dictionary;
    location    "system";
    object      fvSchemes;
}
// * * * * * * * * * * * * * * * * * * * * * * * * * * * * * * * * * * * * //
// http://www.openfoam.org/docs/user/fvSchemes.php
ddtSchemes
{
    default     backward;
}

gradSchemes
{
    default     Gauss linear;
}

divSchemes
{
    default                         none;
    // http://www.openfoam.org/version2.1.0/numerics.php
    // the surfaceScalarField velocity flux phi = rho U
    div(phi,U)                      Gauss LUST grad(U);
    div(phi,k)                      Gauss limitedLinear 1; // not used for S-A
    div(phi,B)                      Gauss limitedLinear 1;
    // see Section 4.4.1 in the website given in the header
    div(phi,nuTilda)                Gauss limitedLinear 1;
    div(B)                          Gauss linear;
    div((nuEff*dev(T(grad(U)))))    Gauss linear;
}

laplacianSchemes
{
    default     Gauss linear corrected;
}

interpolationSchemes
{
    default     linear;
}

snGradSchemes
```

```
{
    default      corrected;
}

fluxRequired
{
    default      no;
    p            ;
}

// ************************************************************************* //
```

A.2 `fvSolution` file for an OpenFOAM DDES case

```
/*--------------------------------*- C++ -*----------------------------------*\
| =========                 |                                                 |
| \\      /  F ield         | OpenFOAM: The Open Source CFD Toolbox           |
|  \\    /   O peration     | Version:  2.3.0                                 |
|   \\  /    A nd           | Web:      www.OpenFOAM.org                      |
|    \\/     M anipulation  |                                                 |
\*---------------------------------------------------------------------------*/
FoamFile
{
    version     2.0;
    format      ascii;
    class       dictionary;
    location    "system";
    object      fvSolution;
}
// * * * * * * * * * * * * * * * * * * * * * * * * * * * * * * * * * * * * * //
// http://www.openfoam.org/docs/user/fvSolution.php
solvers
{
    p
    {
        solver              PCG;
        preconditioner      DIC;
        tolerance           1e-7;
        relTol              0.01;
    };

    pFinal
    {
        solver              PCG;
        preconditioner      DIC;
        tolerance           1e-7;
        relTol              0; /* the solver relative tolerance is set to zero
                                  to be sure to achieve the solver tolerance */
    };

    "(U|k|B|nuTilda)"
    {
        solver              PBiCG;
        preconditioner      DILU;
        tolerance           1e-7;
        relTol              0;
    };
}

PISO
{
    nCorrectors     2; // default value
    nNonOrthogonalCorrectors 1;
}

// ************************************************************************* //
```

Bibliography

[1] R. Allemang and D. Brown. A correlation coefficient for modal vector analysis. In *Proceedings of the 1st International Modal Analysis Conference*, pages 110–116, 1982.

[2] J. Anderson. *Fundamentals of Aerodynamics*. Anderson series. McGraw-Hill Education, 2010.

[3] M. Breuer and N. Jovicic. Separated flow around a flat plate at high incidence: an les investigation. *Journal of Turbulence*, 2(018):1–15, 2001.

[4] P. A. Davidson. *Turbulence: an introduction for scientists and engineers*. Oxford University Press, 2004.

[5] P. A. Durbin and B. P. Reif. *Statistical theory and modeling for turbulent flows*. John Wiley & Sons, 2011.

[6] ESI-OpenCFD. Openfoam, the open source CFD toolbox. `http://www.openfoam.com`, April 15, 2015.

[7] C. Geuzaine and J.-F. Remacle. Gmsh: A 3-d finite element mesh generator with built-in pre-and post-processing facilities. *International Journal for Numerical Methods in Engineering*, 79(11):1309–1331, 2009.

[8] N. Gregory and C. L. O'Reilly. Low-speed aerodynamic characteristics of naca 0012 aerofoil sections, including the effects of upper-surface roughness simulation hoar frost. *NASA RM 3726*, 1970.

[9] A. Guissart, T. Andrianne, G. Dimitriadis, and V. Terrapon. Using proper orthogonal decomposition and dynamic mode decomposition methods for comparing cfd results and experimental measurements. In *Proceedings of the 16th International Forum on Aeroelasticity and Structural Dynamics*, 2013.

[10] C. Hirsch. *Numerical Computation of Internal and External Flows: The Fundamentals of Computational Fluid Dynamics*, volume 1. Butterworth-Heinemann, 2007.

[11] S. Hoerner. *Fluid-dynamic Drag: Practical Information on Aerodynamic Drag and Hydrodynamic Resistance*. Hoerner Fluid Dynamics, 1992.

[12] J. Jeong and F. Hussain. On the identification of a vortex. *Journal of fluid mechanics*, 285:69–94, 1995.

[13] D. A. Joyce. *Flying beyond the stall: the X-31 and the advent of supermaneuverability*. National Aeronautics and Space Administrations, 2014.

[14] C. L. Ladson. Effects of independent variation of mach and reynolds numbers on the low-speed aerodynamic characteristics of the naca 0012 airfoil section. *NASA TM 4074*, 1988.

[15] NASA Langley Research Center. Turbulence modeling resource. `http://turbmodels.larc.nasa.gov`, April 15, 2015.

[16] S. B. Pope. *Turbulent flows*. Cambridge University Press, 2000.

[17] A. Ruhe. Rational krylov sequence methods for eigenvalue computation. *Linear Algebra and its Applications*, 58:391–405, 1984.

[18] P. J. Schmid. Dynamic mode decomposition of numerical and experimental data. *Journal of Fluid Mechanics*, 656:5–28, 2010.

[19] M. Shur, P. Spalart, M. Strelets, and A. Travin. Detached-eddy simulation of an airfoil at high angle of attack. *Engineering turbulence modelling and experiments*, 4:669–678, 1999.

[20] P. Spalart. Young-person's guide to detached-eddy simulation grids. *NASA Langley Technical Report Server CR-2001-211032*, 2001.

[21] P. Spalart and S. Allmaras. A one-equation turbulence model for aerodynamic flows. *Recherche Aerospatiale*, 1:5–21, 1994.

[22] P. Spalart, W. Jou, M. Strelets, and S. Allmaras. Comments on the feasibility of les for wings, and on a hybrid rans/les approach. *Advances in DNS/LES*, 1:4–8, 1997.

[23] P. R. Spalart, S. Deck, M. Shur, K. Squires, M. K. Strelets, and A. Travin. A new version of detached-eddy simulation, resistant to ambiguous grid densities. *Theoretical and computational fluid dynamics*, 20(3):181–195, 2006.

[24] P. R. Spalart and C. L. Rumsey. Effective inflow conditions for turbulence models in aerodynamic calculations. *AIAA journal*, 45(10):2544–2553, 2007.

[25] A. Travin, M. Shur, M. Strelets, and P. Spalart. Detached-eddy simulations past a circular cylinder. *Flow, Turbulence and Combustion*, 63(1-4):293–313, 2000.

[26] A. Travin, M. Shur, M. Strelets, and P. Spalart. Physical and numerical upgrades in the detached-eddy simulation of complex turbulent flows. In *Advances in LES of complex flows*, pages 239–254. Springer, 2002.

[27] P. Welch. The use of fast fourier transform for the estimation of power spectra: a method based on time averaging over short, modified periodograms. *IEEE Transactions on audio and electroacoustics*, pages 70–73, 1967.